Title	Numerical simulation of thermal and solutal Marangoni convection developing in a floating zone with different heating boundaries under zero gravity
Author(s)	Jin, Chihao
Citation	大阪大学, 2022, 博士論文
Version Type	VoR
URL	https://doi.org/10.18910/89640
rights	
Note	

Numerical simulation of thermal and solutal Marangoni convection developing in a floating zone with different heating boundaries under zero gravity

Chihao JIN

SEPTEMBER 2022

Numerical simulation of thermal and solutal Marangoni convection developing in a floating zone with different heating boundaries under zero gravity

A dissertation submitted to
THE GRADUATE SCHOOL OF ENGINEERING SCIENCE
OSAKA UNIVERSITY
in partial fulfillment of the requirements for the degree of
DOCTOR OF PHILOSOPHY IN ENGINEERING

BY

Chihao JIN

SEPTEMBER 2022

Abstract

Marangoni convection develops along an interface between two fluids due to variation of surface tension caused by temperature and/or concentration gradients, which is called thermal and/or solutal Marangoni convection. It develops during crystal growth whenever there exists surface tension gradients. However, Marangoni convection may adversely affect the crystal quality by forming growth striations by temperature fluctuations and solutal gradients. Therefore, it is important to investigate the dual effects of thermal and solutal Marangoni convection. Due to the opaqueness of semiconductor melt and expensive experiment equipment, numerical simulation provides an effective tool to examine Marangoni flow and make mechanism of heat and mass transfer available, with assumption of zero-gravity condition to eliminate effect of natural convection in the simulation. A floating-zone (FZ) system in a cylindrical shape growing SiGe is selected as the numerical domain. By creating temperature and concentration gradients in the same/ opposite directions along the free surface and choosing a full zone or half zone, thermal and solutal Marangoni convection are observed in the same/ opposite directions.

Firstly, numerical simulation of thermal and solutal Marangoni convection in a full floating zone under zero gravity has been performed to investigate the actual process of crystal growth with heating coils outside the melt. In the system, thermal and solutal Marangoni convection develop along the free surface in the same/opposite directions depending on the region selected. The ambient temperature outside the system is taken as a Gaussian profile, and the radiative heat transfer is considered dominant. The features of concentration pattern in the floating zone vary due to different Marangoni numbers. The flow velocity field exhibits two or four main vortices along the free surface by effects of suppression or augmentation of the two Marangoni flows.

Secondly, the separated lower-half zone is selected as the numerical domain with thermal and solutal Marangoni convection developing in the opposite directions. Due to the complexity of the opposite-direction flow, the supercomputer is required to conduct the simulation. Compared to the study of thermal and solutal Marangoni convection in the same

direction in a half floating zone, the flow patterns of opposite directions behave diversely in various regimes with 2D axisymmetric flow, chaotic flow, oscillatory rotating flow, 3D steady flow, and even switching flow under different Marangoni ratios and combinations of (Ma_C, Ma_T). Furthermore, two kinds of flow transitions are predicted with the increase of $|Ma_T|$ depending on value of Ma_C.

Thirdly, numerical simulation of thermal and solutal Marangoni convection in a floating half zone with radiation effects under zero gravity has been performed. The ambient temperature is kept constant and radiation due to heat loss and heat gain is considered as dominant heat transfer from the ambience. Transition mode maps, based on concentration distribution with respect to Marangoni ratio and ambient temperature have been developed to investigate the radiation effects at unequal or equal (Ma_C, Ma_T) values. Furthermore, two sorts of oscillatory modes are observed in the same-direction Marangoni flows under either heat loss or heat gain. While two kinds of stabilizing effects are predicted under heat loss in the opposite-direction Marangoni flows.

This thesis demonstrates the characteristics of thermal and solutal Marangoni convection developing in a full or half floating zone during crystal growth of SiGe with different heating boundaries under zero gravity. Unique findings, such as characteristic flow patterns, as well as transition mode predictions and suppressions of flow instability, would contribute to the control of unsteady Marangoni convection and obtaining the crystal with higher quality.

Contents

Chapter I General Introduction

1.1 Semiconductor material of SiGe

Silicon-germanium (SiGe) single crystal is an important semiconductor with many unique properties [1, 2], such as "fast data processing", "lower energy consumption", and "potential" for use in the bandgap and lattice parameter engineering. It has broad applications in the field of material technology. SiGe can be grown by different techniques in industry [3], like Floating-Zone (FZ) [4, 5], Bridgeman [6, 7], and Czochralski [8, 9]. However, when it comes to the crystal growth of SiGe, the instability including gravitational effect, surface tension gradients, volume change, melt wetting, and impurity inhalation can alter the quality of crystal growth, among which two major problems are segregation and convection.

The segregation coefficients of Si and Ge vary a lot, with Si larger than 0.3 and Ge smaller than 5. Besides, since the density of germanium ($\rho_{Ge} = 5.35\,g/cm^3$) is much larger than that of silicon ($\rho_{Si} = 2.33\,g/cm^3$), such a large density difference may cause gravitational segregation (due to strong natural convection) in the melt which could be a dominant factor in affecting the growing crystal. According to the unique physical properties, advanced liquid-phase and solid-phase crystallization process of group IV semiconductors have been reviewed in [10].

1.2 Flow phenomenon during crystal growth

The flow phenomenon during crystal growth [11] is quite complicated due to the various components of the flow, including natural convection [12] induced by the temperature or concentration gradients, Marangoni convection along the free surface caused by variation of surface tension and forced convection by some external conditions, such as exerting magnetic fields or rotation of growing crystal. These flows mainly exist in different regions of the melt part but can interact with each other tightly.

Heat convection is the most universal form of natural convection. The temperature gradients of fluid in the gravity field can cause the buoyancy flow. When the temperature gradient is normal to the gravity, any temperature gradient in the horizontal direction may

induce heat convection. If directions are the same, the flow becomes more complicated because of the existence of viscous force. Apart from natural convection by temperature gradients, the concentration differences of solutes can also induce density differences, which may further generate buoyancy flow [13]. Normally, these two kinds of natural convections exist simultaneously during crystal growth of a binary compound. The combined effects are much more intricate than the individual effect.

Marangoni convection is mainly induced by variation of surface tension along the free surface. In a crystal growth system on the Earth, the buoyancy flow is dominant due to gravitational effect. However, under microgravity or in a small growth system, Marangoni convection becomes notable and is obvious to observe. The phenomenon of Marangoni convection will be discussed in the next part.

In the Czochralski method, the rotation of crucible and growing crystal is required for a higher quality. The rotation can produce forced convection, which can be beneficial to the interface with lower oxygen transport [14]. When the two planes rotate, the fluid between the planes rotates at an average speed as a rigid body. The fluid also tends to flow towards the faster plane. Also, the forced convection can be applied to control the flow instability or suppress the unsteady flow, such as control of Marangoni convection by external magnetic fields [15, 16].

Sometimes, different convections exist simultaneously during crystal growth. If exerting external conditions, we may find that the flows can interact with each other. Under normal-gravity conditions and in the presence of free surface, if the size is not limited, both buoyancy convection and Marangoni convection play an important role in determining the flow structure and can interact in a very complex way even if the flow is steady. Some studies focus on the phenomenon of interacting flows. Hirata *et al.* [17] investigated the effect of gravity (natural convection) on Marangoni convection in a liquid bridge and observed temperature oscillations under not only 1 *g* but also microgravity conditions. Bég *et al.* [18] investigated hydromagnetic Marangoni flow in a Darcian porous semiconductor melt enclosure with buoyancy and heat generation effects by combining and comparing various dimensionless numbers, which finds applications in crystal growth of semiconductor and

hydromagnetic materials. From this point of view, a deep understanding of mixed convections is beneficial to material processing and even flow control.

1.3 Marangoni convection

There are many examples of Marangoni convection in our daily life. One is "*Tears of wine*", as shown in **Fig. 1-1** [19]. Since water has a higher surface tension than that of wine (ethanol), when alcohol evaporates from the region of a thinner glass wall, the surface tension gradient generates. The wine climbs up spontaneously forming a firm. Due to the effect of gravity, the wine tears down. So, we call this phenomenon "*Tears of wine*", which can be demonstrated by the mechanism of Marangoni convection.
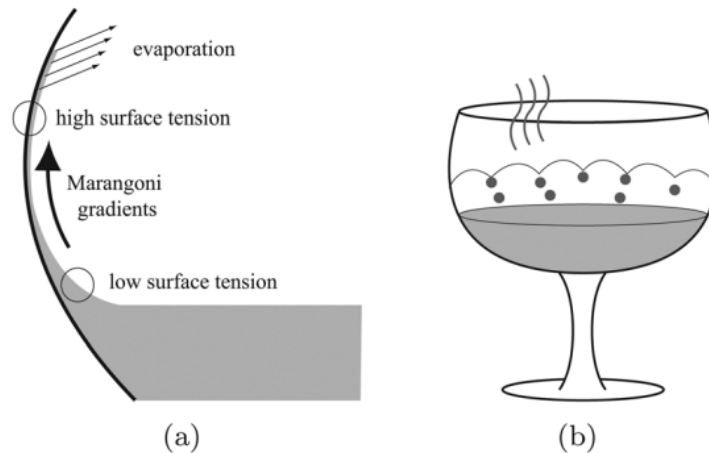
Fig. 1-1 Marangoni phenomenon of "*Tears of wine* ". [19]

Marangoni convection is a fluid flow developing along an interface between two fluids due to the variation of surface tension caused by temperature or concentration gradients. This flow is called respectively thermal or solutal Marangoni convection. When both gradients present, the flow is called thermo-solutal Marangoni convection. Marangoni convection develops in crystal growth whenever there exists a free surface with temperature and/or concentration gradients along it.

Fig. 1-2 briefly shows Marangoni convection caused by temperature differences between two planes [20]. From figure below, we can see Marangoni convection develops when there

exists a temperature difference (higher temperature on top plane and lower temperature on bottom plane). A smaller temperature difference (ΔT) makes Marangoni flow steady. By increasing ΔT, the flow becomes oscillatory with periodic variation. A greater ΔT beyond the critical value induces the turbulent flow with chaotic and random variation. It is known that changing temperature difference along the free surface can alter the flow state, whether to be steady or unsteady. Several studies have indicated the onset of the time-dependent [21, 22] convection and oscillatory flows [23, 24].
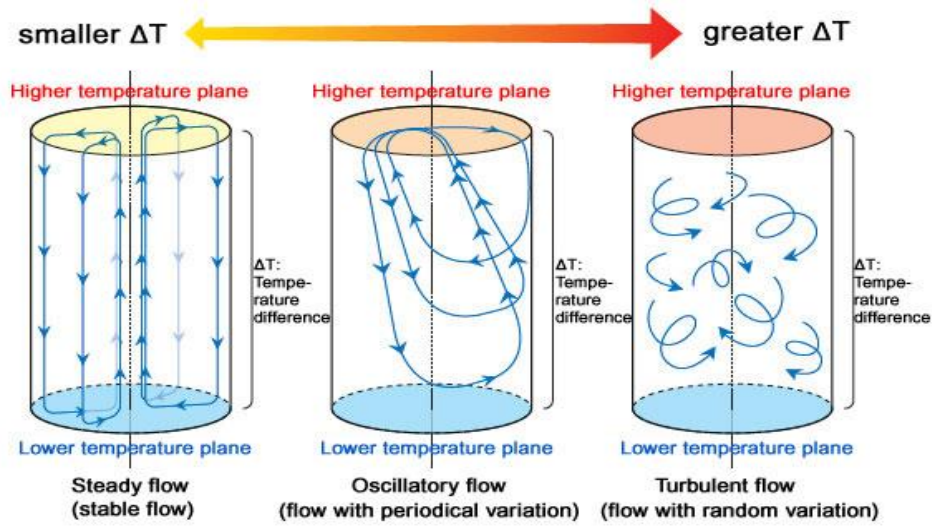
Fig. 1-2 Marangoni convection caused by temperature differences between two planes. [20]

To sense the strengths of thermal and solutal Marangoni convection, the non-dimensional thermal and solutal Marangoni numbers (Ma_T and Ma_C) are introduced, which are the ratios of surface tension gradient to viscous force. Details of Marangoni numbers will be discussed in **Chapter II**.

Changing (increasing or decreasing) the temperature differences along the free surface can lead to the flow transition from one state to another state. In fact, transitions of Marangoni convection also depend on *Pr* numbers [25]. With a higher *Pr*-number fluid, the 2D axisymmetric flow transits to oscillatory flow directly after exceeding the critical number Ma_C, as shown in **Fig. 1-3**. With a lower *Pr*-number fluid, there are two stages of transitions, with the first stage from 2D axisymmetric flow to 3D steady flow beyond Ma_{C1} and second

stage further transiting to oscillatory flow over Ma_{C2}. Both the transition paths undergo turbulent flow once Marangoni number is extremely high. Correspondingly, some studies focus on Marangoni convection under different *Pr* numbers [26, 27, 28]. Christopher *et al.* [29] investigated effects of Prandtl number on Marangoni convection over a flat surface and analyzed how heat transfer variation changes with different *Pr* numbers. Arafune *et al.* [30] investigated thermal Marangoni convection in fluids with various Prandtl numbers ($o[10^{-3}]{\sim}o[10^3]$) inside a rectangular open boat experimentally and numerically. By calculating dimensionless numbers, it is available to determine which convection is dominant. Since most of *Pr* numbers of semiconductor materials are of the order of $o[10^{-3}]{\sim}o[10^{-2}]$, we focus on the situation with a small value of *Pr* in our research.
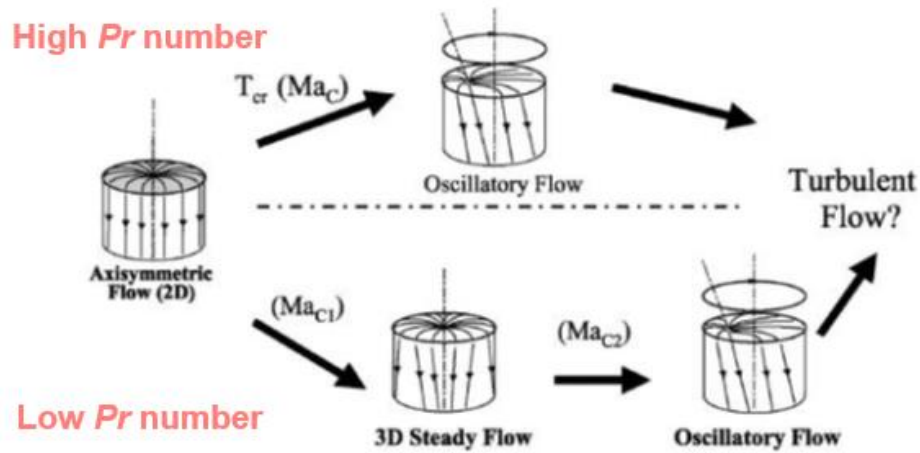
Fig. 1-3 Transitions of Marangoni convection with respect to *Pr* number ($= \nu/\alpha$). Ma_C means critical Marangoni number. [25]

1.4 Effects of Marangoni convection on crystal growth

Marangoni convection may become turbulent and chaotic once Marangoni number is extremely large, which can adversely affect the growing crystal. There are three aspects to measure the quality of growing crystal: purity, uniformity, and integrity. The purity requires the less useless impurity. The uniformity means the useful dopants distribute uniformly in the growing crystal. The integrity permits the dislocation density [31] within the allowable

range. During crystal growth, the dominant defect is the formation of growth striations [32, 33].

Marangoni convection developing in the FZ melt may become unstable, and lead to growth instabilities such as growth striations (growth rate variations) which affect crystal quality adversely [34]. On the one hand, growth striations can develop by variation of growth rate, which is caused by temperature fluctuations. On the other hand, solutal gradients can induce free surface deformation to a concave interface, which further exacerbates the uniformity defects of growth striations [35]. For example, in the SiGe system, the large separation of liquidus and solidus curves leads to a significant segregation of Ge in front of the growing interface during growth. The growth rate and the overall mixing of the melt are the key factors determining the strength of solutal Marangoni convection. Therefore, it is important to simultaneously examine the mechanisms of both thermal and solutal Marangoni convections during crystal growth to minimize the adverse effects of such flow instabilities.

From this point of view, we focus on the investigation of Marangoni effects and contribute to obtaining crystals with better quality. Meanwhile, to separate the natural convection [36] from Marangoni convection in the melt, and to shed light on the effect of Marangoni convection alone, it is necessary to consider the system under zero-gravity or microgravity environments.

1.5 Microgravity experiments and numerical simulations

In the microgravity environment, the strength of natural convection is very weak due to the reduced gravity and strength of Marangoni convection in a floating zone becomes comparable with that of natural convection. A series of experiments of Marangoni convection have been performed on the International Space Station (ISS) [37, 38, 39]. For example, microgravity experiments on thermocapillary convection in a liquid bridge, called *Marangoni Experiment in Space (MEIS)*, are reported in [40]. Kang *et al.* [41] investigated the instability of Marangoni convection experimentally under microgravity and found three types of surface configurations depending on the volume ratio, with further investigation on different waves. In fact, the real microgravity environment may also consist of a spectrum

of accelerations at different frequencies ranging from zero to hundreds of Hertz. These deviations are known to be the origin of convective contribution to mass transfer.

Although the microgravity environment may serve as an indispensable research platform to study the instability mechanism of Marangoni convection [42], the availability of such microgravity experiments is very rare, and the equipment is very costly. They also require very complex systems to be developed. Besides, it is difficult to directly observe the flow phenomenon in the experiment due to the opaqueness of semiconductor melt. Numerical simulation makes it available by using the visualization software to analyze the flow pattern prominently. Thus, method of numerical simulation may provide an inexpensive but effective tool in examining the effects of Marangoni flows in a FZ system.

1.6 Control of Marangoni convection

The flow regime in the liquid is the dominating factor for heat and mass transfer during crystal growth. Thus, the efforts of controlling the flow intensity and bifurcations has become an important issue to obtain crystals with higher uniformity. There are several methods of controlling the flow instability by applying external conditions.

Since molten semiconductors are excellent electrical, one primary method of controlling Marangoni flow is to exert magnetic fields [43, 44, 45]. The motion of electrically conducting melt under magnetic fields induces electric currents. Lorentz forces, resulting from the interaction between electric currents and magnetic fields, affect the flow. Typically, an increase in Hartmann number [46] would decelerate Marangoni flow. Apart from the traditional horizontal and vertical magnetic fields, more complex ones are developed to better perform the investigation of flow mechanism and control of unsteady flow, such as cusp magnetic fields, rotating magnetic fields, and inclined magnetic fields [47, 48].

Melt flow control can be realized by other methods. For example, rotating or accelerating the crystal/crucible in the Czochralski crystal growth [49] or exerting appropriate vibrations [50, 51] is available to control the unsteady flow. Crystal/crucible rotation can alter Marangoni convection by the existing centrifugal force. Even in a FZ system, the adoption of co-rotation or counter-rotation of top and bottom planes can affect the flow instability under some circumstances. In a Czochralski growth, Noghabi *et al.* [52] investigated effect

7

of crystal and crucible rotations on melt convection and indicated that the melt flow regime would be strongly sensitive to the rotation speeds and low deflection can be achieved at certain combinations of rotation rates. Alternatively, Marangoni convection and vibrations can produce the flows of opposite directions in some cases, which further reduces the flow strength. Meanwhile, vibrations are not restricted to electrically conductive melts, which means it can be widely applied in the flow control, as well as in a FZ system. Lyubimova *et al.* [53] investigated control of thermocapillary and solutocapillary flows in a FZ system by applying axial vibrations and found that vibrations can behave a stabilizing effect in the form of increasing critical Marangoni numbers for all unsteady modes, while a destabilization effect at a high intensity of vibration.

Although individual method can be used to realize the flow control, in most cases, there applies a combination of magnetic fields, crucible rotation or vibrations to comprehensively influence the convection, behave optimal in suppression of flow instability, and even provide uniform crystal-growth rate as shown in [54, 55].

1.7 Relevant study on Marangoni convection

Various physical systems or simplified models are selected to perform research on Marangoni convection, such as a weld pool [56], a thin film [57], a rectangular cavity [58], and an annular pool [59]. And there are many studies focusing on the mechanism of Marangoni convection and determining appropriate external conditions to control the unsteady flows [60, 61, 62, 63]. The following studies are cited to briefly describe some findings in research.

Imaishi *et al.* [64] predicted flow bifurcations as the temperature difference increases in a liquid bridge at smaller Prandtl numbers in their study. Li *et al.* [65] investigated three types of oscillatory Marangoni flows in half-zone liquid bridges of low *Pr*-fluids by proper orthogonal decomposition (POD) using method of snapshots and determined oscillatory disturbances with characteristic eigenfunctions. Li *et al.* [66] also studied change in the oscillation mode by time evolutions of thermocapillary flows in a short half-zone of molten tin with low *Pr* number. Wide surveys of this aspect can be found in [67, 68]. Since the combined thermal and solutal Marangoni convection can affect the melt flow and quality of

8

growing crystal, investigation of dual effects of two flows becomes prevalent. Several studies concentrate on thermal and solutal Marangoni flows that co-exist in a floating zone or a rectangular cavity [69, 70]. Mendis *et al.* [71, 72] performed a global linear stability analysis to further determine the onset of thermal and solutal Marangoni convection and critical transition in a half-zone liquid bridge. These studies are conducted with respect to the relative contributions of thermal and solutal Marangoni convection. In this thesis, we also take the dual Marangoni effects with different strengths into consideration.

In our previous study, Minakuchi *et al.* [73, 74] investigated the relative contributions of thermal and solutal Marangoni convection of the same direction in a half-zone system under zero gravity by numerical simulation, and showed the co-existence of two flows significantly affects the flow pattern and azimuthal wave number (*m*). Augmented effects with *m*-fold symmetry and oscillatory rotating tendency are dominantly observed at large Marangoni numbers. Minakuchi *et al.* [75] also performed numerical investigation on hysteresis phenomenon of flow patterns induced by thermal and solutal Marangoni convection in a half-zone system under zero gravity. It is found that the hysteresis behavior of flow field with about 24% difference between critical values in the hysteresis diagram. These results and findings are based on the assumption of the same flow direction of thermal and solutal Marangoni convection

Meanwhile, we are more interested in the mixed thermal and solutal Marangoni convection of opposite directions in a half floating zone and the overall flow pattern in a full floating zone to determine whether the flow behaves similarly or differently. Furthermore, investigation by changing the heating boundary conditions from "adiabatic free surface" to "radiative heat transfer" is also considered an important factor to determine the radiation effects on Marangoni convection, especially under conditions of heat loss or heat gain, which constitutes our main objective of this thesis. Finally, the obtained findings and discussions are necessary to gain further insight into the mechanism of thermal and solutal Marangoni convection during crystal growth under different conditions. Besides, with the help of supercomputers supported by *Kyushu University, Japan*, the subsequent calculations have been performed.

1.8 Outlines of thesis

This thesis aims to give insight into the combined thermal and solutal Marangoni convection developing in a floating zone with different heating boundaries under zero gravity by numerical simulation.

In **Chapter II**, the numerical methods including model simplifications and assumptions, governing equations, boundary conditions, and numerical schemes are presented. Also, non-dimensional thermal Marangoni number (Ma_T), solutal Marangoni number (Ma_C), and Marangoni ratio (R_σ) are introduced.

In **Chapter III** [76], numerical simulation of thermal and solutal Marangoni convection in a full floating zone under zero gravity has been performed. With the assumption of ambient temperature in a Gaussian profile in the vertical direction, the features of temperature distribution, concentration pattern, and flow velocity field at different combinations of (Ma_C, Ma_T) in a full zone are shown.

In **Chapter IV** [77], the lower-half zone is selected as the numerical domain with thermal and solutal Marangoni convection developing in the opposite directions. The characteristic flow regimes under various combinations of (Ma_C, Ma_T), such as 2D axisymmetric flow, chaotic flow, oscillatory rotating flow, 3D steady flow, and switching flow in a transition state are determined, and the flow transitions are predicted with the increase of $|Ma_T|$ depending on value of Ma_C.

In **Chapter V** [78], numerical simulation of thermal and solutal Marangoni convection in a floating half zone with radiation effects of heat loss and heat gain under zero gravity has been performed. Transition mode maps, based on concentration distribution with respect to Marangoni ratio and ambient temperature, have been developed. Two sorts of oscillatory modes in the same-direction Marangoni flow and two kinds of stabilizing effects in the opposite-direction Marangoni flows are also predicted.

The conclusions of this thesis and future perspectives are summarized in **Chapter VI**.

Chapter II Numerical Methodology

2.1 Floating-zone (FZ) method

Marangoni convection is widely observed in the melt during crystal growth of the binary compound. We choose a floating-zone (FZ) system to grow the crystal of SiGe. Compared to other growing techniques, such as Bridgeman and Czochralski, the FZ method is widely used due to main advantage of being a crucible-contamination-free technique, which means it is free from incorporating impurities, improving the quality of growing crystal.

Fig. 2-1 describes schematically Marangoni convection developing in the SiGe melt of a FZ system. Between the feed crystal and seed crystal is the melt part, where Marangoni convection can be observed. The blue arrows represent thermal Marangoni convection and the yellow arrows stand for solutal Marangoni convection. In an actual process of crystal growth, by moving the heating coils upwards slowly, the melt is formed by the localized heating and single crystal grows vertically from the seed crystal. Our simulation study of Marangoni convection is based on the melt part in a floating-zone system.
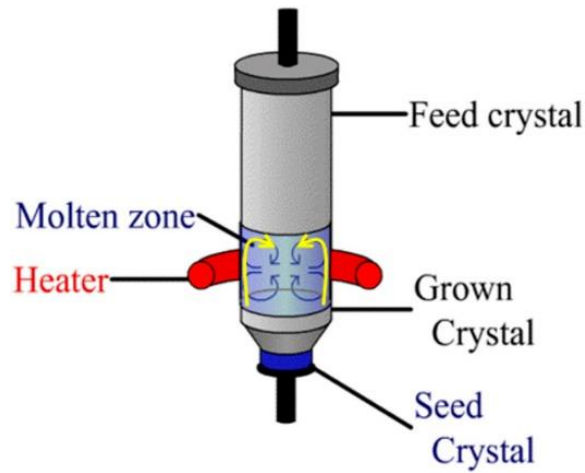

Fig. 2-1 Schematic view of the floating-zone system used for SiGe crystal growth. Between the feed and seed crystal is the melt where thermal and solutal Marangoni convection develop.

However, under Earth conditions, the crystal can easily drop down if the melt gets too large, which limits the potential diameter under Earth's gravity [79]. In space, the maximum

zone height is given by the circumference of crystal. Therefore, the microgravity or zero-gravity environment is feasible for growing crystals with higher zone heights and larger diameters, which enables the production of crystals that exhibit unique properties. This pioneering research is leading to the next-generation commercial crystal products.

2.2 Liquid bridge

Fig. 2-2 shows detailed information of thermal and solutal Marangoni convection in a melt, which develop along the free surface due to variation of surface tension by temperature or concentration gradients. The direction of Marangoni convection is from the region with a lower surface tension to the one with a higher surface tension. Given that the heating coils are set outside the melt in an actual manner, the highest temperature (with smallest surface tension) locates almost middle of the zone, giving rise to thermal Marangoni convection in the vertical direction. Besides, in terms of different materials of Si and a mixture of SiGe that are put near the feed and seed crystal respectively, we assume solutal Marangoni convection is monodirectional from the bottom to the top due to the segregation coefficient of Si and Ge.
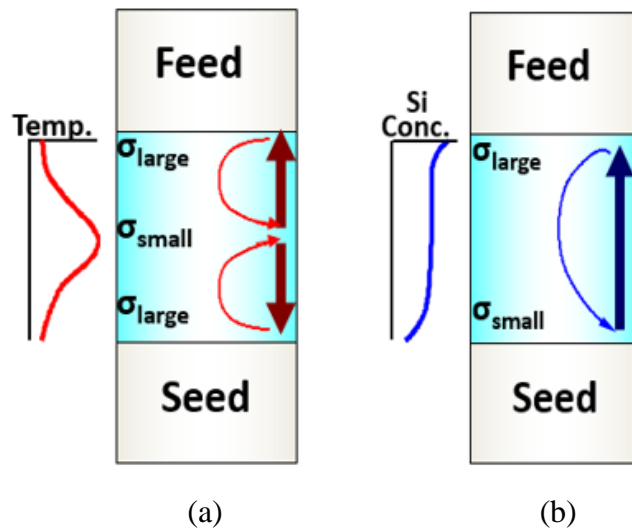

(a)   (b)

Fig. 2-2 Marangoni convection develops in the melt due to variation of surface tension by temperature or concentration gradients, (a) thermal Marangoni convection, (b) solutal Marangoni convection.

Note that if different regions are selected, thermal and solutal Marangoni convection can be either in the same direction or opposite directions. If we select the upper half zone, two convections are in the same direction, while in the opposite direction if the lower half zone is considered. Therefore, in the following discussions, we would like to consider the full zone as well as the separated half zone to focus on the flow mechanism in different regions.

In order to easily understand the flow characteristics, it is necessary to simplify the floating zone system as a cylindrical "liquid bridge" [80, 81] with two coaxial planes, as shown in **Fig. 2-3**. The liquid bridge has some unique properties, such as the applied temperature is known a priori in the analysis and the interface is generally considered adiabatic with isothermal plane areas. The cylindrical coordinate system is located at the center of the bottom plane with the radial (r), azimuthal (θ), and vertical (z) directions. The radius and length of liquid bridge are $a = 0.01$ m and $L = 0.005$ m in a half-zone system ($L = 0.01$ m for a full zone), respectively. It is assumed that (i) the melt, a mixture of silicon and germanium, is incompressible and Newtonian; (ii) the solid/liquid interfaces are flat; (iii) the system is under zero gravity. Since we carry out the numerical simulation under zero gravity, and also due to small Capillary number of the melt, we assume that (iv) the melt between two planes do not deform and remains cylindrical during simulations.
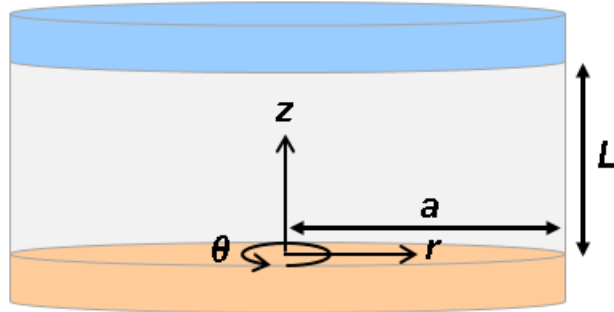

Fig. 2-3 Configuration of a cylindrical liquid bridge.

2.3 Governing equations

The governing equations of the flow in SiGe melt are the well-known continuity, momentum, energy, and mass transfer equations, given by:

$$\nabla \cdot \boldsymbol{v} = 0 \tag{1}$$

$$\frac{\partial \boldsymbol{v}}{\partial t} + \boldsymbol{v} \cdot \nabla \boldsymbol{v} = -\frac{1}{\rho} \nabla p + \nu \Delta \boldsymbol{v} \tag{2}$$

$$\frac{\partial T}{\partial t} + \boldsymbol{v} \cdot \nabla T = \alpha \Delta T \tag{3}$$

$$\frac{\partial C}{\partial t} + \boldsymbol{v} \cdot \nabla C = D \Delta C \tag{4}$$

where $\boldsymbol{v} = (v_r, v_\theta, v_z)$ is the flow velocity, t is time, ρ is density, p is pressure, T is temperature, C is the molar fraction of silicon in the SiGe melt, while ν and α represent the kinematic viscosity and thermal diffusivity of the melt, respectively, and D is the diffusion coefficient of C.

2.4 Boundary conditions

As for the boundary conditions at the height of $z = 0$ and $z = L$, the no-slip condition with $v_r = v_\theta = v_z = 0$ is applied for the flow velocity field both on the top and bottom planes of the melt. The condition of pure silicon is imposed on the top plane ($C_{\text{top}} = 1$), while a concentration value of SiGe ($C_{\text{bottom}} < 1$) is set on the bottom plane. For the case of thermal and solutal Marangoni flows in a half floating zone in the same direction, higher temperature is set on the bottom plane and a lower temperature value is set on the top plane. The above selected temperature values on the planes are reversed to develop flows in opposite directions, by inducing opposite thermal and solutal gradients along the free surface. If a full floating zone is considered, the ambient temperature varying by vertical position in the vertical direction is required to give rise to the thermal Marangoni convection. Details of boundary conditions of top and bottom planes will be described in the following chapters.

The boundary conditions of Marangoni flow in the r, θ, z directions on the free surface ($r = a$) are given as:

$$v_r = 0 \tag{5}$$

$$\mu \left[r \frac{\partial}{\partial r} \left(\frac{v_\theta}{r} \right) \right] = \frac{1}{r} \left(\frac{\partial \sigma}{\partial T} \frac{\partial T}{\partial \theta} + \frac{\partial \sigma}{\partial C} \frac{\partial C}{\partial \theta} \right) \tag{6}$$

$$\mu \frac{\partial v_z}{\partial r} = \frac{\partial \sigma}{\partial T} \frac{\partial T}{\partial z} + \frac{\partial \sigma}{\partial C} \frac{\partial C}{\partial z} \tag{7}$$

where μ is the viscosity of the melt, and $\partial \sigma / \partial T$ (< 0) and $\partial \sigma / \partial C$ (> 0) are the surface tension coefficients of temperature and concentration, respectively.

The surface tension along the free surface is considered as the following linear function with temperature and concentration:

$$\sigma(T, C) = \sigma_0 - \sigma_T(T - T_0) - \sigma_C(C - C_0) \tag{8}$$

where σ_0, T_0, and C_0 are the reference surface tension, reference temperature, and reference concentration, respectively. σ_T and σ_C is the same as $\partial\sigma/\partial T$ and $\partial\sigma/\partial C$ correspondingly.

The temperature boundary condition on the free surface varies by different heating conditions. Basically, with an adiabatic free surface, it follows "zero gradient" in the radial direction as shown below.

$$\frac{\partial T}{\partial r} = 0 \tag{9}$$

With the consideration of radiation effects from the ambience, it follows "radiative heat transfer" by neglecting the connective heat transfer due to its weakness.

$$-k\frac{\partial T}{\partial r} = \varepsilon\sigma_{SB}(T^4 - T_a^4) \tag{10}$$

where k is the thermal conductivity of melt, ε is the emissivity, and σ_{SB} is the Stefan-Boltzmann constant. T_a is the ambient temperature, which can be either constant or as a function of height, $T_a(z)$.

The concentration boundary condition on the free surface is considered as "zero gradient":

$$\frac{\partial C}{\partial r} = 0 \tag{11}$$

Some details of physical properties of binary compound of SiGe is shown in **Table 2-1**, where Pr $(= \nu/\alpha)$ and Sc $(= \nu/D)$ stand for Prandtl number and Schmidt number, respectively. Pr and Sc number are kept constant in the whole study.

Table 2-1 Physical properties of binary compound of SiGe. [82]

Property	Symbol	Value
Kinematic viscosity	ν [m²/s]	1.40×10^{-7}
Thermal diffusivity	α [m²/s]	2.20×10^{-5}
Diffusion coefficient	D [m²/s]	1.00×10^{-8}
Prandtl number	Pr	6.37×10^{-3}
Schmidt number	Sc	14.0

2.5 Marangoni numbers

Non-dimensional thermal and solutal Marangoni numbers are defined as below, with the ratio of surface tension gradient to viscous force, to describe the strength of Marangoni convection.

$$Ma_T = \left|\frac{\partial \sigma}{\partial T}\right| \cdot \frac{\Delta T L}{\mu v} \tag{12}$$

$$Ma_C = \left|\frac{\partial \sigma}{\partial C}\right| \cdot \frac{\Delta C L}{\mu v} \tag{13}$$

In a floating zone system, ΔT and ΔC are the temperature and concentration differences, mostly defined as differences between two planes, which primarily induce thermal and solutal Marangoni convection. These definitions are equivalent to the capillary Reynolds numbers and are presented in a different expression in some studies [83, 84].

The Marangoni ratio (R_σ) is presented to describe the comparative strength of solutal Marangoni convection to thermal Marangoni convection. Normally, when $R_\sigma = 1$, two Marangoni flows are of equivalent strength. R_σ is discussed in detail in the following sections.

$$R_\sigma = \frac{Ma_C}{Ma_T} \tag{14}$$

2.6 Numerical schemes

The governing equations (1-4) are discretized by the Finite Volume Method (FVM) and solved by the PISO algorithm in the OpenFOAM software.

The FVM is a method for representing and evaluating the partial differential equations in the form of algebraic equations. The values are calculated at discrete places on a meshed geometry. The finite volume refers to the small volume surrounding each node point on a mesh. In the FVM, the volume integrals in a partial differential equation that contain a divergence term are converted to the surface integrals, using the divergence theorem. These terms are then evaluated as the fluxes at the surfaces of each finite volume. Because the flux entering a given volume is identical to that leaving the adjacent volume, this method is conservative.

The PISO algorithm (Pressure Implicit with Splitting of Operator) is proposed without iterations and with large time steps and a lesser computing effort. It is an extension of the SIMPLE algorithm used in computational fluid dynamics (CFD) to solve the Navier-Stokes equations. PISO is a pressure-velocity calculation procedure for the Navier-Stokes equations developed originally for non-iterative computation of unsteady compressible flow, but it has been adapted successfully to steady-state problems. The PISO involves one predictor step and two corrector steps and is designed to satisfy mass conservation using predictor-corrector steps.

The computation is carried out by using the open-source software OpenFOAM. The solver applied in the simulation is "*icoTSmaFoam*", improved from the basic "*icoFoam*". Euler scheme, QUICK scheme, and Gauss linear scheme are applied respectively to the terms involving time derivative, divergence, and Laplacian in the governing equations. The computational mesh applied in a half zone simulation is shown in **Fig. 2-4**, with 40, 160, and 60 meshes in the r, θ, z directions, respectively. In a full zone simulation, the mesh number in the z-direction is doubled to 120 to improve the calculation accuracy. The mesh has been refined due to the complicated flow near the free surface and top/bottom plane when we consider the opposite effects of thermal and solutal Marangoni convection.

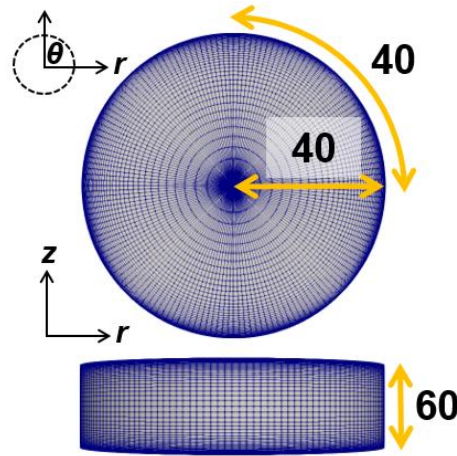**Fig. 2-4** Computational mesh applied in a half zone simulation. The mesh number in the r, θ, z directions are 40, 160, and 60, respectively. The total mesh number is 384,000.

The details of the non-uniform grid refinement, numerical schemes, and validation of the solver using OpenFOAM can be found in the previous research [85, 86]. Details of mesh dependency are shown in the following chapters.

Chapter III Thermal and Solutal Marangoni Convection in a Full Floating Zone

In this chapter, numerical simulation of thermal and solutal Marangoni convection in a full floating zone under zero gravity has been performed to investigate the actual process of crystal growth with heating coils outside the melt. In the system, thermal and solutal Marangoni convection develop along the free surface in the same/opposite directions depending on the region selected. The ambient temperature outside the system is taken as a Gaussian profile, and the radiative heat transfer is considered dominant.

3.1 Full floating zone

In a full floating zone, the heating coils are placed outside the melt part, by moving along with the growing crystal they provide the intended applied temperature profile to the free surface, as shown in **Fig. 2-1** in **Chapter II**. Since the radiative heat transfer is mainly responsible for inducing the flow in the zone, it must be taken into account properly in the model. Although there are several heating-profile models as heating source, either can be heat power or ambient temperature distribution, used in a floating zone in the vertical direction around the equatorial plane [87], the Gaussian temperature profile would be more suitable to accommodate the contribution of heating coils to the floating zone, and most of the studies applied Gaussian temperature profile [88, 89, 90]. In this profile, the equatorial plane receives the maximum heat from the surroundings and the top and bottom planes of the zone receive less heat.

To the best of our knowledge, there are only a few studies in literature considering the contributions of both thermal and solutal Marangoni convective flows in a full floating zone. Thus, to shed further light on the subject, the present study simulated a full zone system with radiative heat transfer under zero gravity including the effects of both thermal and solutal Marangoni convective flows in the melt.

3.2 Numerical methods

A full floating zone is simplified as a cylindrical liquid bridge, as shown in **Fig. 3-1**. Model assumptions, governing equations and numerical schemes are the same as those listed in *Numerical Methodology* in **Chapter II**. However, minor differences are listed below about the boundary conditions, especially the temperature field.

The temperature on both top and bottom planes is constant at a lower value of T_C. The ambient temperature (T_a) profile (distribution) as a function of height gives rise to the thermal Marangoni convection along the free surface. The Gaussian thermal profile (heat source) is assumed outside the floating zone in the vertical direction as

$$T_a = T_C + (T_H - T_C)exp\left[-\left(\frac{z-L/2}{a}\right)^2\right] \tag{15}$$

where T_C is the melting point, T_H is the maximum ambient temperature, L is the length of liquid bridge ($L = 0.01$ m), and a is the typical width of distribution ($a = 0.003$ m). The temperature boundary condition on the free surface follows "radiative heat transfer", as shown in Equation (10) in **Chapter II**. The aspect ratio ($A_s = L/R$) of liquid bridge is 1.0. Pr and Sc number are 6.37×10^{-3} and 14.0, respectively.

Besides, although the definition of Ma_T is the same as the one in Equation (12) in **Chapter II**, ΔT differs in the temperature difference between the maximum ambient temperature (T_H) and melting point (T_C).
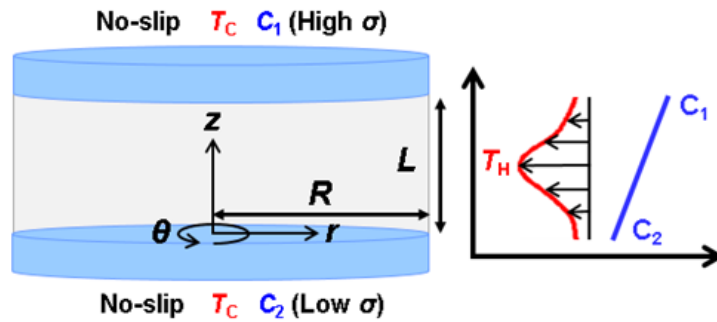

Fig. 3-1 Numerical model of liquid bridge as a full floating zone.

3.3 Mesh dependency

Before simulation, the mesh dependency has been tested at $Ma_C = 1786$ and $Ma_T = 2800$ by using different numerical mesh sizes in the r, θ, and z directions as shown in **Table 3-1**. The parameter of T_{max} stands for the maximum calculated temperature on the free surface. U_{1ave} and U_{2ave} are the average velocities in the z-direction at the sampling points of $(0.99R, 0, 0.25L)$ and $(0.99R, 0, 0.75L)$ in the liquid bridge.

Table 3-1 Numerical results with different mesh sizes at $Ma_C = 1786$ and $Ma_T = 2800$.

	Mesh	T_{max} **[K]**	U_{1ave} **[m/s]**	U_{2ave} **[m/s]**
1	$40^r \times 120^\theta \times 100^z$	1277.10	-0.00358	0.00369
2	$40^r \times 120^\theta \times 120^z$	1277.12	-0.00361	0.00370
3	$40^r \times 120^\theta \times 160^z$	1277.23	-0.00371	0.00374
4	$40^r \times 160^\theta \times 120^z$	1277.13	-0.00368	0.00373
5	$40^r \times 160^\theta \times 160^z$	1277.24	-0.00375	0.00379
6	$60^r \times 160^\theta \times 120^z$	1277.13	-0.00369	0.00372

From the above table, it is seen that values of T_{max}, U_{1ave}, and U_{2ave} are close at different mesh sizes. Given that the Marangoni flow develops along the free surface, the mesh in the θ and z directions should be adequate. Meanwhile, to save simulation time and cost, the mesh size of $40 \times 160 \times 120$ in the r, θ, and z directions, respectively, is applied in the simulation, as shown in **Fig. 3-2**.
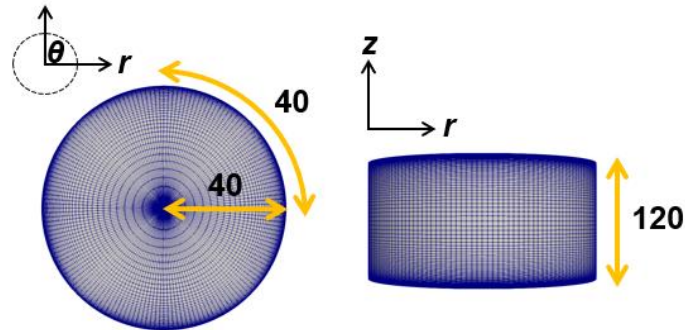

Fig. 3-2 Computational mesh applied in a full zone simulation. The mesh number in the r, θ, z directions are 40, 160, and 120, respectively. The total mesh number is 768,000.

3.4 Temperature distribution along the free surface

Fig. 3-3(a) shows the computed temperature field at $Ma_T = 2800$ and $Ma_C = 1072$, which is 2D symmetric in the z-direction. In this profile, the heat is concentrated on the equatorial plane of the liquid bridge, and the regions near the top and bottom planes receive the lowest heat from the ambiance. **Fig. 3-3(b) and (c)** show the snapshots of temperature field in the central r-z plane at $Ma_T = 700$ and 2100, respectively. The temperature distribution is almost symmetric with the equatorial region receiving the largest heat. The temperature gradients are almost existing in the vertical direction near the free surface, where thermal Marangoni convection dominants.

(a)

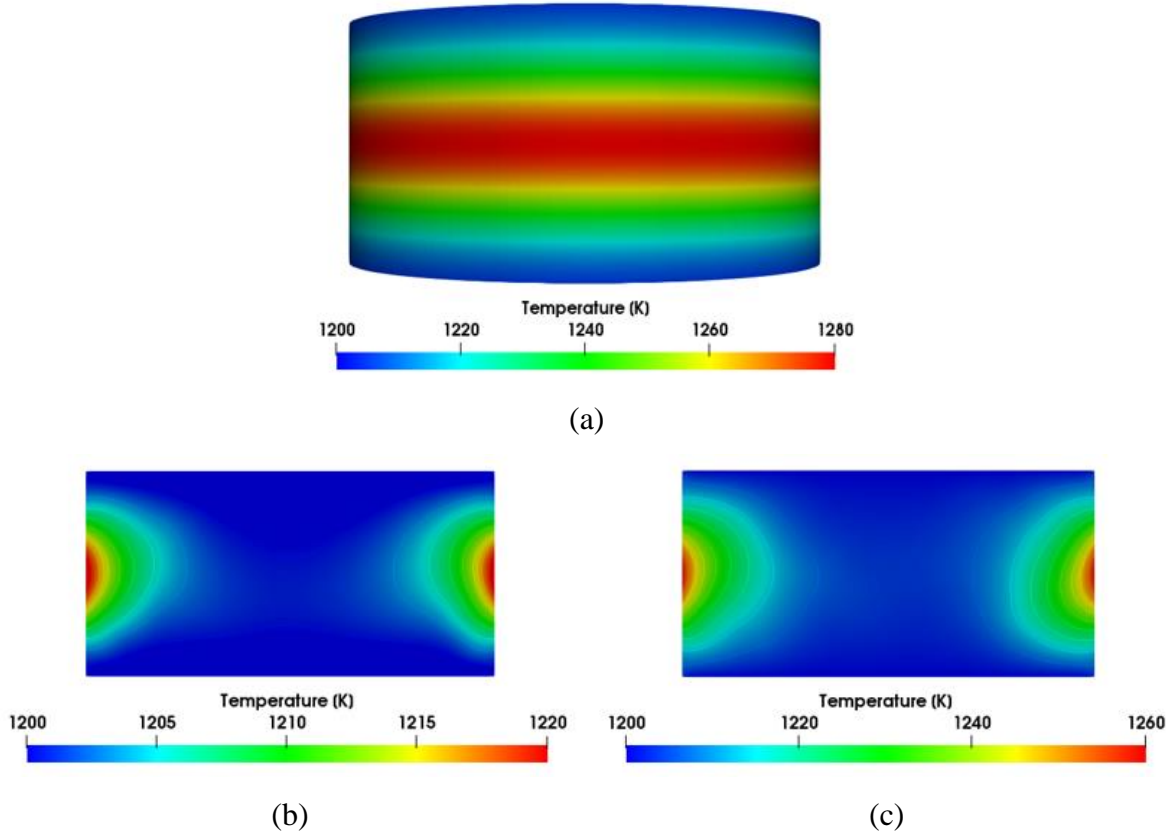(b)   (c)

Fig. 3-3 (a) Temperature field of liquid bridge at $Ma_T = 2800$ and $Ma_C = 1072$. (b) Snapshots of temperature field in the central r-z plane at $Ma_T = 700$ and $Ma_C = 1072$. (c) Snapshots of temperature field in the central r-z plane at $Ma_T = 2100$ and $Ma_C = 1072$.

Fig. 3-4 shows the temperature distribution on the free surface at different Ma_T values, which is in the Gaussian profile. These temperature differences on the free surface give rise to the development of the thermal Marangoni convection in the zone.

As seen in **Figs. 3-3** and **3-4**, the temperature distribution is not affected by Marangoni convection in the range of present simulation due to the small Pr number.
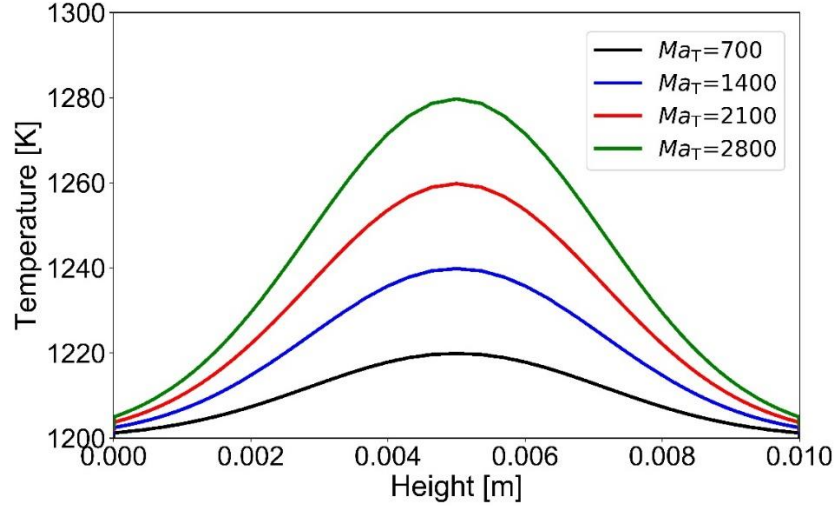

Fig. 3-4 Temperature distribution along the free surface at different Ma_T values.

3.5 Thermal and solutal Marangoni convection in a full floating zone at $Ma_C = 1072$ and different Ma_T values.

Fig. 3-5 shows the snapshots of the computed Si concentration distribution along the r-θ plane from the top view at the height of $z/L = 0.25$ and $z/L = 0.75$ at $Ma_C = 1072$ and $Ma_T = 700$, 1400, 2100, and 2800. The bottom graphs in **Fig. 3-5** are taken from the height of $z/L = 0.25$, where the thermal and solutal Marangoni convective flows are in the opposite direction (lower part of the liquid bridge). The 2D axisymmetric flow pattern is observed at a smaller Ma_T value ($Ma_T = 700$). As Ma_T increases, the flow pattern behaves chaotically at $Ma_T = 1400$ or 2100 with the irregular azimuthal wave. It becomes diverging at $Ma_T = 2800$. In the lower liquid region, we may consider the flow pattern varies due to different Ma_T values. Meanwhile, the top graphs in **Fig. 3-5** are taken from the height of $z/L = 0.75$, where the thermal and solutal Marangoni convective flows are in the same direction (upper part of the

liquid bridge). In this region, at a larger Ma_T ($Ma_T = 1400$ or 2100), the azimuthal wave pattern can be observed, which is quasi-symmetric, and the augmented effect of thermal and solutal Marangoni convection gives rise to a flow instability. In the middle part of **Fig. 3-5**, the flow patterns at the central r-z plane are shown at various Ma_T values. The strength of thermal and solutal Marangoni convection becomes stronger and more complex with the increase of Ma_T.
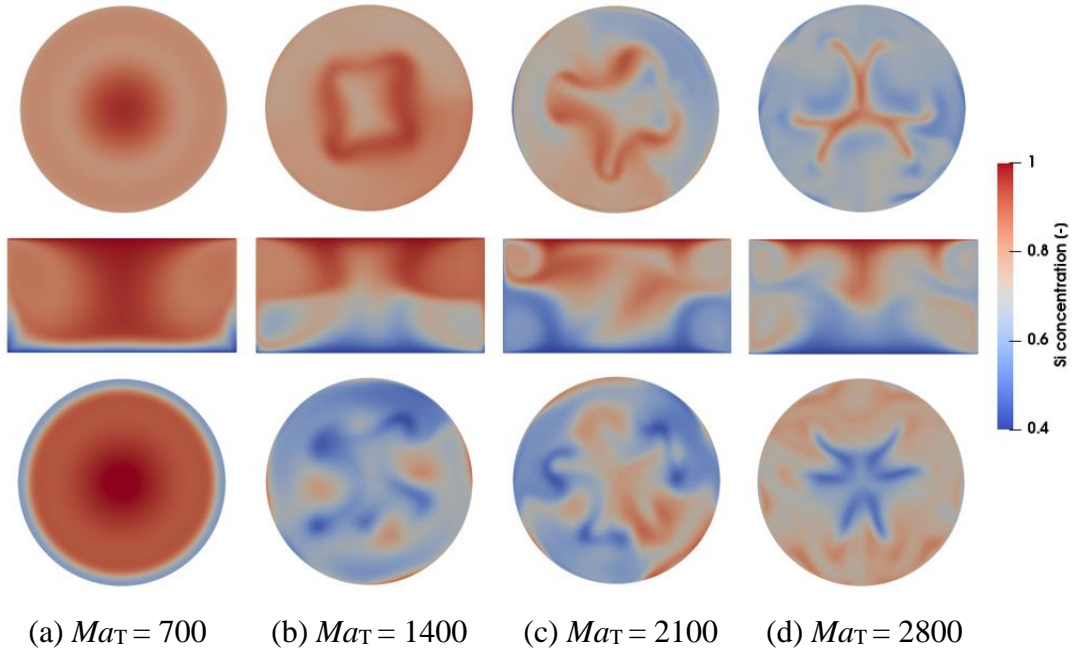

(a) $Ma_T = 700$ (b) $Ma_T = 1400$ (c) $Ma_T = 2100$ (d) $Ma_T = 2800$

Fig. 3-5 Snapshots of Si concentration distribution at the r-θ plane at the height of $z/L = 0.25$ (Bottom) and 0.75 (Top), and central r-z plane (Middle) at $Ma_C = 1072$ with different Ma_T values at $t = 500$ s.

Fig. 3-6 shows the computed velocity vectors at the central r-z plane from the front view at $Ma_C = 1072$ and different Ma_T values at $t = 500$ s. When Ma_T is small ($Ma_T = 700$), there are two vortices along the free surface near the top plane, which means the flow in the lower region is suppressed. With the increase of Ma_T, there appear four vortices along the free surface near both the top and bottom planes. As Ma_T increases further, the flow becomes stronger near the top and bottom planes.
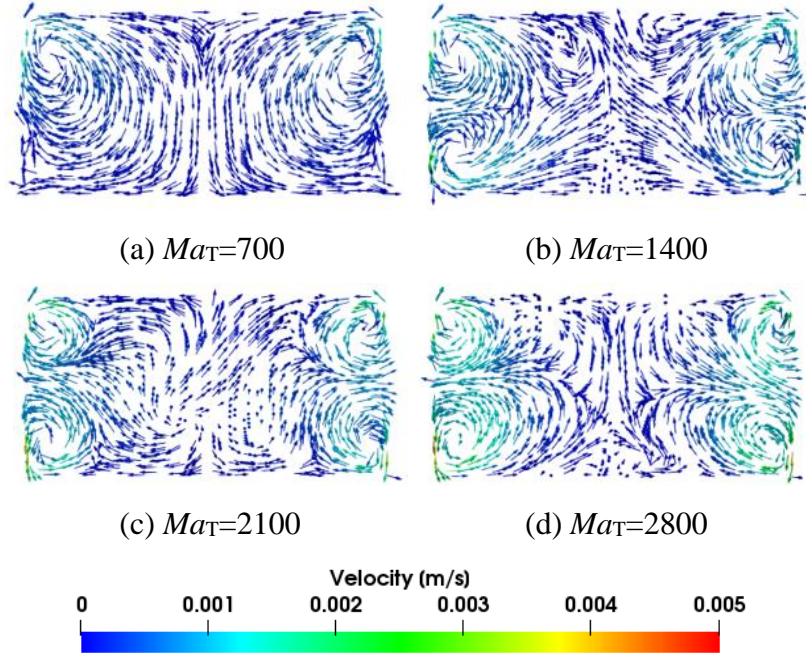
(a) Ma_T=700   (b) Ma_T=1400

(c) Ma_T=2100   (d) Ma_T=2800

Velocity (m/s)

0   0.001   0.002   0.003   0.004   0.005

Fig. 3-6 Flow velocity vectors at the central r-z plane at $Ma_C = 1072$ and different Ma_T values at $t = 500$ s.

Fig. 3-7 shows the vertical time-averaged velocity on the free surface at $Ma_C = 1072$ and $Ma_T = 0$, 700, 1400, 2100, and 2800. At $Ma_T = 0$, the magnitude of pure solutal Marangoni convection is weak, and the consideration of thermal Marangoni convection can affect the shape of the free surface velocity. At $Ma_T = 700$, the velocity is very weak in the lower region, where thermal and solutal Marangoni convection are suppressed. At the higher Ma_T values, the peak value of velocity appears around the height of 0.2 L and 0.8 L, where the strong vortices form in these regions. The velocity fluctuates around zero when we observe the sampling point at the middle height of the liquid bridge ($z/L = 0.5$). Therefore, from the bottom to the top plane, the variation of the vertical velocity undergoes a sharp increase to a peak value then reduces to zero in the middle, and a reverse increase to a peak value again near the top plane. Additionally, it is noted that very small vortices develop near the bottom plane, especially at larger Ma_T values.
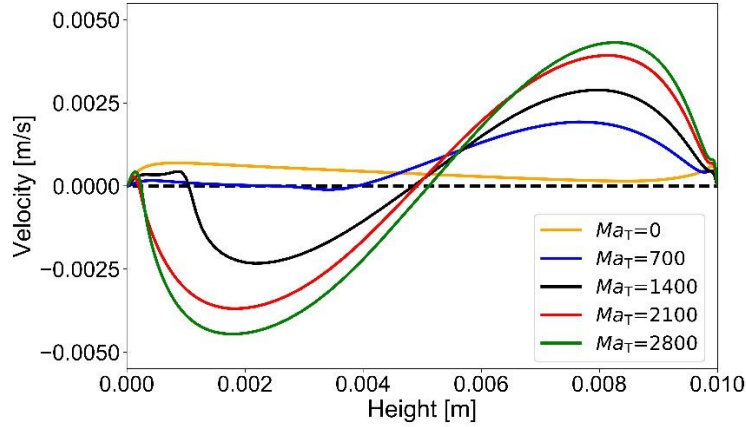
Fig. 3-7 Time-averaged free surface velocity at $Ma_C = 1072$ and different Ma_T values.

3.6 Thermal and solutal Marangoni convection in a full floating zone at $Ma_C = 1786$ and different Ma_T values.

Fig. 3-8 shows the snapshots of the Si concentration distribution along the r-θ plane from the top view at the height of $z/L = 0.25$ and $z/L = 0.75$ at $Ma_C = 1786$ and $Ma_T = 700$, 1400, 2100, and 2800. The bottom graphs are taken from the height of $z/L = 0.25$, which show a transition from a 2D axisymmetric flow to a chaotic flow, with an irregular azimuthal wave pattern pulsating in the θ-direction. The top graphs are taken from the height of $z/L = 0.75$, and as seen, the patterns are much simpler and gentler compared with those at $z/L = 0.25$ at the larger Ma_T values.

Fig. 3-9 shows the computed flow velocity vectors at the central r-z plane from the front view at $Ma_C = 1786$ and different Ma_T values at $t = 500$ s. Comparing them with those in **Fig. 3-6**, we see that the flow becomes stronger. As also seen, there are two vortices at $Ma_T = 700$ and 1400 which are smaller than the value of Ma_C calculated, while four vortices form at the larger Ma_T values with higher instability.

Fig. 3-10 shows the vertical velocity at the sampling points of $(0.99R, 0, 0.25L)$, $(0.99R, 0, 0.50L)$, and $(0.99R, 0, 0.75L)$ at $Ma_C = 1786$ and $Ma_T = 1400$ and 2800. At a smaller Ma_T value, the vertical velocity near the lower sampling point of the liquid bridge becomes around zero after slight fluctuations. The velocity at the upper point is larger than that of the lower point, with the augmentation of thermal and solutal Marangoni flow. At a larger Ma_T value,

the velocity field at the sampling points shows fluctuations with time. The time-averaged velocity values of the symmetric points at $(0.99R, 0, 0.25L)$ and $(0.99R, 0, 0.75L)$ are similar.

(a) $Ma_T = 700$ (b) $Ma_T = 1400$ (c) $Ma_T = 2100$ (d) $Ma_T = 2800$
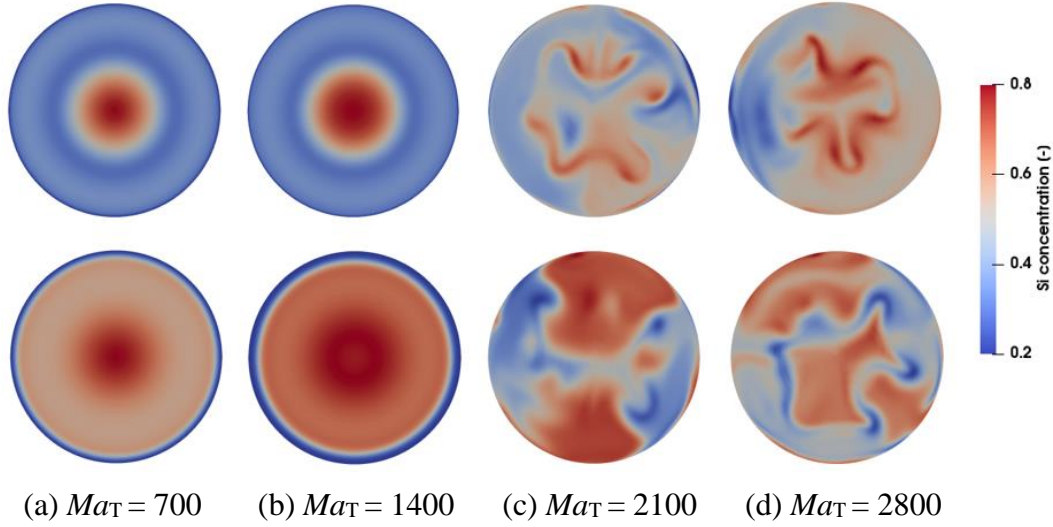
Fig. 3-8 Snapshots of Si concentration distribution at the r-θ plane at the height of $z/L = 0.25$ (Bottom) and 0.75 (Top) at $Ma_C = 1786$ with different Ma_T values at $t = 500$ s.

(a) $Ma_T=700$ (b) $Ma_T=1400$

(c) $Ma_T=2100$ (d) $Ma_T=2800$
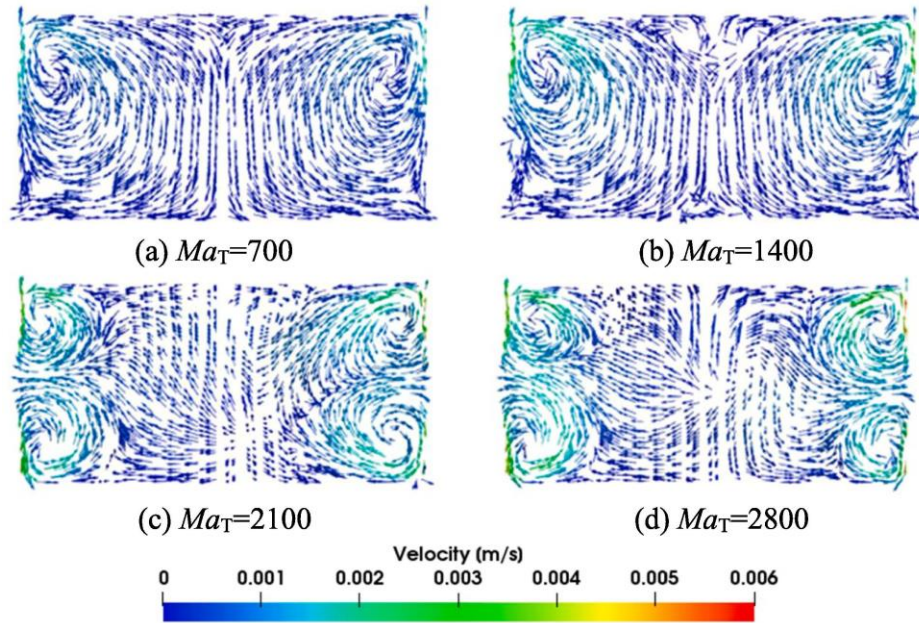
Fig. 3-9 Flow velocity vectors at the central r-z plane at $Ma_C = 1786$ and different Ma_T values at $t = 500$ s.
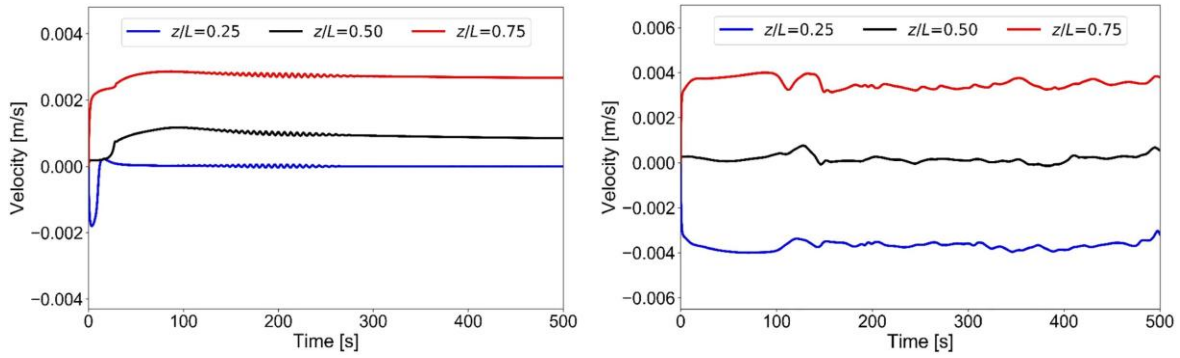
Fig. 3-10 Vertical flow velocity at the sampling points of (0.99*R*, 0, 0.25*L*), (0.99*R*, 0, 0.50*L*), and (0.99*R*, 0, 0.75*L*) at Ma_C = 1786 and Ma_T = 1400 (left) and 2800 (right).

3.7 Summary

The characteristics of the concentration pattern in the zone vary due to the varying thermal and solutal Marangoni numbers, as well as the characteristic azimuthal wave. The flow velocity field exhibits two or four main vortices along the free surface by effects of suppression or augmentation of thermal and solutal Marangoni convection. These vortices get stronger at higher thermal Marangoni numbers.

Chapter IV Characterization of Thermal and Solutal Marangoni Convection of Opposite Directions in a Half Floating Zone

In this chapter, numerical simulation of thermal and solutal Marangoni convection of opposite directions in a half floating zone under zero gravity has been performed. The separated lower-half zone is selected as the numerical domain with considering various combinations of (Ma_C, Ma_T). Due to the complexity of the opposite-direction flow, the supercomputer is required to conduct the simulation.

4.1 Relevant studies on the combined thermal and solutal Marangoni convection

Since solutal Marangoni convection plays an important role in crystal growth by the FZ method, as stated in **Chapter I**, it is necessary to consider the dual effects of thermal and solutal Marangoni convection in a half floating zone.

Some studies focused on the dual effects of two Marangoni convections. Chen *et al.* [83] studied thermal and solutal Marangoni convection in a two-dimensional (2D) rectangular cavity where the thermal and solutal Marangoni flows are opposite to each other with equal magnitudes. It is predicted that a no-flow state remains stable up to a critical thermal Marangoni number. Wu *et al.* [91] also investigated thermal and solutal Marangoni convection in a rotating cylinder where the thermal and solutal Marangoni flows were in opposite directions with equal strengths. They proposed to control instability by disk rotation.

In our previous study, Minakuchi *et al.* [73, 74] investigated the combined effects of thermal and solutal Marangoni convection in a half floating zone. In their system, the thermal and solutal Marangoni flows developing in the melt are in the same direction (upper-half zone). Their study predicts that the concentration pattern becomes three-dimensional (3D) and unsteady under a large temperature difference along the free surface. The predicted 3D flow pattern also shows an *m*-fold symmetry in the azimuthal direction (where *m* is the azimuthal wave number), and *m* increases if the flow loses its stability further.

However, the overall characterization of thermal and solutal Marangoni convective flow of opposite directions in a liquid bridge has not been reported in the literature. We guess the

29

phenomenon would be different from that of the same direction. Therefore, we focus on the phenomenon of thermal and solutal Marangoni convection of opposite directions (lower-half zone) at various Marangoni ratios and explore the unique characteristics of flow regimes that are different from those of the same direction.

4.2 Half floating zone

A lower-half floating zone is selected as the numerical domain to investigate the mechanism of the combined thermal and solutal Marangoni convection of opposite directions in the melt. A half zone model simulates half of a real floating zone. The presence of heating coins in a full zone model is simulated by heating one of the supporting planes, where heat transfer is neglected through the free surface. Surface tension-driven force induces Marangoni convection with a single toroidal vortex.
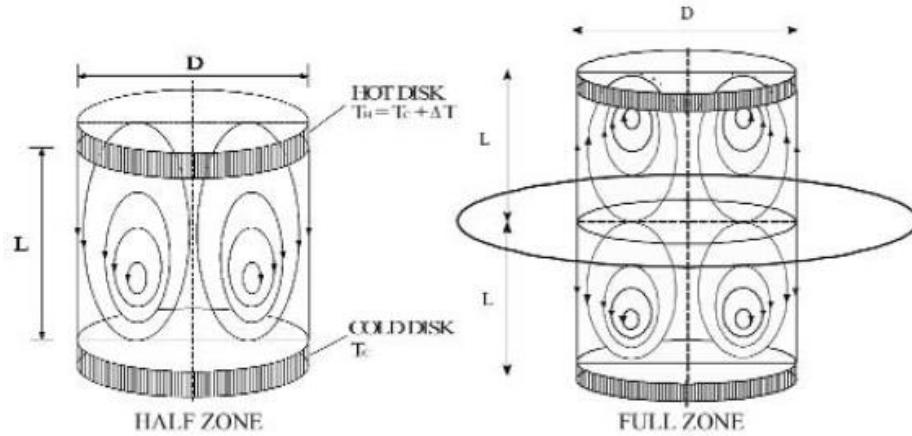
Fig. 4-1 Configurations of a half floating zone (left) and a full floating zone (right). [87]

The configurations of a half and full floating zone and their differences are shown in **Fig. 4-1 [87]** and **Table 4-1** below. The dominant difference is whether a heater is set outside the floating zone and thus thermal boundary condition is different, depending on whether heat transfer between floating zone and ambience is taken into consideration. In this chapter, we assume an adiabatic free surface between top and bottom planes to emphasize the flow phenomenon itself inside a half floating zone without consideration of heat transfer from ambience, which ensures that thermal Marangoni convection develops due to the temperature

30

difference between two planes. Effects of heat transfer in a half floating zone will be discussed in **Chapter V**.

Table 4-1 Comparison of a half floating zone in the present research and a full floating zone.

	Half zone	Full zone
Heater	×	Heating coils
Surface heating	×	Ambient temperature / Heat flux
Boundary condition	Adiabatic	Radiative heat transfer
Thermal Marangoni convection	ΔT between the cold and hot plane	ΔT between the cold planes and hot free surface

This half zone model has distinct advantages. In particular, the ends of domain are isothermal, the interface is adiabatic and the applied temperature difference driving thermal Marangoni convection can be fixed a priori in the analysis. If under normal-gravity conditions, the upper half of the full zone is influenced by buoyancy force so that Marangoni convection can hardly be recognized. On the other hand, the lower half is less affected by buoyancy since the upper temperature is higher. Consequently, Marangoni convection dominates in the lower half zone. For this reason, the lower half zone is preferred in the normal-gravity research.

4.3 Numerical methods

A half floating zone is simplified as a cylindrical liquid bridge, as shown in **Fig. 4-2**. Model assumptions, governing equations and numerical schemes are the same as those listed in *Numerical Methodology* in **Chapter II**. However, minor differences are listed below about the boundary conditions, especially the temperature field.

In order to create thermal and solutal Marangoni convections of opposite directions, a higher temperature was imposed on the top plane, while a lower temperature on the bottom plane. Because of the negative value of surface tension coefficient of temperature ($\partial \sigma / \partial T < 0$), thermal Marangoni convection is from the top to the bottom plane. To the contrary,

solutal Marangoni convection flows from the bottom to the top plane by imposing a mixture of Si and Ge on the bottom and pure Si on the top, due to the positive value of surface tension coefficient of concentration ($\partial\sigma/\partial C > 0$).
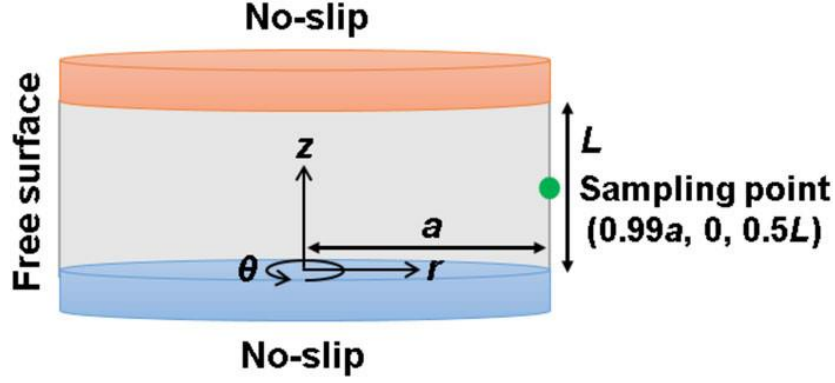

Fig. 4-2 Configuration of a cylindrical half-zone liquid bridge. The bottom plane is cooler, and the top plane is hotter. The bottom plane has a lower concentration of silicon.

To emphasize the opposite flow directions of thermal and solutal Marangoni convection. definitions of thermal and solutal Marangoni number are adjusted to make Ma_T negative and Ma_C positive. These slight changes are suitable in the whole chapter.

$$Ma_\mathrm{T} = \frac{\partial\sigma}{\partial T} \cdot \frac{\Delta TL}{\mu v} \tag{12-1}$$

$$Ma_\mathrm{C} = \frac{\partial\sigma}{\partial C} \cdot \frac{\Delta CL}{\mu v} \tag{13-1}$$

where $\Delta T = T_{top} - T_{bottom} > 0$ and $\Delta C = C_{top} - C_{bottom} > 0$ are the temperature and concentration differences between top and bottom planes.

Furthermore, in this chapter, Marangoni ratio ($R_\sigma = Ma_\mathrm{T}/Ma_\mathrm{C}$) is negative since $Ma_\mathrm{T} < 0$. Ma_C is ranged from 0 to 1786, and Ma_T varies from 0 to -3500. The negative symbol only represents the direction of thermal Marangoni flow is opposite to solutal one. *Pr* and *Sc* number are 6.37×10^{-3} and 14.0, respectively. The aspect ratio of liquid bridge is 0.5.

4.4 Dimensionless governing equations and boundary conditions

In this chapter, all of the numerical results are analyzed in a dimensionless form. Thus, dimensionless governing equations and boundary conditions are given below.

Governing equations of (1) ~ (4) are given in a dimensionless form below using the following characteristic values, length L, time L^2/ν, and velocity ν/L:

$$\nabla \cdot v^* = 0 \tag{D-1}$$

$$\frac{\partial v^*}{\partial t^*} + v^* \cdot \nabla v^* = -\nabla p^* + \nabla^2 v^* \tag{D-2}$$

$$\frac{\partial T^*}{\partial t^*} + v^* \cdot \nabla T^* = \frac{1}{Pr}\nabla^2 T^* \tag{D-3}$$

$$\frac{\partial C^*}{\partial t^*} + v^* \cdot \nabla C^* = \frac{1}{Sc}\nabla^2 C^* \tag{D-4}$$

where $(\cdot)^*$ represents the dimensionless variable.

Boundary conditions of Marangoni convection of (5) ~ (7) in a dimensionless form are given as:

$$v_r^* = 0 \tag{D-5}$$

$$r^* \frac{\partial}{\partial r^*}\left(\frac{v_\theta^*}{r^*}\right) = \frac{1}{r^*}\left(Ma_\text{T}\frac{\partial T^*}{\partial \theta^*} + Ma_\text{C}\frac{\partial C^*}{\partial \theta^*}\right) \tag{D-6}$$

$$\frac{\partial v_z^*}{\partial r^*} = Ma_\text{T}\frac{\partial T^*}{\partial z^*} + Ma_\text{C}\frac{\partial C^*}{\partial z^*} \tag{D-7}$$

Dimensionless temperature and concentration gradients in the radial direction along the free surface follows "zero-gradient":

$$\frac{\partial T^*}{\partial r^*} = 0 \tag{D-8}$$

$$\frac{\partial C^*}{\partial r^*} = 0 \tag{D-9}$$

4.5 Characterization of thermal and solutal Marangoni convection of opposite directions

The computed flow regimes are summarized in **Fig. 4-3** with respect to different thermal and solutal Marangoni numbers. The flow regimes in this map are identified in the r-θ plane at $z/L = 0.5$. The black dashed line represents the condition of $R_\sigma = -1$. In terms of creating the initial condition at different Ma_C and Ma_T values, at first, Ma_C is increased in time with a constant rate of $\Delta Ma_\text{C}/\Delta t^* \approx 32.1$ and then stays constant at $Ma_\text{C} = (179, 357, 536, 714, 893, 1072, 1250, 1429, 1607, 1786)$ in order to investigate the fully developed Marangoni convection with $Ma_\text{T} = 0$. Then, Ma_T is decreased from 0 to -3500 with $-\Delta Ma_\text{T}/\Delta t^* \approx 62.5$

at each Ma_C, and the statistical equilibrium state is achieved corresponding to the constant values of Ma_C and Ma_T.

When Ma_T is decreased, the temperature field is almost steady with an axisymmetric structure, as shown in **Fig. 4-4**. This prediction is due to the very low Pr value of the melt. **Fig. 4-5** shows the computed temperature deviations from the quasi-laminar linear profile ($T^* = z^*$) in the z-direction at $r/a = 0$, 0.50, and 0.99 for $(Ma_C, Ma_T) = (1072, -3500)$. As seen, the deviations are within $\pm 5\%$, which means that the temperature field almost remains 2D axisymmetric. Therefore, in the rest of this study, we only focus on the concentration and velocity fields.
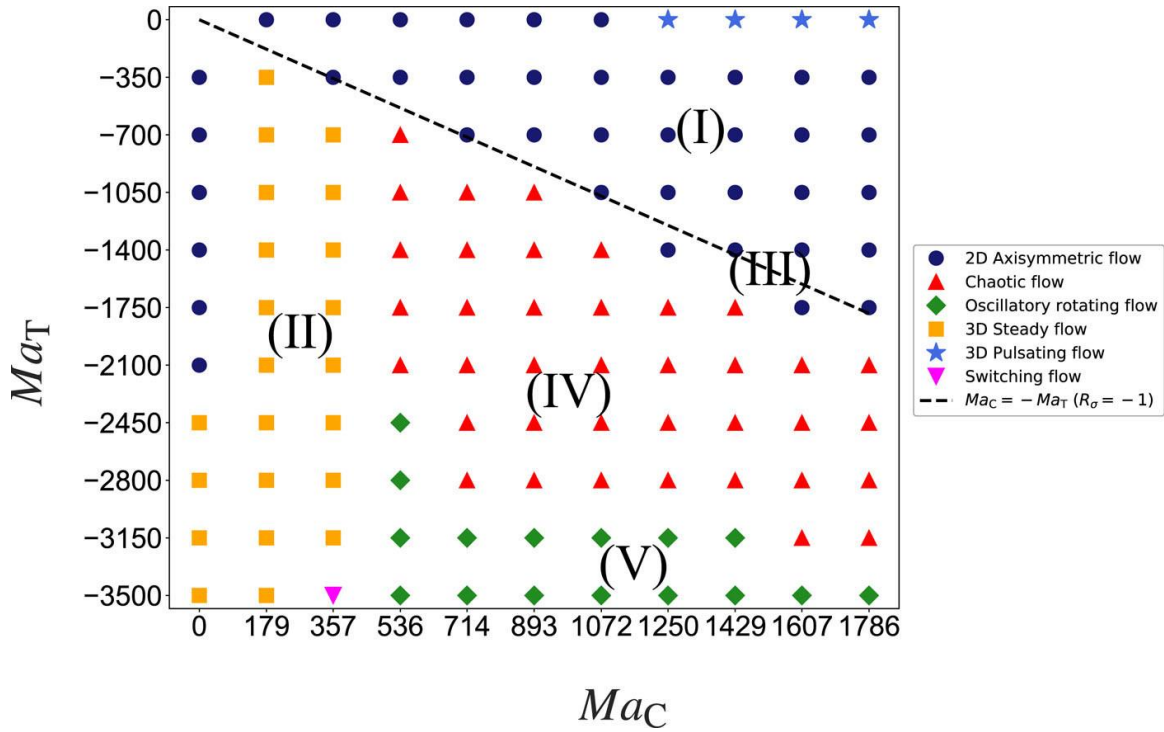

Fig. 4-3 (Ma_C, Ma_T) map of flow regimes.

When only solutal Marangoni convection is considered ($Ma_T = 0$), i.e., the points in the first row (from top) of **Fig. 4-3**, the flow is 2D axisymmetric when Ma_C is small ($Ma_C <$ 1200). The concentration patterns become 3D unsteady at higher values of $Ma_C \gtrsim 1200$ with pulsations as shown in **Fig. 4-6**. The concentration field pulsates as traveling waves of expansion and compression in a period of $T_p^* = 0.35$ with the azimuthal wave number ($m =$

4). The critical value of Ma_C at $Ma_T = 0$ is roughly 1100, which is in agreement with that of Minakuchi *et al* [73].
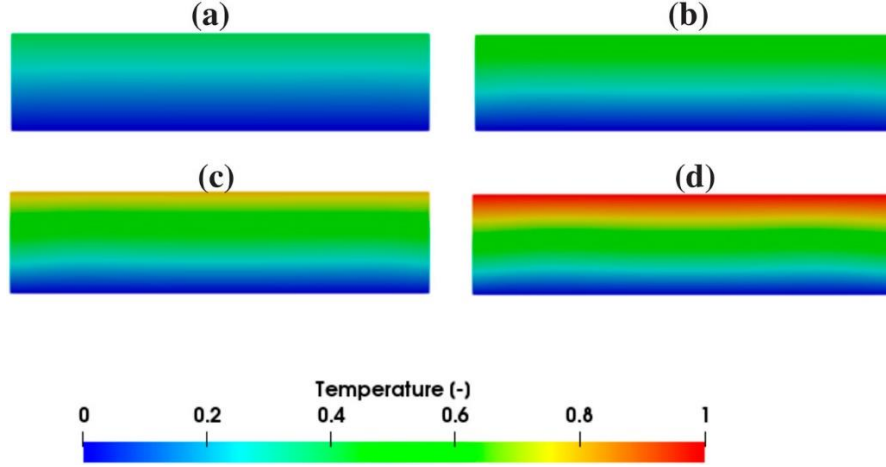

Fig. 4-4 Nondimensional temperature distribution in the vertical r-z plane, $T^*(r, z)$, at $Ma_C = 1072$: (a) $Ma_T = -1400$, (b) $Ma_T = -2100$, (c) $Ma_T = -2800$, and (d) $Ma_T = -3500$.
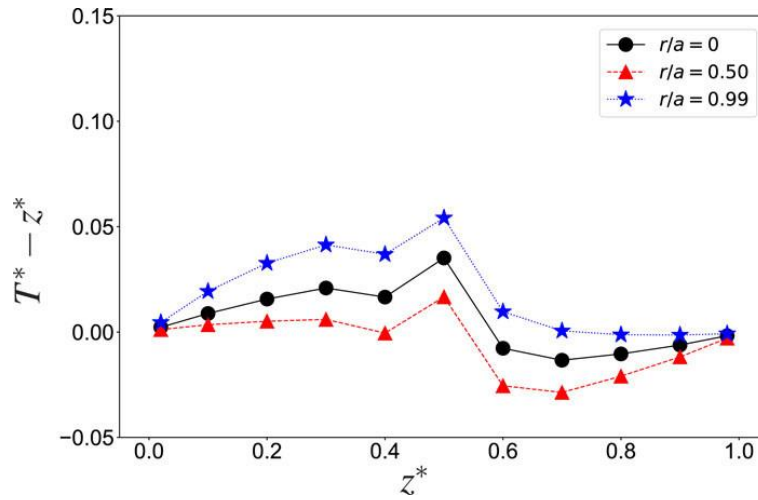
Fig. 4-5 Temperature deviations from the quasi-laminar profile ($T^* = z^*$) in the vertical direction with $r/a = 0$, 0.50, and 0.99 at $(Ma_C, Ma_T) = (1072, -3500)$.

When we consider both thermal and solutal Marangoni flows, the flow regime becomes more complicated, which is highly dependent on the Marangoni ratio R_σ and the quantitative relationship between Ma_C and Ma_T. The flow regimes can be characterized as follows:

(I)   2D axisymmetric flow: at $-1 < R_\sigma < 0$ with $Ma_C > -Ma_T$.

(II) 3D steady flow with a symmetric azimuthal wave: at $R_\sigma < -1$ with small Ma_C ($Ma_C \lesssim 360$).

(III) Periodic flow: at $R_\sigma \approx -1$, where $-Ma_T$ is approximately equal to Ma_C.

(IV) Chaotic flow: at $R_\sigma < -1$ with moderate $|Ma_T|$ at $Ma_C \gtrsim 530$.

(V)   Oscillatory flow with a rotating azimuthal wave: at $R_\sigma < -1$ with large $|Ma_T|$ at $Ma_C \gtrsim 530$.

In the following subsections, the concentration pattern in each flow regime, i.e., (I) - (V), and the critical transitions are examined in detail.
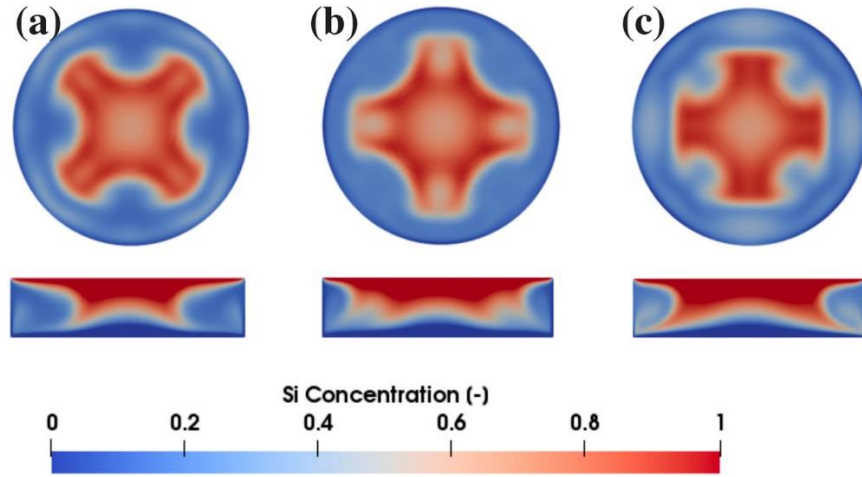

Fig. 4-6 Nondimensional concentration distribution of Si in the r-θ plane at $z/L = 0.5$ and the vertical r-z plane with 3D pulsating traveling waves during a period at $(Ma_C, Ma_T) = (1429, 0)$: (a) $t^*/T_p^* = 0$, (b) 1/3, and (c) 2/3.

4.6 Transition from a 2D axisymmetric regime (regime I) to a 3D steady regime (regime II) with a symmetric azimuthal wave

When $Ma_C > -Ma_T$ ($-1 < R_\sigma < 0$), a 2D axisymmetric steady flow regime is observed. The corresponding concentration field is shown in **Fig. 4-7(a)** and **(b)**. In this case, since the thermal and solutal Marangoni flows are in opposite directions, they are competing and weakening each other gradually with the increase in $|Ma_T|$. The concentration pattern in the central r-z plane indicates that Marangoni convection is weak along the free surface.
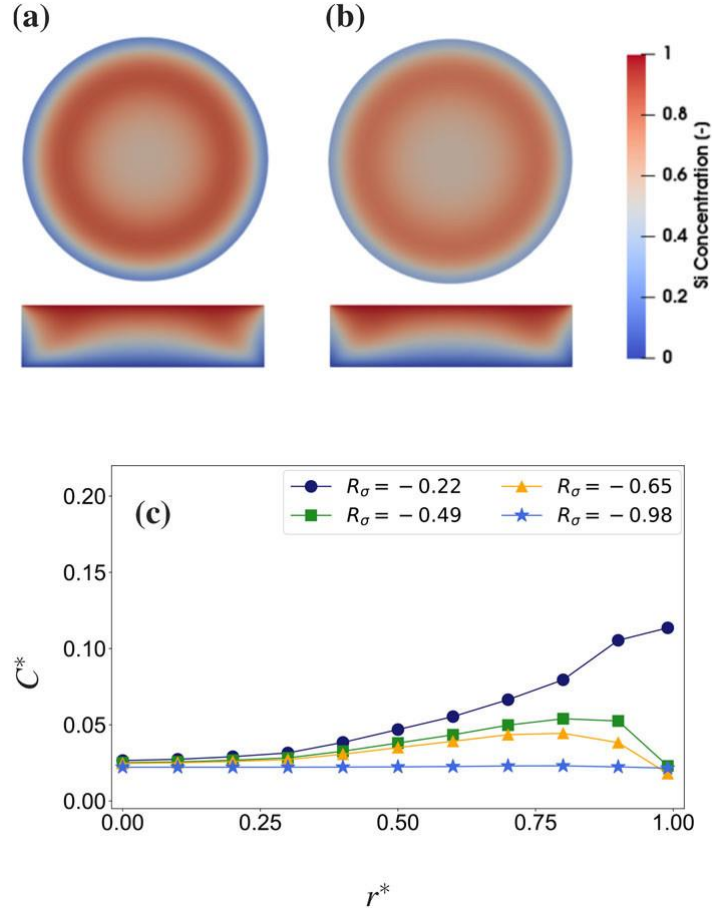
Fig. 4-7 (a, b) Nondimensional concentration distribution of Si with $-1 < R_\sigma < 0$ ($Ma_C > -Ma_T$) in the r-θ plane at $z/L = 0.5$ and the vertical r-z plane: (a) (Ma_C, Ma_T) = (714, −350) and (b) (Ma_C, Ma_T) = (1607, −1050). (c) Nondimensional concentration distribution of Si in the radial direction at $z/L = 0.02$ of regime I.

Fig. 4-7(c) presents the computed concentration distribution of Si at $z/L = 0.02$ (near the bottom) in the r-direction under different values of R_σ. This plot is important and can be used to make predictions for the uniformity of the growing crystal. Under the condition of $-1 < R_\sigma < 0$, the concentration distribution tends to be constant and uniform in the central region ($r^* < 0.50$), while we see some weak fluctuations near the free surface ($0.75 < r^* < 1$). As seen, if R_σ is close to −1 ($Ma_C = -Ma_T$), the concentration distribution is very uniform, i.e., $R_\sigma = -0.98$. It can be concluded that the condition of $-1 < R_\sigma < 0$ is beneficial in growing

crystals with higher uniformity, which resulted from the fact that the competing thermal and solutal Marangoni flows are weakening each other in this case.

When only thermal Marangoni convection is considered, i.e., the points in the first column (from left) of **Fig. 4-3**, as $|Ma_T|$ is greater than 2450, the flow regime is 3D stationary and steady with the m-folded symmetric azimuthal wave as shown in **Fig. 4-8(a)**. When Ma_C is relatively small (i.e., $Ma_C \lesssim 360$), the wave number changes as $|Ma_T|$ increases, as shown in **Fig. 4-8(b)-(e)**. **Fig. 4-9** shows the relationship between azimuthal wave number (m) and thermal Marangoni number (Ma_T) with respect to solutal Marangoni number (at $Ma_C = 0$, 179, and 357). As Ma_T decreases beyond $Ma_T \approx -1000$, the azimuthal wave number also decreases, i.e., from $m = 4$ to 3 at $Ma_C = 179$ and from $m = 7$ to 3 at $Ma_C = 357$. Therefore, in regime II, we predict that a relatively higher Ma_C value (i.e., $Ma_C = 357$) can give rise to the steady flow regime with higher azimuthal wave numbers ($m = 5 \sim 7$).

Note that an isolated switching flow is shown in **Fig. 4-3** at $(Ma_C, Ma_T) = (357, -3500)$. At this point, the azimuthal wave is similar to the pattern of regime II; however, it varies chaotically with time and the wave pattern becomes irregular, as shown in **Fig. 4-10**.
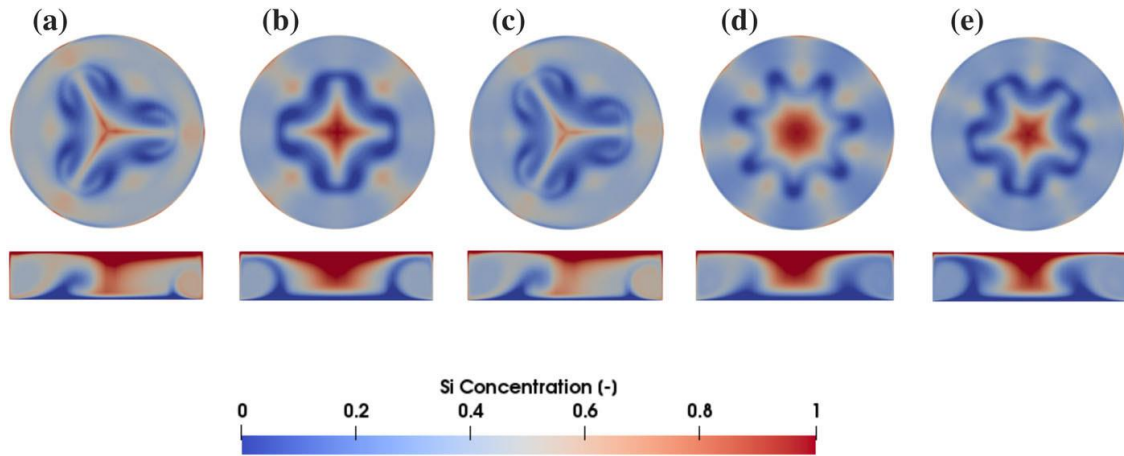

Fig. 4-8 Nondimensional concentration distribution of Si at relatively small Ma_C ($Ma_C \lesssim 360$, regime II) in the r-θ plane at $z/L = 0.5$ and the vertical r-z plane: (a) $(Ma_C, Ma_T) = (0, -2800)$, (b) (179, -1750), (c) (179, -3150), (d) (357, -1400), and (e) (357, -2100).
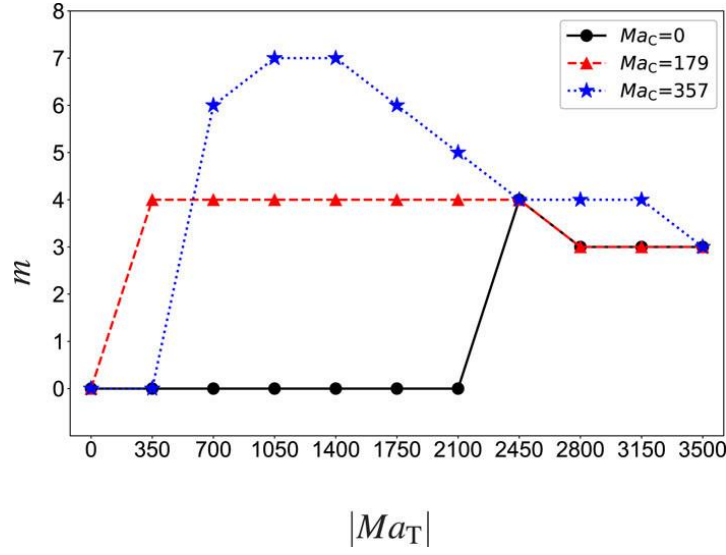
Fig. 4-9 Azimuthal wave number (m) as a function of thermal Marangoni number ($|Ma_T|$) with respect to Ma_C (Ma_C = 0, 179, 357) for the case of a 3D steady convective flow ($0 \lesssim Ma_C \lesssim 360$, regime II).
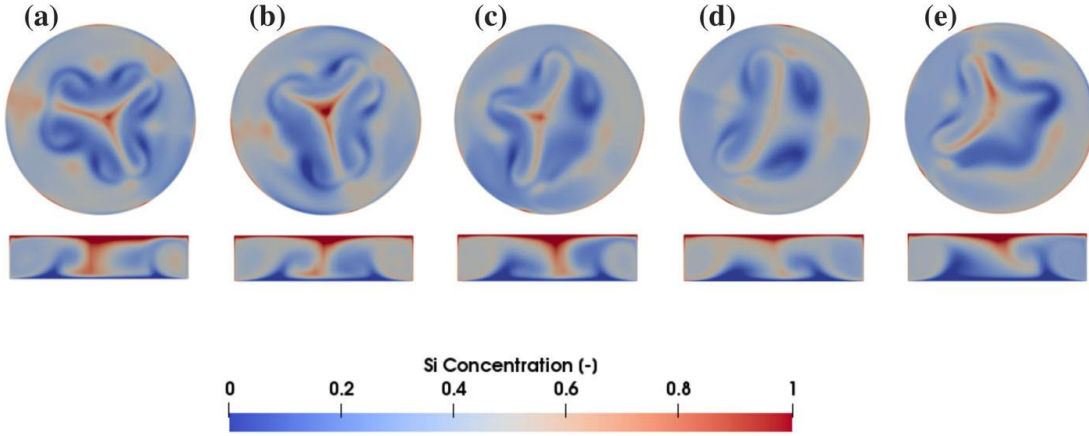
Fig. 4-10 Nondimensional concentration distribution of Si with time at (Ma_C, Ma_T) = (357, −3500) in the r-θ plane at z/L = 0.5 and the vertical r-z plane: (a) $t^* = 3.472$, (b) $t^* = 3.696$, (c) $t^* = 3.920$, (d) $t^* = 4.144$, and (e) $t^* = 4.368$.

4.7 The periodic flow – regime III

At $Ma_C \approx -Ma_T$ ($R_\sigma \approx -1$), the computed concentration field of Si, shown in **Fig. 4-11(a)** and **(b)**, exhibits a 2D axisymmetric pattern with weak and periodic oscillations. In this case, the strengths of thermal and solutal Marangoni flows are roughly equal and the total combined Marangoni flow strength is weakened due to their competing effects.

However, since these two flows do not eliminate their opposing effects completely, there still remains a weak and periodic flow in the liquid bridge.
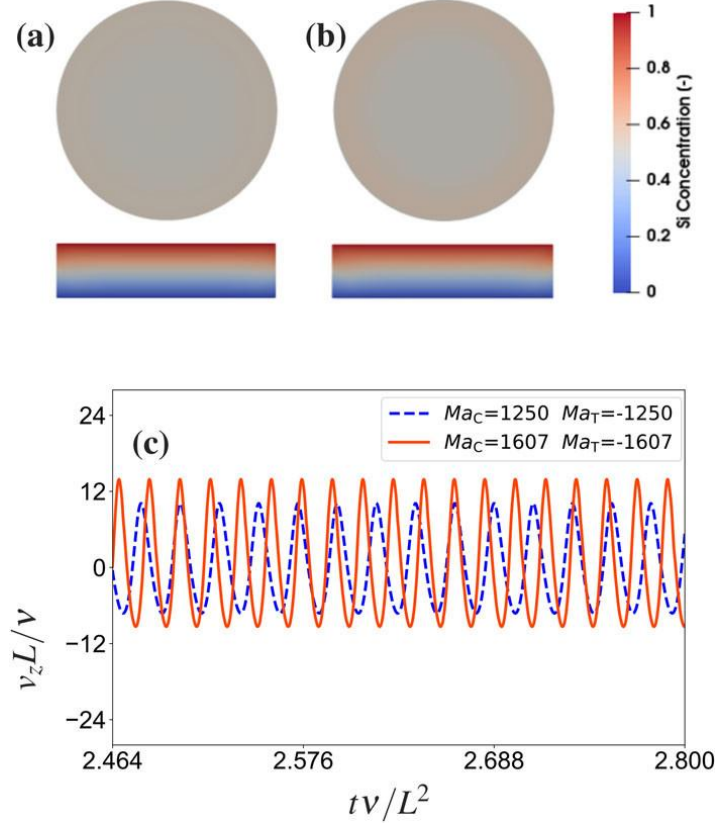
Fig. 4-11 (a, b) Nondimensional concentration distribution of Si with $R_\sigma = -1$ ($Ma_C = -Ma_T$) in the r-θ plane at $z/L = 0.5$ and the vertical r-z plane: (a) (Ma_C, Ma_T) = (1250, −1250) and (b) (Ma_C, Ma_T) = (1607, −1607). (c) Velocity in the vertical direction, v_z^*, at the sampling point (0.99a, 0, 0.5L) of regime III.

Fig. 4-12 shows the flow velocity variation, which is represented by the difference of the maximum and minimum flow velocities and the non-dimensional time period (T_p^*) of the periodic flow at the sampling point (0.99a, 0, 0.5L). As Ma (= $Ma_C = -Ma_T$) increases, the fluctuation increases monotonically. It is almost linear above $Ma \gtrsim 700$. On the other hand, the time period of the fluctuation decreases, which means that it oscillates with higher frequencies, i.e., $f^* = 49.6$ for $Ma_C = -Ma_T = 1429$ and $f^* = 62.4$ for $Ma_C = -Ma_T = 1786$. The flow is relatively weak even at a large Ma, and therefore, the whole concentration pattern

remains 2D axisymmetric. When Ma_C is small enough ($Ma_C \lesssim 360$), the vertical velocity at the sampling point is very small and stays constant at around zero and the periodic fluctuation is hardly observed.
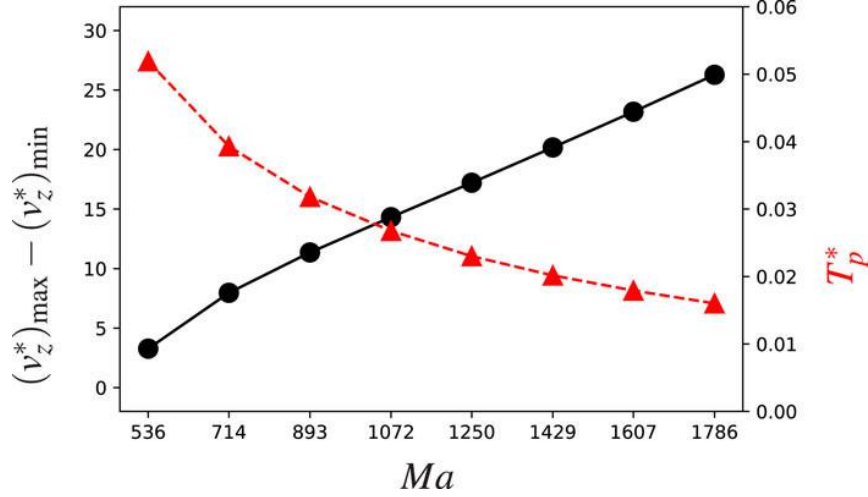
Fig. 4-12 Dependency of the flow velocity amplitude and time period at $R_\sigma = -1$ ($Ma_C = -Ma_T$) at the sampling point ($0.99a$, 0, $0.5L$): —•— (black): the velocity amplitude, $(v_z^*)_{max} - (v_z^*)_{min}$ and − − $\triangle$ − − (red): the time period, T_p^*.

4.8 The bypass transition from the regime of a 2D axisymmetric flow to a 3D chaotic flow (regime IV)

When $Ma_C \gtrsim 530$ and $R_\sigma < -1$, the flow becomes chaotic and an irregular azimuthal wave develops (regime IV in **Fig. 4-3**). This *bypass* transition develops as follows.

As $|Ma_T|$ increases, the flow reaches regime III ($R_\sigma \approx -1$) and further regime IV at $Ma_C = 1072$. The 2D axisymmetric flow develops into a periodic flow and suddenly becomes 3D chaotic with a time-dependent irregular azimuthal wave (regime IV). This is a *bypass* transition that skips the regime of 3D steady-state (regime II) due to the observed strong nonlinearity. The chaotic flow also tends to rotate slightly when $|Ma_T|$ is greater than 2800 at $Ma_C = 1072$. As $|Ma_T|$ further increases up to 3500, the rotating traveling wave overtakes, but the flow is still chaotic. The details of the rotating mode at larger $|Ma_T|$ values will be discussed in the following subsection.

The sequence of transitions from regime I to regime V is summarized in **Fig. 4-13**. The plot shows the time variation of the vertical flow velocity v_z^* at the sampling point $(0.99a, 0, 0.5L)$ at $Ma_C = 1072$. When $0 < |Ma_T| < 700$, the flow is steady state (regime I). At $-Ma_T = Ma_C = 1072$, the flow velocity fluctuates periodically around zero as explained earlier (regime III). When $|Ma_T| > Ma_C$, the flow behaves chaotic, as shown in **Fig. 4-15(a)** and **(b)**. However, as Ma_T reaches -3500, the fluctuation becomes quasi-periodic, which corresponds to the appearance of the rotating traveling wave in the concentration field in the azimuthal direction.
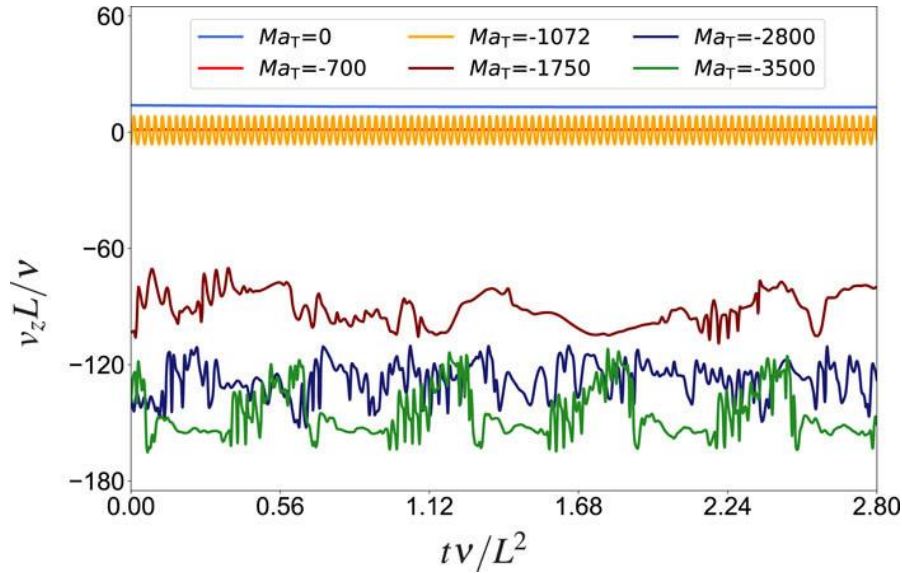
Fig. 4-13 Dependency of Ma_T on the vertical velocity, v_z^*, at the sampling point $(0.99a, 0, 0.5L)$ at $Ma_C = 1072$.

Fig. 4-14 shows the computed flow velocity vectors in the vertical r-z plane at $Ma_C = 1072$ and different values of $Ma_T = 0$, -1072, -2450, and -3500 at $t^* = 2.80$. When only solutal Marangoni convection is considered ($Ma_T = 0$), the flow along the free interface is from the bottom to the top. As Ma_T equals to -1072, there are two corner circulations near the free surface in **Fig. 4-14(b)**. The upper circulation near the top corner is driven by thermal Marangoni convection, whose direction is from the top to the bottom along the free surface, while the lower one is driven by solutal Marangoni convection. As mentioned earlier, these opposite flows approximately balance and weaken each other's strength. As Ma_T further

decreases ($Ma_C < - Ma_T$), there appears a reversed flow from the top to the bottom along the free surface, as shown in **Fig. 4-14(c)**. Once $|Ma_T|$ is sufficiently large, the total thermal and solutal Marangoni convection become stronger and the circulation extends to the central region of the liquid bridge, as shown in **Fig. 4-14(d)**.
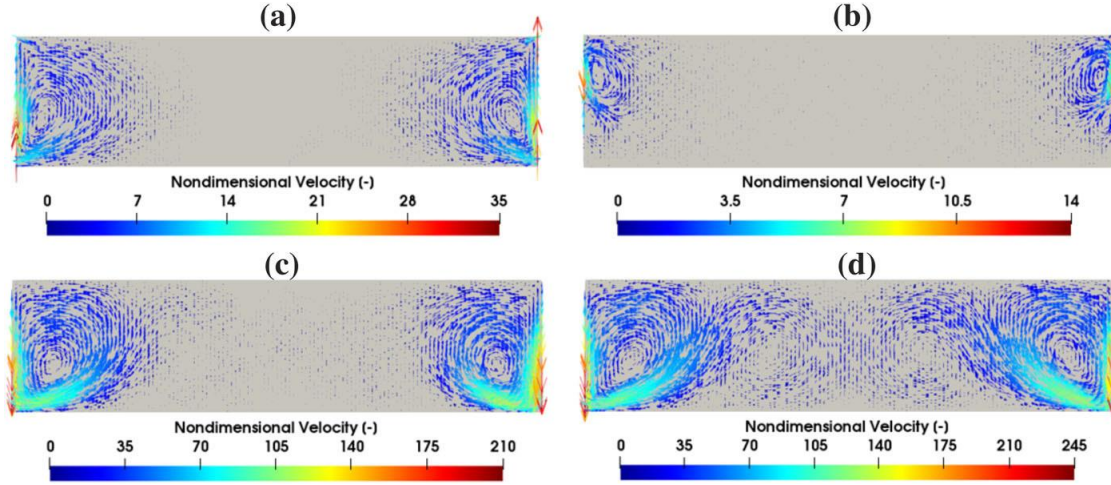
Fig. 4-14 Flow velocity vectors in the vertical r-z plane at $t^* = 2.80$ for $Ma_C = 1072$ and (a) $Ma_T = 0$ (regime I), (b) $Ma_T = -1072$ (regime III), (c) $Ma_T = -2450$ (regime IV), and (d) $Ma_T = -3500$ (regime V).

4.9 The oscillatory flow with a rotating azimuthal wave (regime V)

A transition from a chaotic flow to an oscillatory rotating flow occurs when $|Ma_T|$ is far larger than Ma_C. The chaotic concentration pattern and vertical flow velocity under $Ma_C < -Ma_T$ are shown in **Fig. 4-15**, which correspond to regime IV in **Fig. 4-3**. The non-uniform concentration distribution is strongly disturbed by the increment in $|Ma_T|$. The azimuthal wave becomes irregular, and the wave number changes in time.

As $|Ma_T|$ increases further, the flow develops into regime V, becoming an oscillatory flow with the rotating azimuthal wave. When $R_\sigma < -1$ with larger $|Ma_T|$, it is an oscillatory rotating flow with the azimuthal wave number, $m = 3$, as shown in **Fig. 4-16(a)** and **(b)**. Meanwhile, the flow velocity in the z-direction at the sampling point is quasi-periodic, as shown in **Fig. 4-16(c)**. For these cases, the rotating traveling wave emerges. As shown in **Fig. 4-17**, the non-dimensional angular flow velocity, v_θ^*, is periodic with a clear time period. The non-

dimensional time period is approximately at $T_p^* = 0.52$ at $(Ma_C, Ma_T) = (893, -3150)$ and $T_p^* = 0.84$ at $(Ma_C, Ma_T) = (1429, -3500)$, which is much longer than those of the periodic flow of regime III in **Fig. 4-12** since the oscillation mechanism is different.

Fig. 4-15 (a, b) Nondimensional concentration distribution of Si with $R_\sigma < -1$ ($Ma_C < -Ma_T$) in the r-θ plane at $z/L = 0.5$ and the vertical r-z plane with moderate $|Ma_T|$: (a) $(Ma_C, Ma_T) = (1072, -1750)$ and (b) $(Ma_C, Ma_T) = (1429, -2800)$. (c) Flow velocity in the vertical direction, v_z^*, at the sampling point $(0.99a, 0, 0.5L)$ at of regime IV.

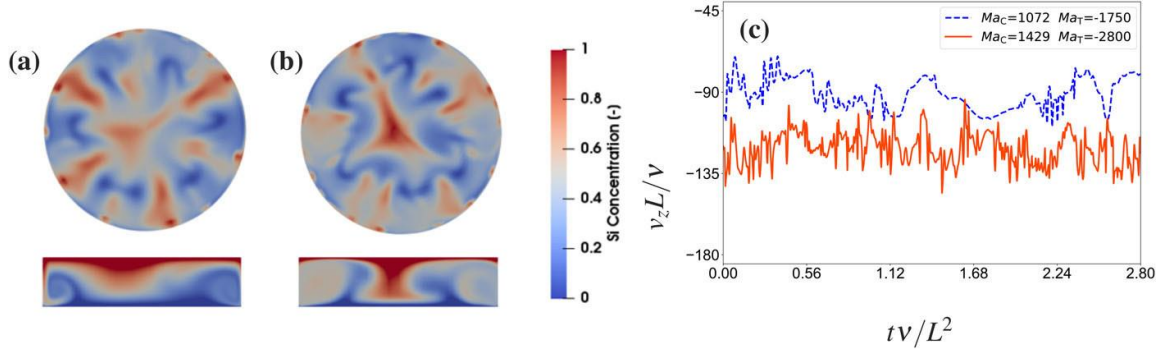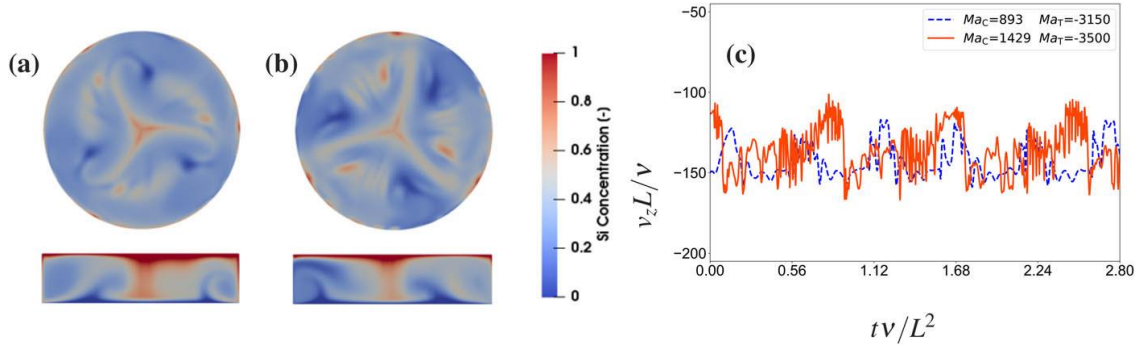**Fig. 4-16** (a, b) Nondimensional concentration distribution of Si with $R_\sigma < -1$ ($Ma_C < -Ma_T$) in the r-θ plane at $z/L = 0.5$ and the vertical r-z plane with large $|Ma_T|$: (a) $(Ma_C, Ma_T) = (893, -3150)$ and (b) $(Ma_C, Ma_T) = (1429, -3500)$. (c) Flow velocity in the vertical direction, v_z^*, at the sampling point $(0.99a, 0, 0.5L)$ at of regime V.
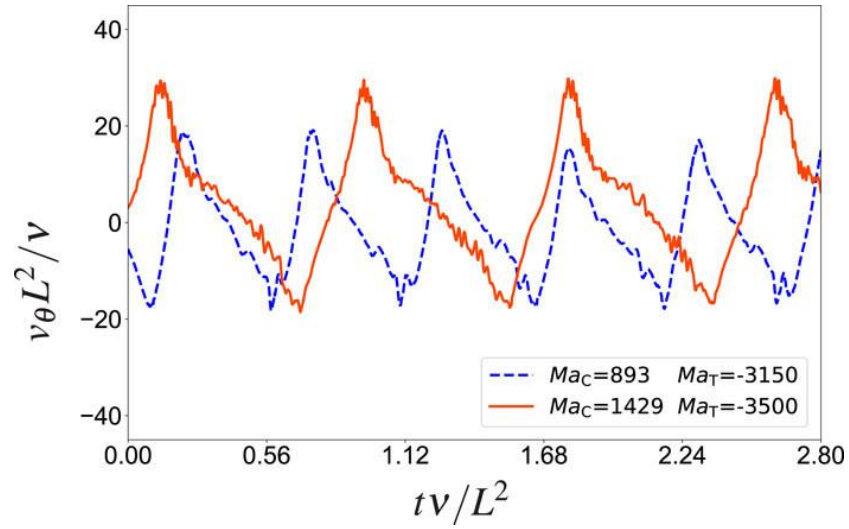
Fig. 4-17 Angular velocity, v_θ^*, in the azimuthal direction at the point of $(0.80a, 0, 0.5L)$.

4.10 Summary

By investigating the flow patterns at various combinations of (Ma_C, Ma_T) values, distinctive flow regimes of 2D axisymmetric flow, chaotic flow, oscillatory rotating flow, 3D steady flow, and even switching flow have been determined. Furthermore, two kinds of flow transitions are predicted with the increase of $|Ma_T|$ depending on the value of Ma_C. Furthermore, thermal and solutal Marangoni convection in this system can be suppressed almost completely when Ma_C is approximately equal to $-Ma_T$ ($Ma_C \approx -Ma_T$) and the flow becomes periodically stable with weak fluctuations.

Chapter V Radiation Effects on Thermal and Solutal Marangoni Convection in a Floating Half-zone

In this chapter, numerical simulation of thermal and solutal Marangoni convection in a floating half zone with radiation effects of heat loss and heat gain under zero gravity has been performed. The ambient temperature is kept constant and radiation due to heat loss and heat gain is considered as the dominant heat transfer from the ambience.

5.1 Radiation effects in a floating half zone

In an actual floating zone, there is heat transfer along the melt free surface and it needs to be taken into account. There have been some studies taking the effect of radiative heating in the form of heat loss or heat gain from the ambience. For instance, Zhang *et al.* [92] investigated the effect of radiation on thermal and solutal Marangoni convection in a shallow rectangular cavity subject to mutually perpendicular temperature and concentration gradients. It was found that the critical transition of flow destabilization depends on the strength of heat flux and the trend of critical Marangoni number varies from heat loss to heat gain. Shitomi *et al.* [93] investigated the effect of radiative heat transfer on thermocapillary convection in long liquid bridges of a high-*Pr*-number liquid under microgravity and proposed a modified heat transfer ratio to define flow patterns and observed the development of unique secondary vortices under strong heat loss and heat gain. These studies show the role of radiative heat transfer in Marangoni flows and provide an insight for further research in a floating-zone system, showing how the flow and concentration patterns are affected by radiation. Jin *et al.* [76] studied thermal and solutal Marangoni convection in a full floating-zone in which radiation was induced by the Gaussian temperature distribution along free surface. Its effects on flow patterns and flow characteristics were examined. The conclusion of this work was that radiation can affect the behavior of Marangoni flow and change its flow modes correspondingly.

As stated above, to the best of our knowledge, there are few studies examining the radiation effects on thermal and solutal Marangoni convection in a floating half zone. To

gain further insight into radiation effects or flow control with respect to heat loss and heat gain, a floating half-zone is considered in the present study. The system is simulated to predict the concentration modes at various Marangoni numbers under either heat loss or heat gain. We considered thermal and solutal Marangoni flows both in the same direction and in opposite directions in separate half zones.

5.2 Numerical methods

The numerical model of a floating half zone is shown in **Fig. 5-1**. Model assumptions, governing equations and numerical schemes are the same as those listed in *Numerical Methodology* in **Chapter II**. However, minor differences are listed below about the boundary conditions, especially the temperature field.

Due to the imposed concentration gradient along the free surface, the solutal Marangoni convection is from bottom to top. When higher temperature is set on the bottom plane, thermal Marangoni convection is also from bottom to top. This means that two flows are in the same direction. To create flows in opposite directions, higher temperature is set reversely on the top plane.

In the model, the ambient temperature (T_a) is set perpendicular to the melt free surface for the intendent radiative heat transfer to the melt. The ambient temperature is assumed to be uniform on the free surface under each heat loss or heat gain case for simplicity, ranging from 500 K to 3000 K. T_a of 500 K, 1000 K, and 1500 K represent heat loss while T_a of 2000 K, 2500 K, and 3000 K indicate heat gain. This assumption is reasonable for a half-zone model. However, more complex heating conditions have been imposed for mainly full-zone models as stated in [87]. The temperature boundary condition on the free surface follows "radiative heat transfer", as shown in Equation (10) in **Chapter II**.

Marangoni ratio (R_σ) is ranged from 0 to 1 ($0 < R_\sigma \leq 1$). When $R_\sigma = 1$, two Marangoni flows are of equivalent strengths. Ma_C is ranged from 0 to 2500, and Ma_T varies from 0 to 3500. The aspect ratio ($A_s = L/a$) of liquid bridge is 0.5. *Pr* and *Sc* number are 6.37×10^{-3} and 14.0, respectively.
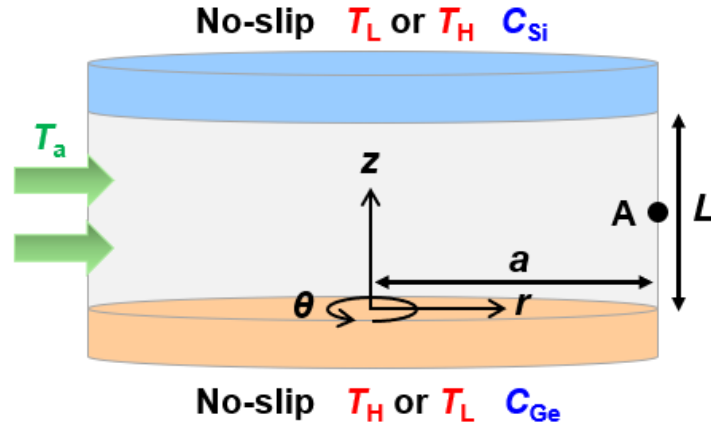
Fig. 5-1 Schematic view of the computational domain of a floating half-zone. Thermal and solutal gradients along the melt free surface determine the directions of thermal and solutal Marangoni flows.

5.3 Mesh dependency

Mesh dependency has been done to test the optimal mesh in the simulation. From **Table 5-1**, it is seen that the values of T_{ave} and U_{ave} are approximative at different mesh sizes. To save simulation time and cost and reach an accurate level, the mesh size of $40 \times 160 \times 60$ in the r, θ, and z directions, respectively, is applied in the simulation.

Table 5-1 Numerical results by different mesh sizes at $(Ma_C, Ma_T) = (2500, 2500)$ at $T_a = 2000$ K in the same-direction thermal and solutal Marangoni flow.

Mesh		T_{ave} [K]	U_{ave} [m/s]
1	$40^r \times 120^\theta \times 40^z$	1701.20	0.00556
2	$40^r \times 160^\theta \times 40^z$	1701.22	0.00557
3	$40^r \times 160^\theta \times 60^z$	1701.71	0.00554
4	$60^r \times 160^\theta \times 60^z$	1701.69	0.00540
5	$60^r \times 180^\theta \times 60^z$	1701.70	0.00543

T_{ave}: Time-averaged temperature in a fully developed state at the sampling point.

U_{ave}: Time-averaged vertical velocity in a fully developed state at the sampling point.

5.4 Radiation effects at unequal (Ma_C, Ma_T) numbers with lower R_σ values

In this section, we consider two cases of unequal Marangoni numbers: at (Ma_C, Ma_T) = (1250, 2800) with $R_\sigma = 0.45$ and at (Ma_C, Ma_T) = (500, 2500) with $R_\sigma = 0.20$ under different T_a values. From now on in the manuscript, for convenience, when the thermal and solutal Marangoni flows are in the same direction the flow will be called the "same-direction flow or convection", when the thermal and solutal flows are in opposite directions, the flow will be called the "opposite-direction flow or convection".
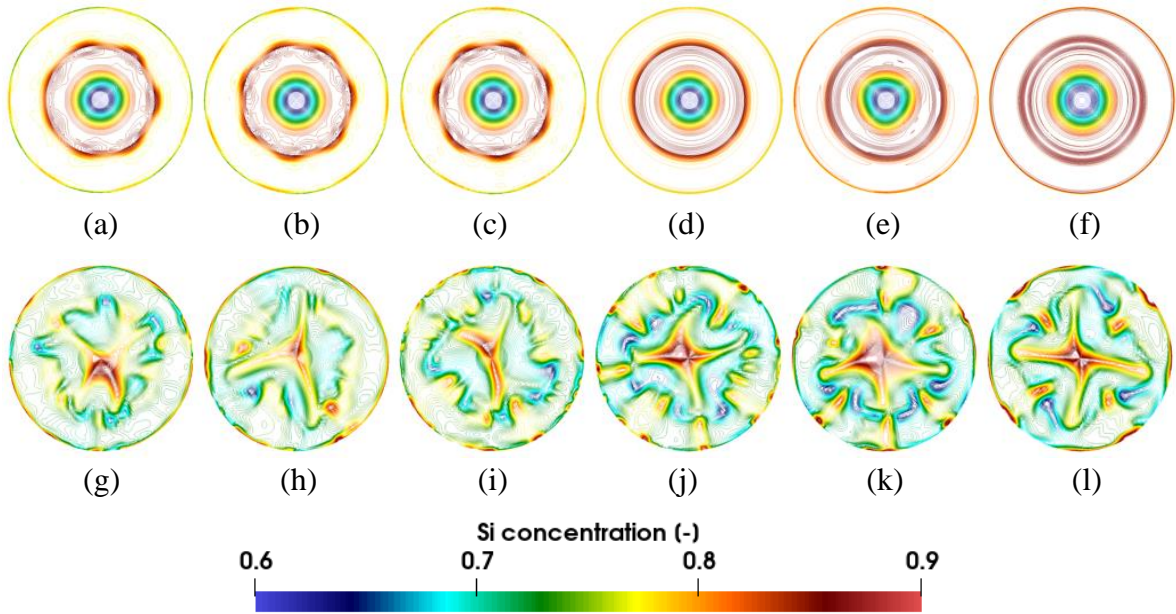
Fig. 5-2 Top view snapshots of computed Si concentration distribution at the central r-θ plane at (Ma_C, Ma_T) = (1250, 2800) with $R_\sigma = 0.45$ under different T_a, (a-f) in the same-direction flow, (g-l) in the opposite-direction flow. (a, g) $T_a = 500$ K, (b, h) $T_a = 1000$ K, (c, i) $T_a = 1500$ K, (d, j) $T_a = 2000$ K, (e, k) $T_a = 2500$ K, (f, l) $T_a = 3000$ K.

Fig. 5-2(a-f) shows the top view snapshots of computed Si concentration distribution at the central r-θ plane at (Ma_C, Ma_T) = (1250, 2800) with $R_\sigma = 0.45$ under different T_a values for the same-direction flow. Under heat loss **(a-c)**, the concentration distribution exhibits an oscillatory rotating structure with regular azimuthal wave at the wave number of $m = 7$. At a strong heat loss of $T_a = 500$ K, the wave is relatively less distinct in the azimuthal direction. In the case of heat gain, the distribution is a 2D axisymmetric structure. It appears that the

structure changes from oscillatory rotating to 2D axisymmetric ("*critical transition*") when weak heat loss is replaced by weak heat gain **(c-d)**. Similarly, **Fig. 5-2(g-l)** presents the computed concentration distributions for the opposite-direction flow. Apart from the case of a strong heat gain of $T_a = 3000$ K, the structure behaves chaotic with an irregular azimuthal wave in all cases either under heat loss or heat gain. The azimuthal wave becomes more distinct at $T_a = 2500$ K on the periphery, indicating the possibility of a critical transition at this T_a value. The concentration distribution transits to an oscillatory rotating pattern under strong heat gain as seen in **Fig. 5-2(l)**.

The variation of vertical flow velocity component for the same-direction flow is shown in **Fig. 5-3(a)** and that for the opposite-flow in **Fig. 5-3(b)**. As seen in **Fig. 5-3(a)**, under heat loss, the vertical flow velocity exhibits periodic fluctuations after $t = 500$ s, which is corresponding to the oscillatory rotating pattern. Under heat gain, the flow velocity remains almost constant with time. With the increase of T_a, the flow strength tends to decrease. As seen in **Fig. 5-3(b)**, on the other hand, the vertical flow velocity in the opposite-direction flow exhibits almost chaotic and irregular fluctuations over time. Similarly, at higher T_a values, the velocity magnitude also tends to decrease. Note that the velocity profile is more complex and shows violent fluctuations in the case of heat loss, compared to that of heat gain. This illustrates that heat loss can destabilize flow structures and lead to more complex flow modes.

(a)   (b)
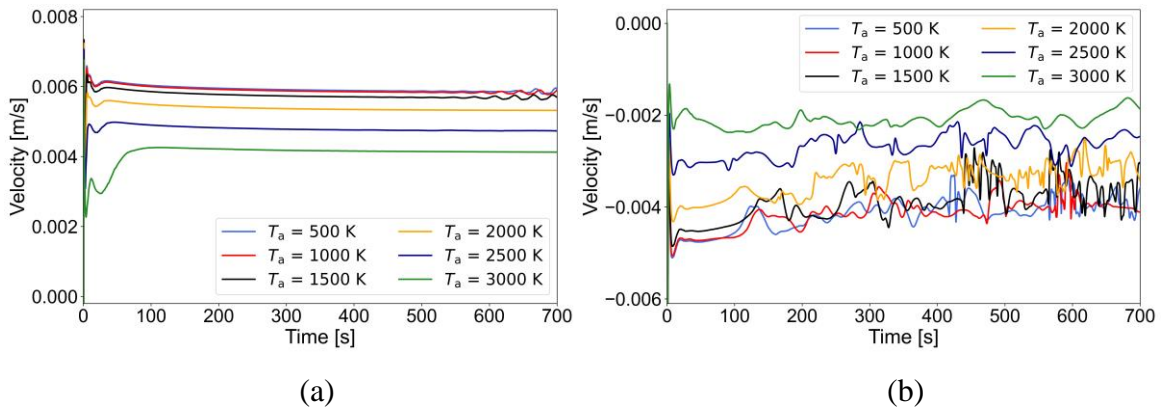
Fig. 5-3 Variation of vertical flow velocity component with time at the sampling point at (Ma_C, Ma_T) = (1250, 2800) with $R_\sigma = 0.45$, (a) in the same-direction flow, (b) in the opposite-direction flow.

Fig. 5-4(a) presents the computed surface velocity (vertical flow velocity along the free surface) distribution in the same-direction flow. The surface velocity distribution exhibits similar profile in all cases except the case of strong heat gain at $T_a = 3000$ K. At higher T_a, the maximum velocity (U_{max}) appears closer to the top plane. As T_a reaches 3000 K, there is a reverse flow near the bottom plane below the height of $z = 0.001$ m. Similarly, **Fig. 5-4(b)** shows the variations for the case of opposite-direction flow. By comparison with that of the same-direction flow, it is seen that the velocity profile is different with increased instability, and U_{max} gets closer to the bottom plane. The similarity between two flows is that there still exists a distinctly reverse flow at $T_a = 3000$ K. This observation indicates that a second vortex may form under strong heat gain in both cases. From these figures, we can also note that with the increase of T_a, the surface velocity value at the middle height ($z = 0.0025$ m) becomes smaller, which shows the same trend of the sampling point velocity given in **Fig. 5-3**. Furthermore, the smaller velocity values at higher T_a values are the indication of a critical transition to almost a constant distribution, i.e., a transition from an oscillatory rotating structure to a 2D axisymmetric structure in the same-direction flow, and a transition from chaotic to oscillatory rotating in the opposite-direction flow. These observations show that the behavior of both vertical velocities (surface and sampling point) is in accordance with those concentration distributions presented in **Fig. 5-2**.

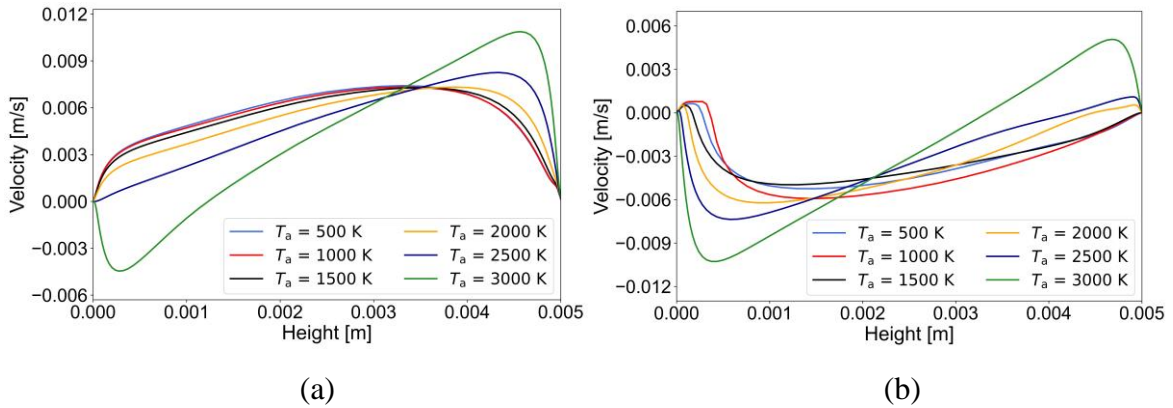(a)   (b)

Fig. 5-4 Vertical flow velocity along the free surface at $(Ma_C, Ma_T) = (1250, 2800)$ with $R_\sigma = 0.45$ at $t = 700$ s, (a) in the same-direction flow, (b) in the opposite-direction flow.

Fig. 5-5(a-c) shows the snapshots of computed Si concentration distribution at the central *r-z* plane at $(Ma_C, Ma_T) = (1250, 2800)$ with $R_\sigma = 0.45$ under heat gain. The concentration distribution is symmetric with two main vortices for the same-direction flow. However, it appears a second weak vortex developing along the free surface near the bottom plane at T_a = 3000 K. As seen from **Fig. 5-5(e, f)**, a second weak vortex also develops near the top plane at T_a = 2500 K or 3000 K in the opposite-direction flow. By comparison of two distributions, one can say that heat gain may make it easier for the development of a secondary vortex in the case of opposite-direction flow. The secondary vortex becomes larger at higher T_a values. The formation of a secondary vortex is discussed in the following section by examining the temperature distribution along the free surface.

(a)　　　　　　　　　　(b)　　　　　　　　　　(c)

(d)　　　　　　　　　　(e)　　　　　　　　　　(f)

Si concentration (-)

0.5　　　0.6　　　0.7　　　0.8　　　0.9　　　1
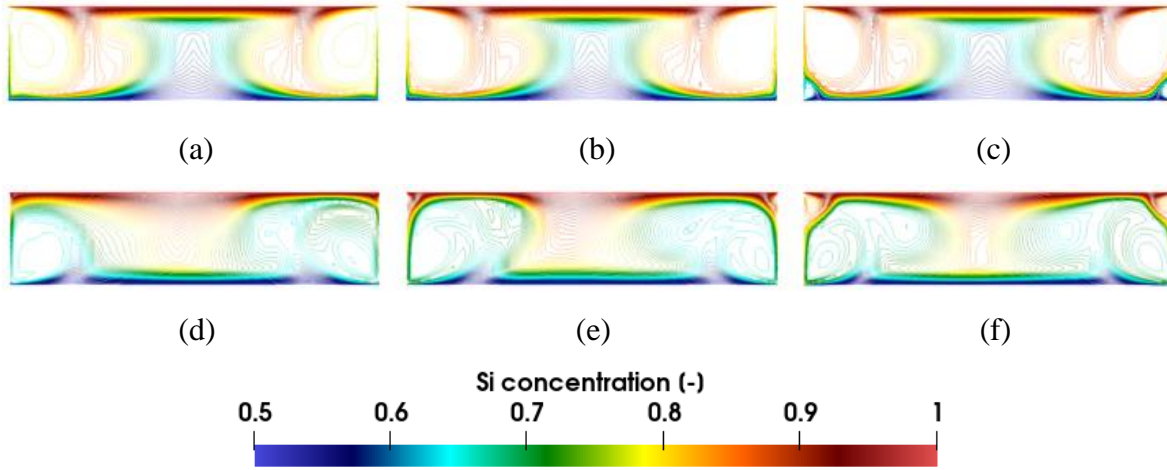
Fig. 5-5 Front view snapshots of computed Si concentration distribution at the central *r-z* plane at $(Ma_C, Ma_T) = (1250, 2800)$ with $R_\sigma = 0.45$ under heat gain, (a-c) in the same-direction flow, (d-f) in the opposite-direction flow. (a, d) T_a = 2000 K, (b, e) T_a = 2500 K, (c, f) T_a = 3000 K.

Fig. 5-6 presents temperature distribution along the free surface in the same-direction flow at $(Ma_C, Ma_T) = (1250, 2800)$ at different T_a values. As seen from this figure, at higher T_a values, the temperature distribution has non-linear profiles, with the highest temperature (T_{max}) being at the height of $z = 0.001$ m to 0.002 m. An almost linear temperature distribution at T_a = 1500 K changes to non-linear profiles with increasing temperature. Although the very fine computed temperature profile at 1500 K shows a very slight deviation from a linear

distribution, since this cannot be notable in the figure, we call it "*assumed-linear*" profile to show its evolution to non-linear profiles. The nonlinearity of temperature distribution at higher T_a values gives rise to a temperature gradient along the free surface. Since T_{max} is located slightly above the bottom plane, the thermal gradients formed in the vertical direction at higher T_a values induce secondary vortices. This is the reason we see the development of secondary vortices. Now, looking at the results presented in **Figs. 5-4, 5-5 and 5-6**, one can state that the strong heat gain at a higher T_a value may give rise to a reverse flow due to the non-linear temperature distribution along the free surface. This shows that the heat gain has a significant role in altering Marangoni flows in the melt.
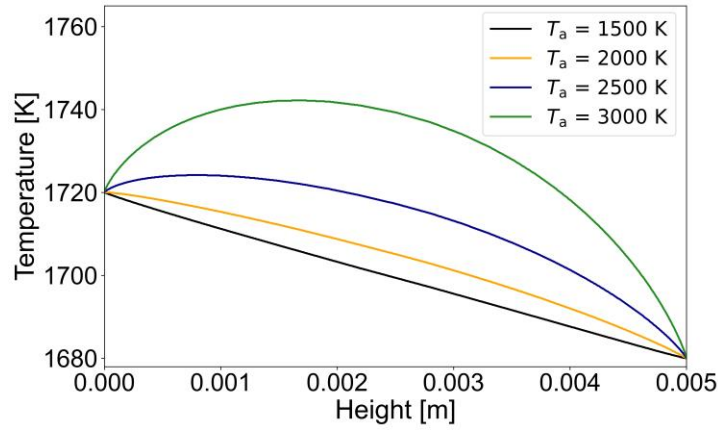
Fig. 5-6 Temperature distribution along the free surface in the same-direction flow at $(Ma_C, Ma_T) =$ (1250, 2800) at different T_a values.

Next, we discuss the effect of radiation at a lower R_σ value: $R_\sigma = 0.20$. **Fig. 5-7(a-f)** presents the top view snapshots of computed Si concentration distribution at the central r-θ plane at $(Ma_C, Ma_T) = (500, 2500)$ at different T_a values in the case of same-direction flow. In this case, the concentration distributions are of 2D axisymmetric under either heat loss or heat gain. The vertical flow velocity also remains constant as seen in **Fig. 5-8(a)**. In the case of opposite-direction flow, the distributions exhibit several critical transitions as seen in **Fig. 5-7(g-l)**, indicating the possibility of instability to some degree. Under strong heat loss or strong heat gain at $T_a = 500$ K or 3000 K, in both flows the concentration fields show oscillatory rotating patterns. They are regular with $m = 4$ under heat loss while asymmetric

with $m = 3$ under heat gain. As T_a increases from 500 K to 2000 K, it exhibits an oscillatory pattern with weak fluctuations in shape, with m varying between 4 and 5. At $T_a = 2500$ K, the structure becomes chaotic abruptly. Thus, from the snapshots in **Fig. 5-7(g-l)**, we can conclude that the concentration distribution undergoes a series of complex transitions under different heating conditions. The azimuthal wave pattern almost keeps the overall profile under heat loss while it behaves chaotic or asymmetric under heat gain. Although the structure becomes multiple in the case of opposite-direction flow at a lower R_σ values, the velocity fluctuations at the sampling point in **Fig. 5-8(b)** are not as severe as those in **Fig. 5-3(b)** because Ma_C value is much smaller than Ma_T value.
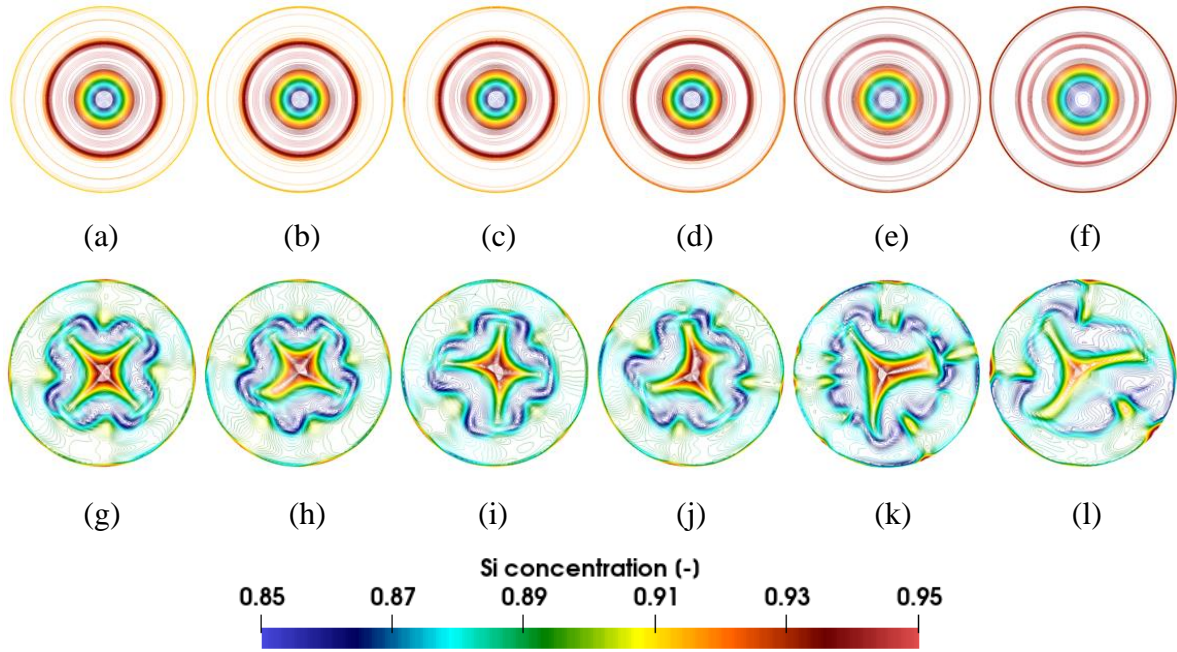

Fig. 5-7 Top view snapshots of computed Si concentration distribution at the central r-θ plane at $(Ma_C, Ma_T) = (500, 2500)$ with $R_\sigma = 0.20$ under different T_a, (a-f) in the same-direction flow, (g-l) in the opposite-direction flow. (a, g) $T_a = 500$ K, (b, h) $T_a = 1000$ K, (c, i) $T_a = 1500$ K, (d, j) $T_a = 2000$ K, (e, k) $T_a = 2500$ K, (f, l) $T_a = 3000$ K.
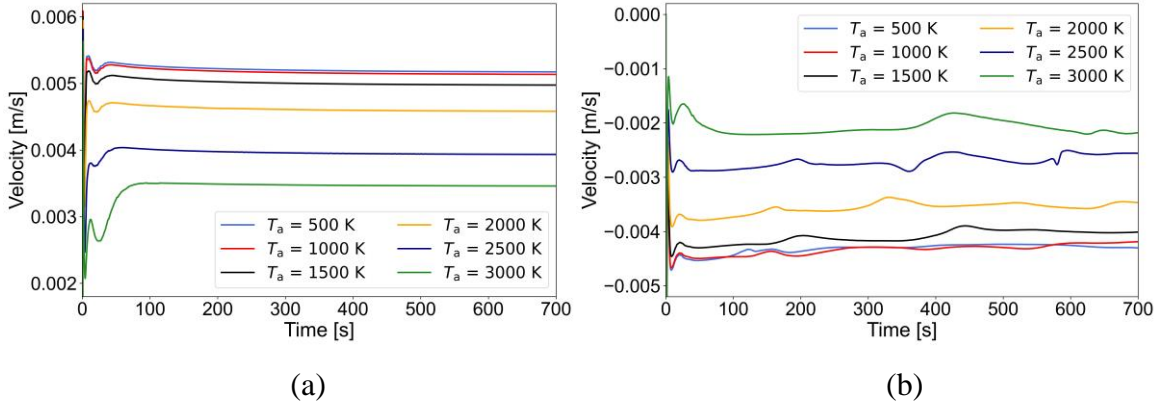
Fig. 5-8 Variation of vertical flow velocity component with time at the sampling point at (Ma_C, Ma_T) = (500, 2500) with $R_\sigma = 0.20$, (a) in the same-direction flow, (b) in the opposite-direction flow.

5.5 Radiation effects at equal (Ma_C, Ma_T) numbers with a higher R_σ value ($R_\sigma = 1$)

In this section, we consider two cases of equal Marangoni numbers: (Ma_C, Ma_T) = (750, 750) and (2500, 2500) with a higher R_σ value ($R_\sigma = 1$). To describe the radiation magnitude under different heating conditions of heat loss and heat gain, based on the "*Modified Heat Transfer Ratio*" introduced in [93], we define a new ratio in this part, the "Radiation Ratio" (φ), as

$$\varphi = \frac{Q_{LB}}{max(|Q_T|,|Q_B|)} \tag{16}$$

where Q_{LB} is the radiative heat from melt to ambience, Q_T is the heat from top plane to the melt, and Q_B is the heat from melt to the bottom plane. $\varphi > 0$ and $\varphi < 0$ represent heat loss and heat gain, respectively.

Fig. 5-9 describes the relationship between φ (radiation ratio) and T_a. Points above the dashed line represent heat loss while those below the dashed line account for heat gain. The radiation is stronger at the smaller $Ma_T = 750$. As the magnitude of heat loss or heat gain increases, the absolute value of φ increases along with them.
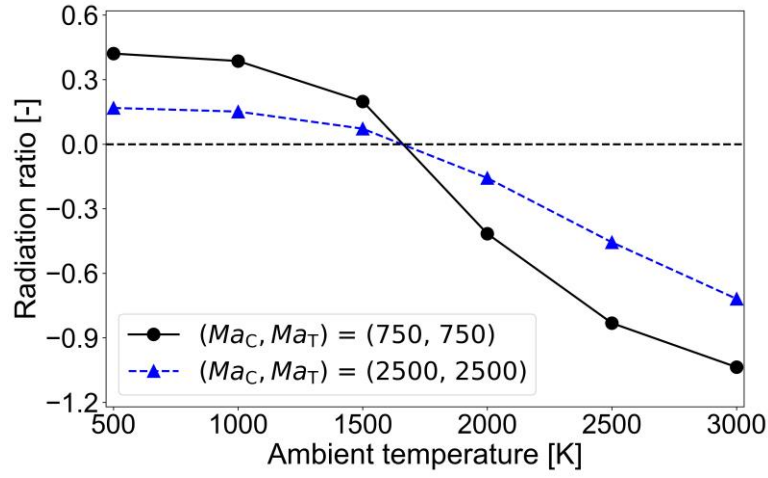
Fig. 5-9 Radiation ratio (φ) as a function of ambient temperature (T_a) at (Ma_C, Ma_T) = (750, 750) and (2500, 2500) under various heating conditions.
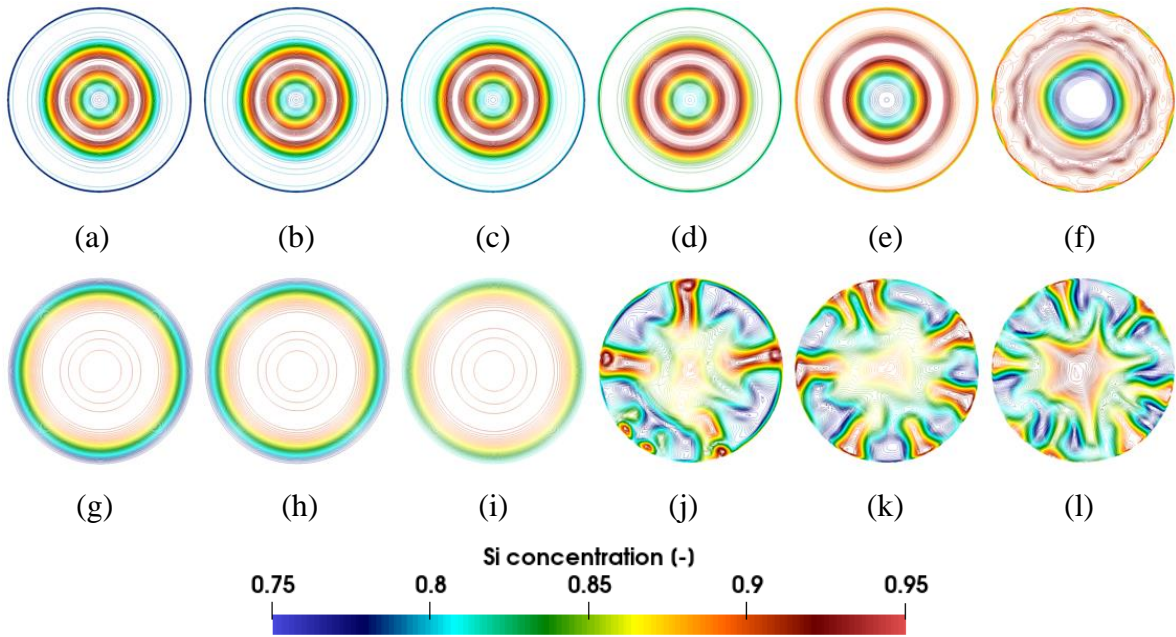
Fig. 5-10 Top view snapshots of computed Si concentration distribution at the central r-θ plane at (Ma_C, Ma_T) = (750, 750) with $R_\sigma = 1$ under different T_a, (a-f) in the same-direction flow, (g-l) in the opposite-direction flow. (a, g) T_a = 500 K, (b, h) T_a = 1000 K, (c, i) T_a = 1500 K, (d, j) T_a = 2000 K, (e, k) T_a = 2500 K, (f, l) T_a = 3000 K.

Fig. 5-10(a-f) shows the top view snapshots of computed Si concentration distribution at the central r-θ plane at $(Ma_C, Ma_T) = (750, 750)$ with $R_\sigma = 1$ under different T_a in the same-direction flow. The concentration field exhibits a 2D axisymmetric structure under heat loss and medium heat gain up to $T_a = 2500$ K. However, there is a critical transition to an oscillatory rotating pattern with $m = 13$ under strong heat gain at $T_a = 3000$ K. It is observed that the concentration distribution inside the melt tends to remain asymmetric, which oscillates with time.

(a)   (b)

Fig. 5-11 (a) Variation of vertical flow velocity component with time at the sampling point at $(Ma_C, Ma_T) = (750, 750)$ with $R_\sigma = 1$ in the same-direction flow. (b) Si concentration distributions in the radial direction at the height $z = 0.0025$ m.

Fig. 5-11(a) gives an insight to this phenomenon in the flow velocity field. For instance, constant velocity accounts for the axisymmetric structure, and the profile with periodic fluctuations accounts for the oscillatory rotating pattern at $T_a = 3000$ K. Although most of the structures are axisymmetric in **Fig. 5-10(a-f)**, it is difficult to determine the concentration distribution or uniformity in the radial direction. **Fig. 5-11(b)** presents the computed Si concentration distributions in the radial direction at the height of $z = 0.0025$ m, with almost similar profile forms at each T_a value. To make the differences more notable, the coefficient of variance (CV) is introduced. This coefficient is defined as $CV = \sigma_{Si}/\bar{C}_{Si}$ with the ratio of standard deviation to the mean of Si concentration. We calculated CV as 4.60%, 4.55%, 4.41%, 4.11%, 5.10%, and 7.13% at $T_a = 500$ K, 1000 K, 1500 K, 2000 K, 2500 K, and 3000

K, respectively. As seen CV has a minimum value at T_a = 2000 K. This implies that a weak heat gain may lead to a comparatively better concentration uniformity.

The computed Si concentration distributions shown in **Fig. 5-10(g-l)** in the case of the opposite-direction flow exhibit 2D axisymmetric structures under heat loss. Considering this together with the results given in **Fig. 5-12(a)**, we can state that the flow strength at the sampling point is very weak, which means thermal and solutal Marangoni flows nearly offset each other since we used the same Ma_C and Ma_T values. Under heat gain, however, the stability of symmetry is destroyed with the chaotic behavior (large fluctuations) of the fluid flow. We note that the velocity profile fluctuations appear in a *two-stage* variation, with a huge increase at T_a = 2000 K in the first stage, and then the velocity decreases around zero with time-dependent irregular fluctuations in the second stage as T_a further increases to 2500 K or 3000 K. This *two-stage* phenomenon is also observed if the sampling point moves in the azimuthal direction at the same height with similar flow fluctuations in the velocity field.

From **Fig. 5-12(b)**, we see that the velocity along the free surface under heat loss is very weak, while a reverse flow is observed under heat gain. Comparing these with the results in **Fig. 5-4(b)**, we note that the magnitude of reverse flow is larger at $R_\sigma = 1$. At the midpoint, the velocity is approximately zero for all heating cases. $U_{\max}$ near the bottom plane is approximately twice of that near the top plane under heat gain.

(a)   (b)
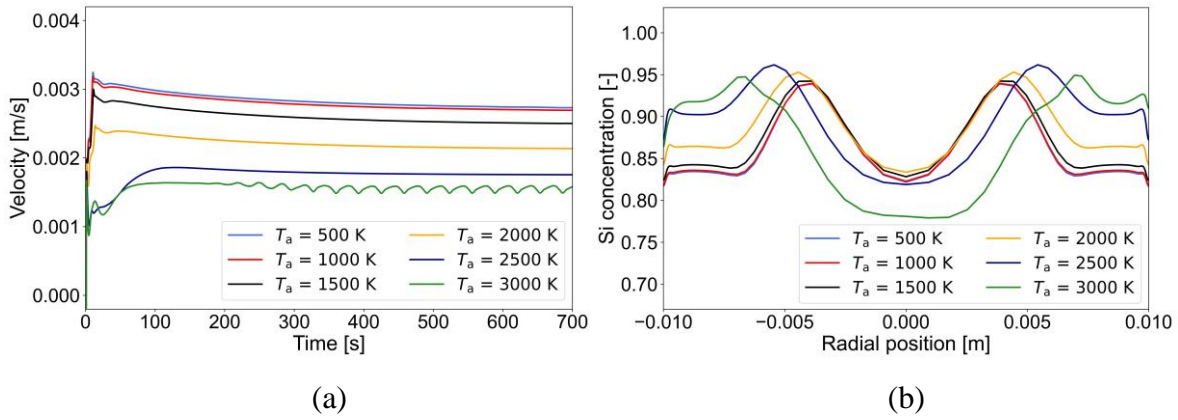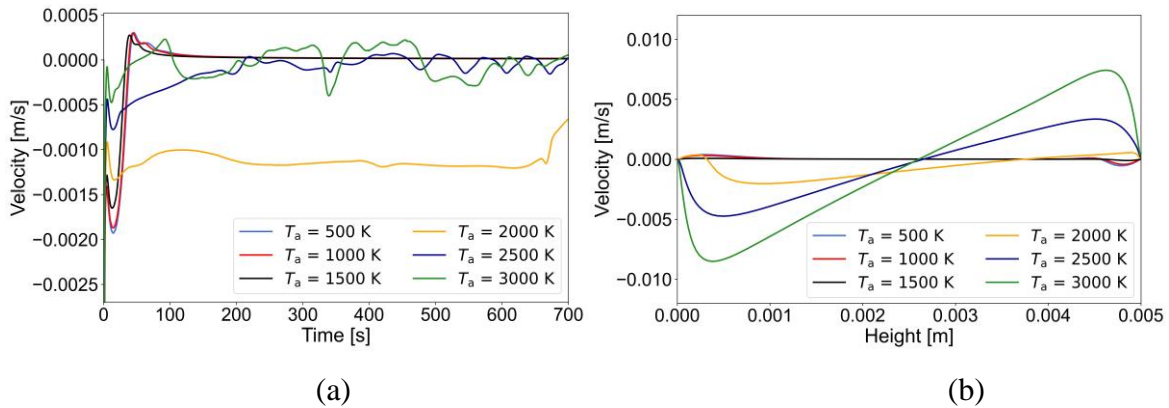
Fig. 5-12 (a) Variation of vertical flow velocity component with time at the sampling point at (Ma_C, Ma_T) = (750, 750) with $R_\sigma = 1$ in the opposite-direction flow. (b) Vertical flow velocity along the free surface at t = 700 s in the opposite-direction flow.

Si concentration (-)

0.7 0.8 0.9 1

Fig. 5-13 Snapshots of computed Si concentration distribution at the central r-z plane at (Ma_C, Ma_T) = (750, 750) with $R_\sigma = 1$ under heat gain in the opposite-direction flow, (a-c) front view, (d-f) side view. (a, d) $T_a = 2000$ K, (b, e) $T_a = 2500$ K, (c, f) $T_a = 3000$ K.

Si concentration (-)

0.7 0.8 0.9 1

Fig. 5-14 Computed concentration distribution along the exterior free surface under different heating conditions in the opposite-direction flow. (a) $T_a = 1000$ K, (b) $T_a = 2000$ K, (c) $T_a = 3000$ K.

    Fig. 5-13 shows the snapshots of computed Si concentration distribution at the central r-z plane at (Ma_C, Ma_T) = (750, 750) with $R_\sigma = 1$ under heat gain in the opposite-direction flow. At $T_a = 2000$ K, there is a chaotic distribution with a tendency of vortex formation along the free surface. At higher T_a values, the distribution becomes asymmetric with four vortices of almost equal size, which is different from the one observed in **Fig. 5-5**. As explained earlier, the additional vortices developed are induced by the maximum temperature at the midpoint on the free surface under a strong heat gain. **Fig. 5-14** presents the

concentration distribution along the exterior free surface under different heating conditions in the opposite-direction flow. In the case of heat loss at $T_a = 1000$ K, the isolines are parallel to each other with an axisymmetric steady structure. This steady-state structure becomes chaotic as heat loss changes to heat gain, with significant instabilities.
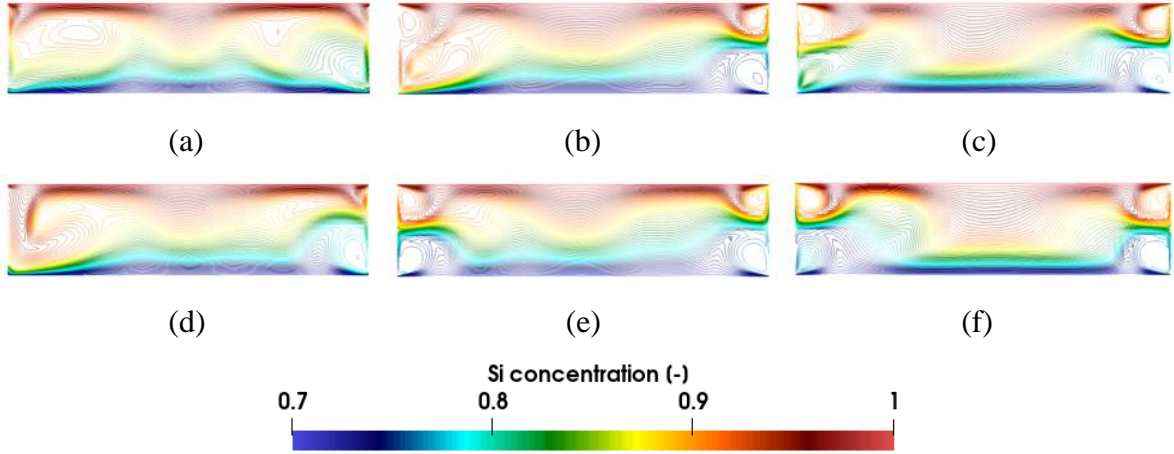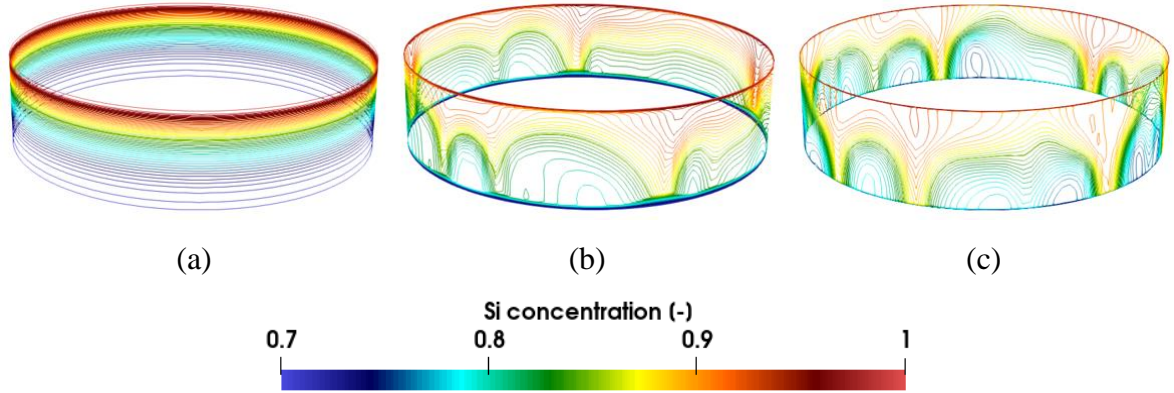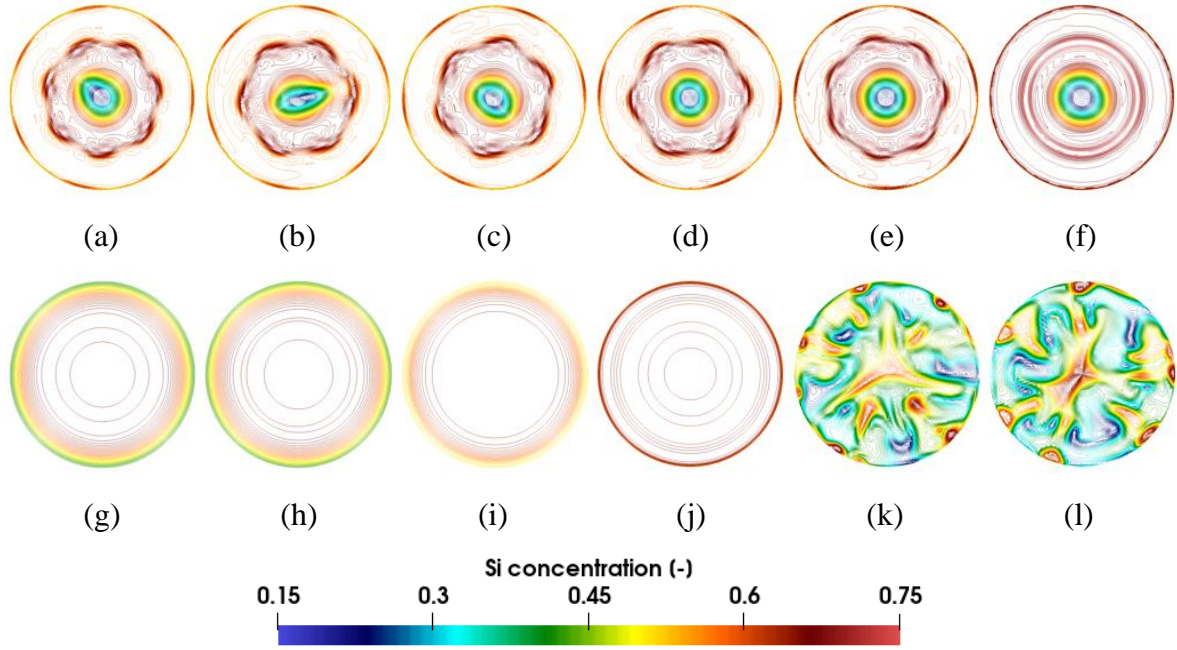

Fig. 5-15 Top view snapshots of computed Si concentration distribution at the central r-θ plane at $(Ma_C, Ma_T) = (2500, 2500)$ with $R_\sigma = 1$ under different T_a, (a-f) in the same-direction flow, (g-l) in the opposite-direction flow. (a, g) $T_a = 500$ K, (b, h) $T_a = 1000$ K, (c, i) $T_a = 1500$ K, (d, j) $T_a = 2000$ K, (e, k) $T_a = 2500$ K, (f, l) $T_a = 3000$ K.

Fig. 5-15(a-f) shows the top view snapshots of computed Si concentration distribution at the central r-θ plane at $(Ma_C, Ma_T) = (2500, 2500)$ with $R_\sigma = 1$ under different T_a values in the same-direction flow. Under heat loss, the peripheral wave pattern behaves oscillatory rotating with m varying from 6 to 7 in the azimuthal direction. The internal pattern also presents an asymmetric structure with $m' = 2$. Similarly, under heat gain, the transition from an oscillatory rotating pattern to a 2D axisymmetric structure takes place at T_a values higher than 2500 K. Note that the interior wave pattern regains its axisymmetric structure with $m' = 0$ in the case of heat gain. Compared with those structures at the lower $(Ma_C, Ma_T) = (750,$

750) in **Fig. 5-10(a-f)**, it is concluded that the transition is totally reversed at the higher (Ma_C, Ma_T) values when $R_\sigma = 1$, i.e., from an oscillatory rotating pattern to an axisymmetric steady one.

As seen in **Fig. 5-16(a)**, the vertical velocity in all cases at the sampling point exhibit periodic fluctuations with time, which are in agreement with the corresponding oscillatory rotating patterns. However, the fluctuation amplitude becomes weaker and more frequent under strong heat gain at $T_a = 3000$ K. Although the concentration field is 2D axisymmetric, the corresponding flow velocity still exhibits small oscillations at this temperature. This implies that the flow is in a quasi-critical state, and at higher T_a values, the velocity profile would be constant corresponding to a pure axisymmetric structure in the concentration field. **Fig. 5-16(b)** provides further insight to the characteristics of vertical velocity at different T_a values in the same-direction flow. The degree of reduction in U_{max} under heat gain is far larger than that of under heat loss. In the frequency profile, f increases significantly at values from 2500 K to 3000 K, coinciding with the structure conversion described earlier. This shows the velocity fluctuation frequency can be a tool to identify the critical transition.

(a)   (b)

Fig. 5-16 (a) Variation of vertical flow velocity component with time at the sampling point at (Ma_C, Ma_T) = (2500, 2500) with $R_\sigma = 1$ in the same-direction flow. (b) Frequency (f) and maximum velocity (U_{max}) as a function of ambient temperature (T_a).

Fig. 5-15(g-l) describes the opposite-direction flow at (Ma_C, Ma_T) = (2500, 2500) with $R_\sigma = 1$. Similar to those observed in **Fig. 5-10(g-l)**, in this case the concentration field

experiences a transition from an axisymmetric structure to a chaotic one. The strong heat gain has a significant effect on the mode by altering the temperature distribution. Contrary to the weak flow observed at a smaller (Ma_C, Ma_T) value, the vertical velocity at a larger (Ma_C, Ma_T) value in **Fig. 5-17(a)** exhibits regularly periodic fluctuations around zero under heat loss and weak heat gain at $T_a = 2000$ K. At higher T_a values, the flow becomes a *one-stage* chaotic fluctuation with a higher magnitude. The second stage of chaotic transition observed in **Fig. 5-12(a)** does not appear in this case. It may be speculated that, at further higher T_a values, i.e., $T_a > 3000$ K, it may be probable to see the second stage of chaotic transition. The periodic vertical velocity variations shown in **Fig. 5-17(a)** are enlarged in **Fig. 5-17(b)** to observe the scale of magnitudes more clearly. As seen, at higher T_a values under heat loss, the amplitudes tend to become larger. Based on these results, the weak periodic structure is adopted to distinguish various concentration distributions.

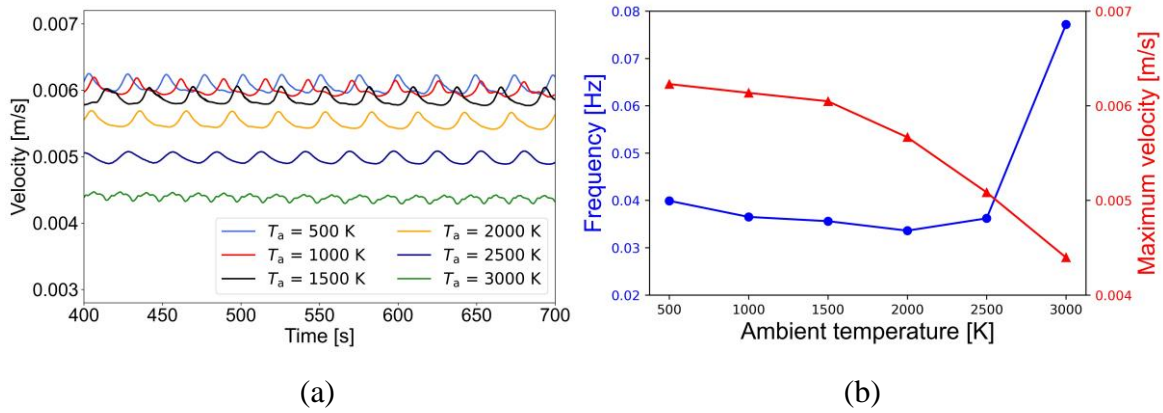(a)   (b)
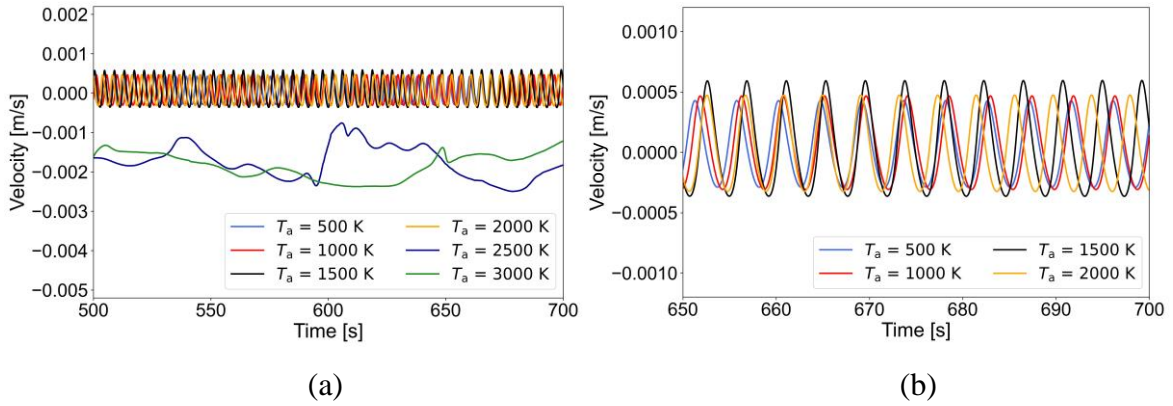
Fig. 5-17 (a) Variation of vertical flow velocity component with time at the sampling point at (Ma_C, Ma_T) = (2500, 2500) with $R_\sigma = 1$ in the opposite-direction flow. (b) Velocity shows periodic fluctuations from $t = 650$ s to 700 s.

5.6 Transition mode map under heat loss and heat gain

Fig. 5-18 summarizes the structures of concentration distributions and their transitions, with the assumption of $Ma_C \leq Ma_T$ in the same-direction flow, with respect to ambient temperature (T_a) and Marangoni ratio (R_σ). As seen, there are 2D axisymmetric, 3D steady, and oscillatory rotating structures in this map. At a lower R_σ value, the mode is almost 2D

axisymmetric no matter how low or high T_a value is. At a medium or higher R_σ value, the mode changes from an oscillatory rotating pattern to a 2D axisymmetric one under heat gain. In some cases, there occurs a second reverse transition from a 2D axisymmetric structure to an oscillatory rotating one. With respect to heat loss or heat gain, it is observed that the concentration field tends to lose its stability with a non-symmetric pattern under strong heat loss at a higher R_σ value. Even the internal structure becomes non-symmetric, as described in **Fig. 5-15**. Under heat gain, the mode prone to experience a critical transition and a second vortex may form along the free surface at very high T_a values. This indicates that heat gain may have a stabilizing effect on the Marangoni flows.
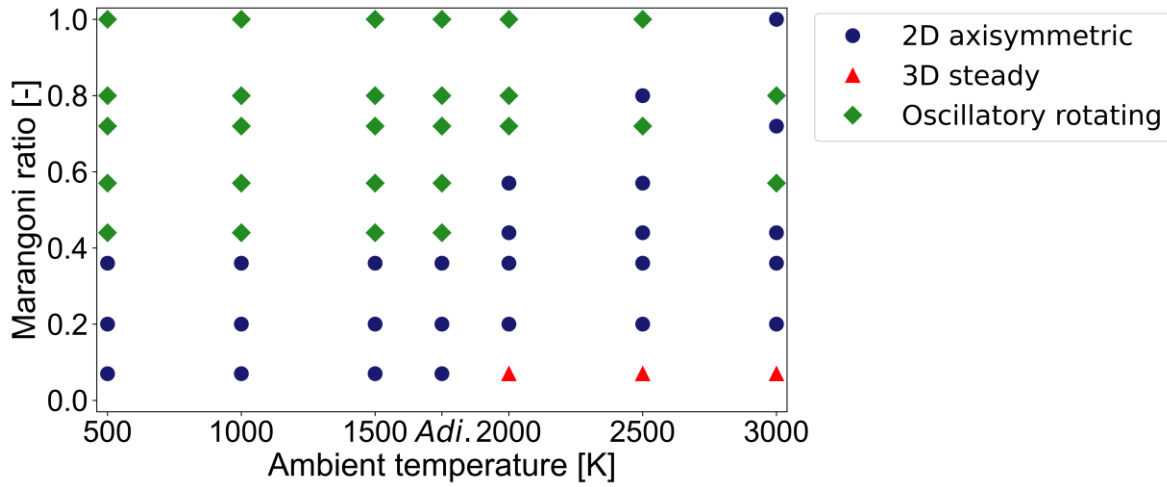
Fig. 5-18 Transition mode map based on concentration distribution with respect to Marangoni ratio (R_σ) and ambient temperature (T_a) in the same-direction flow. Ambient temperature of 500 K, 1000 K, and 1500 K refer to heat loss and 2000 K, 2500 K, and 3000 K refer to heat gain. *Adi.* refers to the adiabatic condition. Plots at $R_\sigma = 1$ are determined by (Ma_C, Ma_T) = (2500, 2500).

Although we observe an oscillatory rotating pattern either under heat loss or heat gain in the concentration field, the behaviors of two cases are quite different, as shown in **Fig. 5-19(a-d)**. The wave pattern is regular under heat loss with $m = 5$ and the rotating mode is dominant with weak oscillations. We call this *oscillatory Mode I*. However, under heat gain, the oscillatory rotating mode becomes more complex, with explicit oscillations as well as

with a non-symmetric interior pattern. We call it *oscillatory Mode II*. The wave number also shows a fluctuating behavior due to the strong oscillation effects.

(a) (b) (c) (d)

(e)
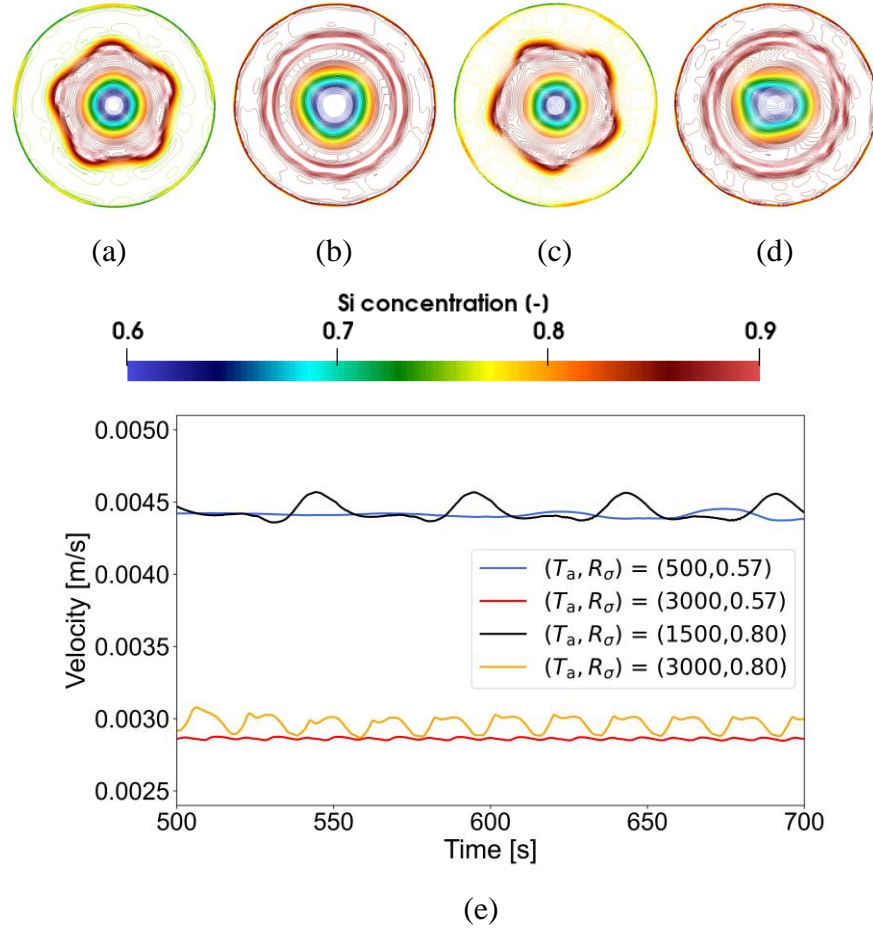
Fig. 5-19 Top view snapshots of computed Si concentration distribution at the central r-θ plane at various combinations of (T_a, R_σ) from oscillatory rotating pattern, (a) (T_a, R_σ) = (500, 0.57), (b) (T_a, R_σ) = (3000, 0.57), (c) (T_a, R_σ) = (1500, 0.80), (d) (T_a, R_σ) = (3000, 0.80). (e) Vertical flow velocity with time at the sampling point in the same-direction flow.

Furthermore, given that the formation of this oscillation after the 2D axisymmetric structure in the map, it can be concluded that the *oscillatory Mode II* is developed by transition from the 2D axisymmetric structure at higher T_a values, representing enhanced rotating oscillations under strong heat gain. To the contrary, *oscillatory Mode I* is in a relatively stable state. **Fig. 5-19(e)** further demonstrates the features of these two oscillatory

modes. The fluctuations of Mode II are more complex, with higher frequencies. At (T_a, R_σ) = (3000, 0.57), the vertical velocity exhibits much higher fluctuation frequencies compared to those at a lower T_a value. Besides, a jagged-shaped fluctuation appears at (T_a, R_σ) = (3000, 0.80), which exacerbates the flow instability by the strong heat gain. For these two oscillatory rotating modes, the angular frequency (f_θ) is calculated. Under heat loss, f_θ takes values of 0.021 Hz and 0.042 Hz at (T_a, R_σ) = (500, 0.57) and (1500, 0.80), respectively. Under heat gain, f_θ is 0.064 Hz and 0.066 Hz at (T_a, R_σ) = (3000, 0.57) and (3000, 0.80), respectively. Similarly, the angular frequency value under heat gain is higher than that of heat loss. This explains the complex and irregular behavior of Mode II under heat gain. Overall, the two oscillatory rotating modes correspond to totally different flow states. Thus, this makes necessary the need for a future investigation of *oscillatory Mode II* to gain more insight into the flow mechanism.

Fig. 5-20 summarizes the structures of concentration distributions and their transitions, with the assumption of $Ma_C \leq Ma_T$ in the opposite-direction flow, described in the same way. There are 3D steady, oscillatory, oscillatory rotating, chaotic, and weak periodic structures (with velocity-field features) in this map. The presence of various structures means that the opposite-direction flow becomes multiple, especially at a lower or higher R_σ value. At a higher R_σ value, the transition tends to move from a weak periodic structure to a chaotic one with the increase of T_a. At a lower R_σ value, the concentration distribution exhibits a 3D steady structure under heat loss, while oscillatory one under heat gain. Meanwhile, it behaves quite irregular at $R_\sigma = 0.20$, exhibiting multiple structures by changes in the heating conditions. The concentration pattern is hardly affected at a medium R_σ value in this transition mode map with a consistent chaotic feature. Considering the above results given in the case of the opposite-direction flow, one can state that the azimuthal wave becomes distinct and even rotating as in the mode of oscillatory rotating pattern under strong heat gain.
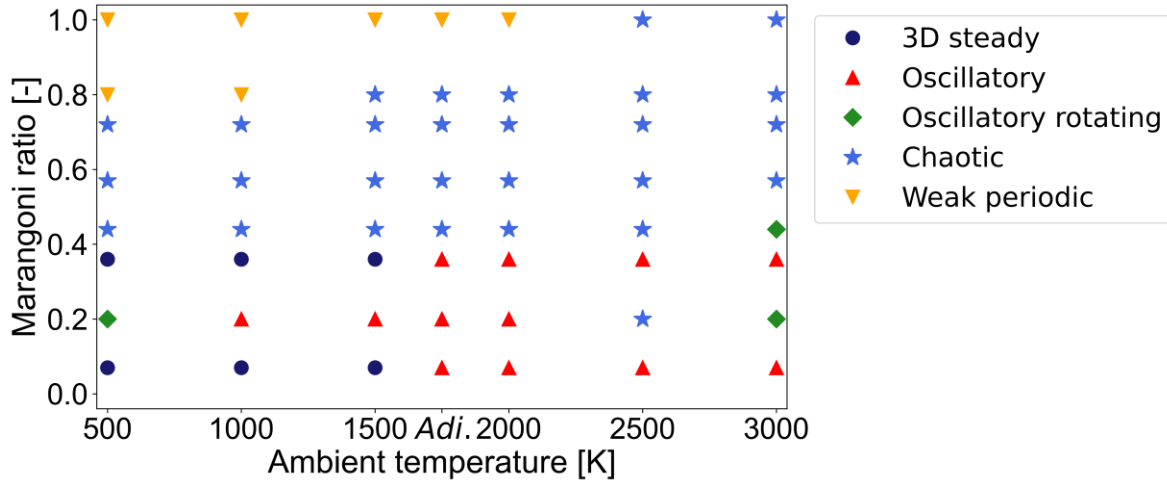
Fig. 5-20 Transition mode map based on the concentration distribution with respect to Marangoni ratio (R_σ) and ambient temperature (T_a) in the opposite-direction flow. Ambient temperature of 500 K, 1000 K, and 1500 K refer to heat loss and 2000 K, 2500 K, and 3000 K refer to heat gain. *Adi.* refers to the adiabatic condition. Plots at $R_\sigma = 1$ are determined by (Ma_C, Ma_T) = (2500, 2500).

In **Fig. 5-20**, it is concluded that there exists a critical transition from a chaotic structure to weak periodic one at a higher R_σ value with the decrease of T_a. **Fig. 5-21** describes this transition with some snapshots of Si concentration distributions at $R_\sigma = 0.80$. The flow is stabilized with weak oscillations in the azimuthal direction from the chaotic structure, which is resulted from the fact that the Ma_C and Ma_T values are getting closer to each other, offsetting each other's effect significantly. Although the stabilizing phenomenon is simultaneously observed in **Fig. 5-7(g-i)**, the transition was due to the small Ma_C value. This indicates the concentration field is overall in a relatively steady state.

Compared with **Fig. 5-18**, the transition mode in the opposite-direction flow is much more complex with multi-directional conversions, and two sorts of *stabilizing effects* under heat loss are observed. However, as mentioned above, at a lower R_σ value, the transition mode appearing in an irregular manner may be function of the values of Ma_C and Ma_T numbers. Although R_σ is constant at 0.20, different combinations of (Ma_C, Ma_T) may contribute to it, as long as we keep the ratio as $Ma_C/Ma_T = 0.20$. Therefore, it feels that a further investigation is needed on this issue, especially focusing on lower R_σ values.
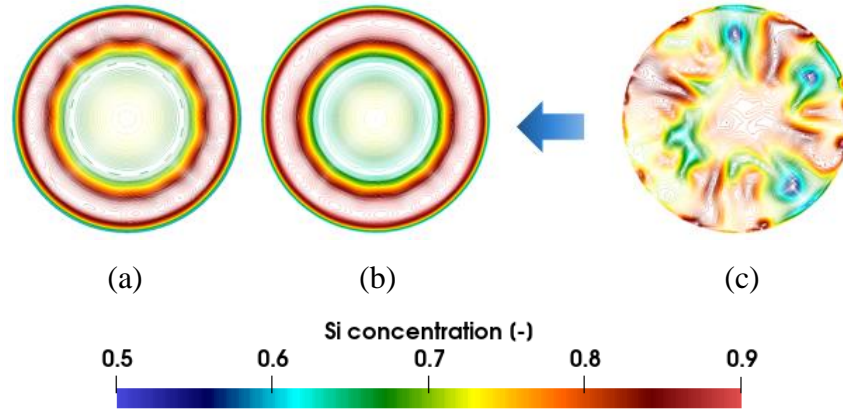
Fig. 5-21 Stabilizing effect on Si concentration distribution at $(Ma_C, Ma_T) = (1400, 1750)$ with $R_\sigma = 0.80$ under heat loss in the opposite-direction flow at (a) 500 K, (b) 1000 K, and (c) 1500 K.

5.7 Summary

Transition mode maps, based on concentration distribution with respect to Marangoni ratio (R_σ) and ambient temperature (T_a) have been developed to investigate the radiation effects at unequal or equal (Ma_C, Ma_T) values. Furthermore, two sorts of oscillatory modes are observed in the same-direction Marangoni flows under either heat loss or heat gain. While two kinds of stabilizing effects are predicted under heat loss in the opposite-direction Marangoni flows.

Chapter VI Conclusions and Future Perspectives

The conclusions of each Chapter (**Chapter III**, **IV**, and **V**) are presented in the following subsections. The future perspectives are listed in the end of this chapter.

6.1 Thermal and solutal Marangoni convection in a full floating zone

A numerical simulation study of thermal and solutal Marangoni convection in a full floating zone under zero gravity has been conducted, and cases of $Ma_C = 1072$ and 1786 and $Ma_T = 700$, 1400, 2100, and 2800 are investigated.

- The computed temperature field exhibits a Gaussian thermal profile and generates the thermal Marangoni convection in the zone.
- At smaller Ma_T values, the combined thermal and solutal flow patterns are suppressed to two vortices, that are mainly located in the upper half zone. At higher Ma_T values, the flow becomes enhanced, and four vortices develop along the free surface.
- The characteristics of the concentration pattern in the zone vary due to the varying thermal and solutal Marangoni numbers, as well as the characteristic azimuthal wave.

This section gives an overall insight into thermal and solutal Marangoni convection in a full floating zone, which approximates the actual process of crystal growth by FZ method. The results indicate that the flow pattern varies due to the region selected, with the consideration of thermal and solutal Marangoni convection in the same or opposite directions.

6.2 Characterization of thermal and solutal Marangoni convection of opposite directions in a half floating zone

A numerical simulation study of the thermal and solutal Marangoni convection of opposite directions developing in a half floating zone has been performed under the assumption of zero gravity and adiabatic free surface.

- The flows develop into various regimes depending on the values of Ma_C and Ma_T: Regime I develops for $-1 < R_\sigma < 0$ ($Ma_C > -Ma_T$) in which the flow is 2D

axisymmetric steady; regime II for $R_\sigma < -1$ ($Ma_C < -Ma_T$) at $Ma_C \lesssim 360$, where the flow becomes 3D steady with an m-folded symmetry in the azimuthal direction; regime III for $R_\sigma \approx -1$ ($Ma_C \approx -Ma_T$) with the flow fluctuating periodically with a very weak amplitude; regime IV for $R_\sigma < -1$ ($Ma_C < -Ma_T$) at $Ma_C \gtrsim 530$ with moderate $|Ma_T|$ in which the flow is 3D chaotic; and regime V with large $|Ma_T|$, where the flow becomes quasi-periodic oscillatory rotating with the time-dependent azimuthal wave number between $m = 3$ and 4.

- The predicted flow transition mechanism depends on Ma_C. When Ma_C is small ($Ma_C \lesssim 360$), the transition occurs and the 2D axisymmetric flow of regime I becomes 3D steady in regime II as $|Ma_T|$ increases. When Ma_C is large ($Ma_C \gtrsim 530$), the flow exhibits two critical transitions as $|Ma_T|$ increases. The first transition is from the 2D axisymmetric flow (regime I) to the 3D chaotic flow (regime IV), and the second one is from the chaotic flow to the oscillatory rotating flow (regime V).

- The strength of combined thermal and solutal Marangoni convection can be suppressed almost completely when $-Ma_T$ is approximately equal to Ma_C due to the opposing effects of thermal and solutal Marangoni flows developing in the liquid bridge of the FZ growth of SiGe.

This chapter focuses on the lower-half zone with the assumption that thermal and solutal Marangoni convection are in the opposite direction. Compared to the flow in the same direction, characteristic and unique flow regimes of chaotic flow and 3D steady flow are newly determined. Flow transitions are predicted depending on value of Ma_C.

6.3 Radiation effects on thermal and solutal Marangoni convection in a floating half-zone

A numerical simulation study of thermal and solutal Marangoni convection in a floating half zone with radiation effects under zero gravity has been conducted. Transition mode maps based on the concentration distribution are developed for the same-direction and opposite-direction flows with the assumption of $Ma_C \leq Ma_T$.

- In the same-direction Marangoni flows, the transition tends to occur at a medium or higher R_σ value under the condition of heat gain from an oscillatory rotating pattern to a 2D axisymmetric structure, which improves the flow stability. The concentration distribution behaves oscillatory rotating again under the strong heat gain in some cases, the rotating mode however behaves quite differently.

- In the opposite-direction Marangoni flows, the transition mainly occurs at a lower or higher R_σ value with the increase of T_a from heat loss to heat gain. At a lower R_σ value, the transition mode becomes more complex and irregular. At a lower or higher R_σ value, strong heat loss can stabilize the concentration field by changing the mode into a relatively steady state.

- In the same-direction Marangoni flows with $R_\sigma = 1$ at lower Ma ($Ma = Ma_C = Ma_T$) values, there is a critical transition from a 2D axisymmetric structure to an oscillatory rotating pattern with the increase of T_a. While, at higher Ma values, it behaves reversely from an oscillatory rotating pattern to a 2D axisymmetric structure with the increase of T_a.

- In the opposite-direction Marangoni flows with $R_\sigma = 1$, the concentration distributions become chaotic under heat gain. At lower Ma ($Ma = Ma_C = Ma_T$) values, the sampling velocity irregularly fluctuates around zero under strong heat gain, while at higher Ma values, the flow loses its stability as transiting from a periodic mode to a chaotic one. Additionally, at lower Ma values under strong heat gain, the four vortices forming along the free surface are almost of equal size, as the consequence of the induced temperature distribution in the vertical direction.

- In the transition mode maps, two sorts of oscillatory rotating modes are observed in the same-direction Marangoni flows under either heat loss or heat gain, while two kinds of stabilizing effects are predicted under heat loss in the opposite-direction Marangoni flows.

This chapter concentrates on the radiation effects of heat loss and heat gain on thermal and solutal Marangoni convection in a floating half-zone. Transition mode behaves quite different in the same/opposite-direction flow. Different oscillatory rotating modes and

stabilizing effects are discovered due to radiation effects. However, it needs more investigating for its complex formation mechanisms.

6.4 Future perspectives

The work presented in this thesis has shown the characteristics of thermal and solutal Marangoni convection in: (1) a full floating zone, (2) a lower-half floating zone, and (3) a floating half zone with radiation effects. However, there still needs further investigation for flow mechanism and application of flow control.

- As discussed in **Chapter V**, we find two sorts of oscillatory rotating modes in the same-direction Marangoni flow under either heat loss and heat gain and two kinds of stabilizing effects under heat loss in the opposite-direction Marangoni flow. The formation or transition mechanisms are necessary to consider because they behave quite differently.

- Both the numerical results in a full or half floating zone present unsteady flow pattern either in an oscillatory rotating mode or a chaotic mode in some cases, which may adversely affect the uniformity of growing crystal. Therefore, it is hoped that the unsteady flow pattern can be controlled or suppressed by exerting external conditions, such as rotations of top/bottom plane.

References

[1] M. E. Levinshtein, S. L. Rumyantsev, and M. S. Shur, *Properties of Advanced Semiconductor Materials: GaN, AIN, InN, BN, SiC, SiGe* (John Wiley & Sons, 2001).

[2] J. D. Cressler, *Silicon Heterostructure Handbook: Materials, Fabrication, Devices, Circuits and Applications of SiGe and Si Strained-Layer Epitaxy* (CRC press, 2018).

[3] T. Duffar, *Crystal growth processes based on capillarity: Czochralski, floating zone, shaping and crucible techniques* (John Wiley & Sons, 2010).

[4] S. Watauchi, I. Tanaka, K. Hayashi, M. Hirano, and H. Hosono, "Crystal growth of $Ca_{12}Al_{14}O_{33}$ by the floating zone method," *J. Cryst. Growth* **237**, 801–805 (2002).

[5] N. Usami, M. Kitamura, K. Obara, Y. Nose, T. Shishido, and K. Nakajima, "Floating zone growth of Si-rich SiGe bulk crystal using pre-synthesized SiGe feed rod with uniform composition," *J. Cryst. Growth* **284**, 57–64 (2005).

[6] M. Akasaka, T. Iida, T. Nemoto, J. Soga, J. Sato, K. Makino, M. Fukano, and Y. Takanashi, "Non-wetting crystal growth of Mg_2Si by vertical Bridgman method and thermoelectric characteristics," *J. Cryst. Growth* **304**, 196–201 (2007).

[7] K. Hoshikawa, E. Ohba, T. Kobayashi, J. Yanagisawa, C. Miyagawa, and Y. Nakamura, "Growth of β-Ga_2O_3 single crystals using vertical Bridgman method in ambient air," *J. Cryst. Growth* **447**, 36–41 (2016).

[8] T. Nishinaga, *Handbook of crystal growth: fundamentals* (Elsevier, 2014).

[9] Z. Zheng, T. Seto, S. Kim, M. Kano, T. Fujiwara, M. Mizuta, and S. Hasebe, "A first-principle model of 300 mm Czochralski single-crystal Si production process for predicting crystal radius and crystal growth rate," *J. Cryst. Growth* **492**, 105–113 (2018).

[10] M. Miyao and T. Sadoh, "Novel growth techniques of group-IV based semiconductors on insulator for next-generation electronics," *Jpn. J. Appl. Phys.* **56**, 05DA06 (2017).

[11] J. S. Langer, "Instabilities and pattern formation in crystal growth," *Rev. Mod. Phys.* **52**, (1980).

[12] S. Kakac, W. Aung, and R. Viskanta, "Natural convection: fundamentals and applications," *Washington* (1985).

[13] C. J. Chang and R. A. Brown, "Radial segregation induced by natural convection and melt/solid interface shape in vertical bridgman growth," *J. Cryst. Growth* **63**, 343–364 (1983).

[14] X. Zhou and H. Huang, "Numerical simulation of Cz crystal growth in rotating magnetic field with crystal and crucible rotations," *J. Cryst. Growth* **340**, 166–170 (2012).

[15] L. Yao, Z. Zeng, X. Li, J. Chen, Y. Zhang, H. Mizuseki, and Y. Kawazoe, "Effects of rotating magnetic fields on thermocapillary flow in a floating half-zone," *J. Cryst. Growth* **316**, 177–184 (2011).

[16] T. J. Jaber, M. Z. Saghir, and A. Viviani, "Three-dimensional modelling of GeSi growth in presence of axial and rotating magnetic fields." *Eur. J. Mech.-B/Fluids* **28**, 214–223 (2009).

[17] A. Hirata, M. Sakurai, and N. Ohishi, "Effect of gravity on Marangoni convection in a liquid bridge," *J. Jpn. Soc. Microgravity Appl.* **14**, 130–136 (1997).

[18] O. A. Bég, K. Venkatadri, V. R. Prasad, T. Beg, A. Kadir, and H. J. Leonard, "Numerical simulation of hydromagnetic Marangoni convection flow in a Darcian porous semiconductor melt enclosure with buoyancy and heat generation effects," *Mater. Sci. Eng. B* **261**, 114722 (2020).

[19] R. Krechetnikov, "Thermodynamics of chemical Marangoni-driven engines," *Soft Matter* **13**, 4931–4950 (2017).

[20] K. Nishino, "KIBO Japanese Experiment Module", *Japan Aerospace Exploration Agency* (2007).

[21] A. Cröll, W. Müller-Sebert, and R. Nitsche, "The critical Marangoni number for the onset of time-dependent convection in silicon," *Mater. Res. Bull.* **24**, 995–1004 (1989).

[22] R. Rupp, G. Müller, and G. Neumann, "Three-dimensional time dependent modelling of the Marangoni convection in zone melting configurations for GaAs," *J. Cryst. Growth* **97**, 34–41 (1989).

[23] D. Schwabe and A. Scharmann, "Some evidence for the existence and magnitude of a critical Marangoni number for the onset of oscillatory flow in crystal growth melts," *J. Cryst. Growth* **46**, 125–131 (1979).

[24] C. H. Chun and W. Wuest, "Experiments on the transition from the steady to the oscillatory Marangoni-convection of a floating zone under reduced gravity effect," *Acta Astronautica* **6**, 1073–1082 (1979).

[25] N. Imaishi, "Fundamental of the Marangoni convection," *Int. J. Microgravity Sci.* **31**, S5 (2014).

[26] T. Yano and K. Nishino, "Flow visualization of axisymmetric steady Marangoni convection in high-Prandtl-number liquid bridges in microgravity," *Int. J. Microgravity Sci. Appl.* **36**, 360202 (2019).

[27] S. Yasuhiro, T. Sato, and N. Imaishi, "Three dimensional oscillatory Marangoni flow in a half zone of $Pr = 1.02$ fluid," *Microgravity Sci. Technol.* **10**, 144–153 (1998).

[28] C. Le, L. Liu, and Z. Li, "Oscillatory thermocapillary convection in deformed half zone liquid bridges of low Prandtl number fluids," *Int. Commun. Heat Mass Transfer* **127**, 105499 (2021).

[29] D. M. Christopher and B. Wang, "Prandtl number effects for Marangoni convection over a flat surface," *Int. J. Therm. Sci.* **40**, 564–570 (2001).

[30] K. Arafune, M. Sugiura, and A. Hirata, "Investigation of thermal Marangoni convection in low- and high-Prandtl-number fluids," *J. Chem. Eng. Japan* **32**, 104–109 (1999).

[31] J. Wollweber, D. Schulz, and W. Schröder, "Extremely reduced dislocation density in $Si_x Ge_{1-x}$ single crystals grown by the float zone technique," *J. Cryst. Growth* **158**, 166–168 (1996).

[32] H. J. Scheel, "Theoretical and technological solutions of the striation problem," *J. Cryst. Growth* **287**, 214–223 (2006).

[33] Y. Arai, K. Kinoshita, T. Tsukada, M. Kubo, K. Abe, S. Sumioka, S. Baba, and Y. Inatomi, "Study of SiGe crystal growth interface processed in microgravity," *Cryst. Growth Des.* **18**, 3697–3703 (2018).

[34] T. Tsukada, "The role of Marangoni convection in crystal growth," *Handbook of Crystal Growth* (Elsevier) 871–907 (2015).

[35] T. Campbell, M. Schweizer, P. Dold, A. Cröll, and K. Benz, "Float zone growth and characterization of $Ge_{1-x}Si_x$ ($x \leq 10$ at %) single crystals," *J. Cryst. Growth* **226**, 231–239 (2001).

[36] K. Motegi, M. Kudo, and I. Ueno, "Linear stability of buoyant thermocapillary convection for a high-Prandtl number fluid in a laterally heated liquid bridge," *Phys. Fluids* **29**, 044106 (2017).

[37] H. Kawamura, K. Nishino, S. Matsumoto, and I. Ueno, "Report on microgravity experiments of Marangoni convection aboard international space station," *J. Heat Transfer* **134**, 031005 (2012).

[38] J. Ezquerro, P. S. Sanchez, A. Bello, J. Rodriguez, V. Lapuerta, and A. Laveron-Simavilla, "Experimental evidence of thermocapillarity in phase change materials in microgravity: Measuring the effect of Marangoni convection in solid/liquid phase transitions," *Int. Commun. Heat Mass Transfer* **113**, 104529 (2020).

[39] T. Duffar, M. Serrano, L. Lerin, and J. Santaller, "Marangoni convective effect during crystal growth in space," *Cryst. Res. Technol.* **34**, 457–465 (1999).

[40] T. Yano, K. Nishino, H. Kawamura, I. Ueno, S. Matsumoto, M. Ohnishi, and M. Sakurai, "Space experiment on the instability of Marangoni convection in large liquid bridge-MEIS-4: effect of Prandtl number," *J. Phys. Conf. Ser.* **327**, 012029 (2011).

[41] Q. Kang, D. Wu, L. Duan, J. He, L. Hu, L. Duan, and W. Hu, "Surface configurations and wave patterns of thermocapillary convection onboard the SJ10 satellite," *Phys. Fluids* **31**, 044105 (2019).

[42] T. Yano, K. Nishino, H. Kawamura, I. Ueno, S. Matsumoto, M. Ohnishi, and M. Sakurai, "3-D PTV measurement of Marangoni convection in liquid bridge in space experiment," *Exp. Fluids* **53**, 9–20 (2012).

[43] T. Munakata, S. Someya, and I. Tanasawa, "Suppression of Marangoni convection in the FZ melt by high-frequency magnetic field," *J. Cryst. Growth* **235**, 167–172 (2002).

[44] B. Fischer, J. Friedrich, H. Weimann, and G. Müller, "The use of time-dependent magnetic fields for control of convective flows in melt growth configurations," *J. Cryst. Growth* **198**, 170–175 (1999).

[45] J. Zueco and O. A. Bég, "Network numerical simulation of hydromagnetic Marangoni mixed convection boundary layers," *Chem. Eng. Commun.* **198**, 552–571 (2010).

[46] D. Montgomery, "Hartmann, Lundquist, and Reynolds: the role of dimensionless numbers in nonlinear magnetofluid behavior," *Plasma Phys. Control. Fusion* **35**, B105 (1993).

[47] J. Mackolil and B. Mahanthesh, "Inclined magnetic field and nanoparticle aggregation effects on thermal Marangoni convection in nanoliquid: A sensitivity analysis," *Chinese J. Phys.* **69**, 24–37 (2021).

[48] Q. M. Al-Mdallal, N. Indumathi, B. Ganga, and A. A. Hakeem, "Marangoni radiative effects of hybrid-nanofluids flow past a permeable surface with inclined magnetic field," *Case Stud. Therm. Eng.* **17**, 100571 (2020).

[49] C. Wu, D. Ruan, Y. Li, and R. Liao, "Flow pattern transition driven by the combined Marangoni effect and rotation of crucible and crystal in a Czochralski configuration," *Int. J. Therm. Sci.* **86**, 394–407 (2014).

[50] M. Lappa, "Control of convection patterning and intensity in shallow cavities by harmonic vibrations," *Microgravity Sci. Technol.* **28**, 29–39 (2016).

[51] M. Kawaji, R. Liang, M. Nasr-Esfahany, S. Simic-Stefani, and S. Yoda, "The effect of small vibrations on Marangoni convection and the free surface of a liquid bridge," *Acta Astronautica* **58**, 622–632 (2006).

[52] O. A. Noghabi, M. M'Hamdi, and M. Jomâa, "Effect of crystal and crucible rotations on the interface shape of Czochralski grown silicon single crystals," *J. Cryst. Growth* **318**, 173–177 (2011).

[53] T. Lyubimova and R. Skuridin, "Control of thermo- and solutocapillary flows in FZ crystal growth by high-frequency vibrations," *J. Appl. Mech. Tech. Phys.* **58**, 1159–1170 (2017).

[54] Y. Takagi, Y. Okano, H. Minakuchi, and S. Dost, "Combined effect of crucible rotation and magnetic field on hydrothermal wave," *J. Cryst. Growth* **385**, 72–76 (2014).

[55] Y. Takehara, A. Sekimoto, Y. Okano, T. Ujihara, and S. Dost, "Bayesian optimization for a high- and uniform-crystal growth rate in the top-seeded solution growth process of silicon carbide under applied magnetic field and seed rotation," *J. Cryst. Growth* **532**, 125437 (2020).

[56] M. Tsai and S. Kou, "Marangoni convection in weld pools with a free surface," *Int. J. Num. Methods Fluids* **9**, 1503–1516 (1989).

[57] S. Shklyaev, M. Khenner, and A. Alabuzhev, "Oscillatory and monotonic modes of long-wave Marangoni convection in a thin film," *Phys. Rev. E* **82**, 025302 (2010).

[58] Y. Li, Z. Chen, and J. Zhan, "Double-diffusive Marangoni convection in a rectangular cavity: transition to chaos," *Int. J. Heat Mass Transfer* **53**, 5223–5231 (2010).

[59] H. Liu, Z. Zeng, L. Yin, Z. Qiu, and L. Qiao, "Influence of aspect ratio on the onset of thermocapillary flow instability in annular pool heated from inner wall," *Int. J. Heat Mass Transfer* **129**, 746–752 (2019).

[60] H. Aminfar, M. Mohammadpourfard, and F. Mohseni, "Numerical investigation of thermocapillary and buoyancy driven convection of nanofluids in a floating zone," *Int. J. Mech. Sci.* **65**, 147–156 (2012).

[61] L. Yao, Z. Zeng, Y. Zhang, Z. Qiu, H. Mei, L. Zhang, and Y. Zhang, "Influence of rotating magnetic field strength on three-dimensional thermocapillary flow in a floating half-zone model," *Heat Mass Transfer* **48**, 2103–2111 (2012).

[62] A. Sabanskis, K. Surovovs, and J. Virbulis, "3D modeling of doping from the atmosphere in floating zone silicon crystal growth," *J. Cryst. Growth* **457**, 65–71 (2017).

[63] B. Šeta, D. Dubert, J. Massons, J. Gavalda, M. M. Bou-Ali, and X. Ruiz, "Effect of Marangoni induced instabilities on a melting bridge under microgravity conditions," *Int. J. Heat Mass Transfer* **179**, 121665 (2021).

[64] N. Imaishi, S. Yasuhiro, Y. Akiyama, and S. Yoda, "Numerical simulation of oscillatory Marangoni flow in half-zone liquid bridge of low Prandtl number fluid," *J. Cryst. Growth* **230**, 164–171 (2001).

[65] K. Li, N. Imaishi, C. Jing, and S. Yoda, "Proper orthogonal decomposition of oscillatory Marangoni flow in half-zone liquid bridges of low-*Pr* fluids," *J. Cryst. Growth* **307**, 155–170 (2007).

[66] K. Li, B. Xun, N. Imaishi, S. Yoda, and W. Hu, "Thermocapillary flows in liquid bridges of molten tin with small aspect ratios," *Int. J. Heat Fluid Flow* **29**, 1190–1196 (2008).

[67] M. Lappa, *Thermal Convection: Patterns, Evolution and Stability* (John Wiley & Sons, 2009).

[68] M. Lappa, *Fluids, materials and microgravity: numerical techniques and insights into physics* (Elsevier, 2004).

[69] R. L. A. Mendis, A. Sekimoto, Y. Okano, H. Minakuchi, and S. Dost, "The relative contribution of solutal Marangoni convection to thermal Marangoni flow instabilities in a liquid bridge of smaller aspect ratios under zero gravity," *Crystals* **11**, 116 (2021).

[70] J. Zhang, A. Sekimoto, Y. Okano, and S. Dost, "Numerical simulation of thermal-solutal Marangoni convection in a shallow rectangular cavity with mutually perpendicular temperature and concentration gradients," *Phys. Fluids* **32**, 102108 (2020).

[71] R. L. A. Mendis, A. Sekimoto, Y. Okano, H. Minakuchi, and S. Dost, "Global linear stability analysis of thermo-solutal Marangoni convection in a liquid bridge under zero gravity," *Microgravity Sci. Technol.* **32**, 729–735 (2020).

[72] R. L. A. Mendis, A. Sekimoto, Y. Okano, H. Minakuchi, and S. Dost, "A numerical study on the exact onset of flow instabilities in thermo-solutal Marangoni convection driven by opposing forces in a half-zone liquid bridge under zero gravity," *J. Chem. Eng. Japan* **54**, 424–430 (2021).

[73] H. Minakuchi, Y. Takagi, Y. Okano, S. Gima, and S. Dost, "The relative contributions of thermo-solutal Marangoni convections on flow patterns in a liquid bridge," *J. Cryst. Growth* **385**, 61–65 (2014).

[74] H. Minakuchi, Y. Okano, and S. Dost, "Effect of thermo-solutal Marangoni convection on the azimuthal wave number in a liquid bridge," *J. Cryst. Growth* **468**, 502–505 (2017).

[75] H. Minakuchi, Y. Okano, and S. Dost, "The hysteresis phenomena of flow patterns due to thermal and solutal Marangoni convections in a liquid bridge under zero gravity," *Fluid Mech. Res. Int.* **2**, 00018 (2018).

[76] C. Jin, Y. Okano, H. Minakuchi, and S. Dost, "Numerical simulation of thermo-solutal Marangoni convection in a full floating zone with radiative heat transfer under zero gravity", *J. Cryst. Growth* **570**, (2021) 126204.

[77] C. Jin, A. Sekimoto, Y. Okano, H. Minakuchi, and S. Dost, "Characterization of the thermal and solutal Marangoni flows of opposite directions developing in a cylindrical liquid bridge under zero gravity", *Phys. Fluids* **32**, (2020) 034104.

[78] C. Jin, Y. Okano, H. Minakuchi, and S. Dost, "Numerical simulation of thermo-solutal Marangoni convection in a floating half-zone with radiation effects under zero gravity", *Int. J. Heat Mass Transfer* **194**, (2022) 123010.

[79] A. Mühlbauer, A. Muiznieks, J. Virbulis, A. Lüdge, and H. Riemann, "Interface shape, heat transfer and fluid flow in the floating zone growth of large silicon crystals with the needle-eye technique," *J. Cryst. Growth* **151**, 66–79 (1995).

[80] F. Romanò, H. C. Kuhlmann, M. Ishimura, and I. Ueno, "Limit cycles for the motion of finite-size particles in axisymmetric thermocapillary flows in liquid bridges," *Phys. Fluids* **29**, 093303 (2017).

[81] T. Yano, K. Nishino, I. Ueno, S. Matsumoto, and Y. Kamotani, "Sensitivity of hydrothermal wave instability of Marangoni convection to the interfacial heat transfer in long liquid bridges of high Prandtl number fluids," *Phys. Fluids* **29**, 044105 (2017).

[82] S. Abbasoglu and I. Sezai, "Three-dimensional modelling of melt flow and segregation during Czochralski growth of Ge$_x$Si$_{1-x}$ single crystals," *Int. J. Therm. Sci.* **46**, 561–572 (2007).

[83] Z. Chen, Y. Li, and J. Zhan, "Double-diffusive Marangoni convection in a rectangular cavity: Onset of convection," *Phys. Fluids* **22**, 034106 (2010).

[84] F. Doumenc, E. Chénier, B. Trouette, T. Boeck, C. Delcarte, B. Guerrier, and M. Rossi, "Free convection in drying binary mixtures: solutal versus thermal instabilities," *Int. J. Heat Mass Transfer* **63**, 336–350 (2013).

[85] H. Minakuchi, Y. Takagi, Y. Okano, K. Mizoguchi, S. Gima, and S. Dost, "A grid refinement study of half-zone configuration of the Floating Zone growth system," *J. Advanced Res. Phys.* **3**, 011201 (2012).

[86] H. Minakuchi, Y. Takagi, Y. Okano, T. Nosoko, S. Gima, and S. Dost, "Three-dimensional numerical simulation of thermal and solutal Marangoni convection in a liquid bridge under zero-gravity field," *Trans. JSASS Aerospace Tech. Japan* **10**, 15–20 (2012).

[87] M. Lappa, "Floating zones heated around the equatorial plane: models and simulations," *Microgravity Sci. Technol.* **15**, 36–51 (2004).

[88] C. Le, L. Liu, and Z. Li, "Numerical investigation of the effect of rotation on the oscillatory thermocapillary convection and dopant transport in a silicon liquid bridge," *J. Cryst. Growth* **523**, 125149 (2019).

[89] Y. Zou, H. Huang, G. Zhu, and X. Zhou, "Effect of rotating magnetic field on thermal convection and dopant transport in floating-zone crystal growth," *Microgravity Sci. Technol.* **32**, 349–361 (2020).

[90] T. Lyubimova and R. Scuridyn, "Numerical modelling of three-dimensional thermo- and solutocapillary-induced flows in a floating zone during crystal growth," *Eur. Phys. J. Special Topics* **192**, 41–46 (2011).

[91] C. Wu, J. Chen, B. Yuan, and Y. Li, "Bifurcations and pattern evolutions of thermo-solutocapillary flow in rotating cylinder with a top disk," *Phys. Fluids* **31**, 094103 (2019).

[92] J. Zhang, Y. Okano, and S. Dost, "Effect of radiative heat transfer on thermal-solutal Marangoni convection in a shallow rectangular cavity with mutually perpendicular temperature and concentration gradients," *Int. J. Heat Mass Transfer* **183**, 122104 (2022).

[93] N. Shitomi, T. Yano, and K. Nishino, "Effect of radiative heat transfer on thermocapillary convection in long liquid bridges of high-Prandtl-number fluids in microgravity," *Int. J. Heat Mass Transfer* **133**, 405–415 (2019).

Acknowledgements

First and foremost, I would like to express my sincere gratitude to my supervisor, Professor Yasunori Okano, who gave me the opportunity to study in Osaka University from a master student, and now a doctoral student and conduct my research. It is my great honor to study here and obtain expert guidance, constructive advice, and meticulous support in the research work by Prof. Okano. I would like to say "Thanks" to the Graduate School of Engineering Science and Osaka University, providing me the valuable opportunity to study here and enjoy the unforgettable campus life.

Secondly, I would like to convey my gratitude to Dr. Hisashi Minakuchi, for his valuable comments and advice in my research of "Marangoni convection in a floating zone". I would like to be thankful to Dr. Sadik Dost, for his careful and detailed revisions of manuscripts in the paper submissions, which helps me improve the grammatical and linguistic skills. I would appreciate Prof. Norikazu Nishiyama, Shinji Sakai, and Hisashi Minakuchi for their meaningful comments in my doctor's defense, as well as Prof. Changyi Kong from Shizuoka University.

Thirdly, I would appreciate every member in Okano Laboratory, as well as Atsushi Sekimoto, for collaborated research discussions in the seminar and presentation rehearsal before conferences. These are the enjoyable and unforgettable moments for self-improvement in research field, especially attending domestic and international conferences.

Finally, I would like to express my appreciation to my family for their endless love, support, and encouragement throughout these five years' study and life. Especially, during the epidemic of COVID-19, even in some difficult moments, they care about me all the time. Additionally, I would like to appreciate Ichikawa International Scholarship Foundation for their financial support and warm encouragement during my last one year and a half, reducing my financial burden and having the opportunities to know more excellent friends.

Last of the last, I would like to thank myself for the persistence all the way. All of the experiences in Osaka University are precious life treasure. I will continuing working harder in my future life.

List of Publications

[Published papers]

1. <u>Chihao Jin</u>, Atsushi Sekimoto, Yasunori Okano, Hisashi Minakuchi, and Sadik Dost, "Characterization of the thermal and solutal Marangoni flows of opposite directions developing in a cylindrical liquid bridge under zero gravity", *Phys. Fluids* **32**, (2020) 034104. **[Editor's Pick, Highlighted by Scilight]**

2. <u>Chihao Jin</u>, Yasunori Okano, Hisashi Minakuchi, and Sadik Dost, "Numerical simulation of thermo-solutal Marangoni convection in a full floating zone with radiative heat transfer under zero gravity", *J. Cryst. Growth* **570**, (2021) 126204.

3. <u>Chihao Jin</u>, Yasunori Okano, Hisashi Minakuchi, and Sadik Dost, "Numerical simulation of thermo-solutal Marangoni convection in a floating half-zone with radiation effects under zero gravity", *Int. J. Heat Mass Transfer* **194**, (2022) 123010.

[International conferences]

1. <u>Chihao Jin</u>, Atsushi Sekimoto, Yasunori Okano, and Hisashi Minakuchi, "The numerical study of co-existence effect of thermal and solutal Marangoni convections in a liquid bridge", *The 17th International Conference on Global Research and Education, Inter-Academia-2018*, Kaunas, Lithuania, Sep. 2018. (Oral)

2. <u>Chihao Jin</u>, Yasunori Okano, Hisashi Minakuchi, and Sadik Dost, "Numerical simulation of thermo-solutal Marangoni convection in a full floating zone with radiative heat transfer under zero gravity", *The 8th Asian Conference on Crystal Growth and Crystal Technology (CGCT-8)*, Online, Mar. 2021. (Oral)

[Domestic conferences]

1. <u>Chihao Jin</u>, Atsushi Sekimoto, Yasunori Okano, and Hisashi Minakuchi, "The numerical study of the instability and control of thermo-solutal Marangoni convection", *The 55th Heat Transfer Symposium*, Sapporo, May 2018. (Oral)

2. <u>Chihao Jin</u>, Atsushi Sekimoto, Yasunori Okano, and Hisashi Minakuchi, "The numerical simulation of thermal and solutal Marangoni convections in the opposite direction in a liquid bridge", *The SCEJ 50th Autumn Meeting*, Kagoshima, Sep. 2018. (Oral)

3. <u>Chihao Jin</u>, Atsushi Sekimoto, Yasunori Okano, and Hisashi Minakuchi, "Numerical simulation of the opposite thermal and solutal Marangoni convections in a liquid bridge under zero gravity", *Conference of the Japan Society of Microgravity Application (JASMAC-31)*, Sendai, Oct. 2019. (Poster) **[最優秀賞]**

4. <u>Chihao Jin</u>, Atsushi Sekimoto, Yasunori Okano, and Hisashi Minakuchi, "Numerical simulation of thermal and solutal Marangoni convection in a full floating zone with radiative heat transfer under zero gravity", *Conference of the Japan Society of Microgravity Application (JASMAC-32)*, Online, Oct. 2020. (Oral)

5. <u>Chihao Jin</u>, Yasunori Okano, and Hisashi Minakuchi, "Numerical simulation of thermal and solutal Marangoni convection in a half floating zone with radiation effects under zero gravity", *Conference of the Japan Society of Microgravity Application (JASMAC-33)*, Online, Oct. 2021. (Oral)